Upper Tropospheric Ozone Enhancement during the North American Monsoon evaluated using the Weather Research and Forecasting Model with Chemistry (WRF-Chem)

by

J. Wong

M.S., University of Colorado, 2010

M.A., University of Arkansas, 2007

B.S., University of Arkansas, 2006

A thesis submitted to the

Faculty of the Graduate School of the

University of Colorado in partial fulfillment

of the requirements for the degree of

Doctor of Philosophy

Department of Atmospheric and Oceanic Sciences

2013

This thesis entitled:
Upper Tropospheric Ozone Enhancement during the North American Monsoon evaluated using the Weather Research and Forecasting Model with Chemistry (WRF-Chem)
written by J. Wong
has been approved for the Department of Atmospheric and Oceanic Sciences

_____

Dr. David Noone

_____

Dr. Mary Barth

_____

Dr. Darin Toohey

Date _____

The final copy of this thesis has been examined by the signatories, and we find that both the content and the form meet acceptable presentation standards of scholarly work in the above mentioned discipline.

Wong, J. (Ph.D., Atmospheric and Oceanic Sciences)

Upper Tropospheric Ozone Enhancement during the North American Monsoon evaluated using the Weather Research and Forecasting Model with Chemistry (WRF-Chem)

Thesis directed by Dr. David Noone

Upper tropospheric ozone has significant impacts on the total atmospheric chemistry and radiative budget. Previous studies noted an upper tropospheric ozone enhancement above southern United States during the North Ameican Monsoon (NAM). This recurring phenomenon has been observed by the satellite-borne Tropospheric Emission Spectrometer (TES) and IONS-06 ozonesondes. Using the Weather Research and Forecasting model with Chemistry (WRF-Chem), we attempt to simulate the ozone enhancement and understand the underlying structure, chemical pathways, and sensitivity to emissions.

Using a modified lightning parameterization based on the Price and Rind scheme, a July-August simulation is performed using WRF-Chem. Validation shows that flash rate is overpredicted by a factor of 10, which subsequently causes an overestimation of O_3. Despite the amplified ozone enhancement, boundary layer and stratospheric tracers do not show substantial differences within and outside the anticyclone, contrary to what has been predicted in other studies. On the other hand, lightning tracers, lateral boundary tracers, tracer-tracer correlations, and chemistry pathways can be used to distinguish between the anticyclone and the surrounding area.

Sensitivity and control simulations are also performed to investigate how different emission sources contribute to the ozone enhancement. It is shown that lightning emission enhances NO_x superlinearly, which leads to NO_x-titration in the upper troposphere. On the other hand, anthropogenic emission is shown to modify the ozone concentration and chemistry profiles via sensitivity to VOC, and biogenic emission affects ozone via sensitivity to NO_x. As a result of the changes in ozone mixing ratio profile, convective tendency is also affected, which forms a nonlinear feedback between chemistry and convection in response to perturbation in emissions.

Acknowledgements

First and foremost, I would like to thank Dr. Mary Barth (NCAR/ACD) and Dr. David Noone (CIRES/ATOC) for providing the opportunities and exceptional guidance throughout my graduate study at University of Colorado at Boulder. This work was supported by the NASA Atmospheric Composition program (grant number NNH07AM47G) and appointment via the NRCM project (NSF-EaSM grant AGS-1048829; "Developing a Next-Generation Approach to Regional Climate Prediction at High Resolution"). The NLDN dataset is provided by Vaisala and made available via Dr. James Crawford of NASA Langley Research Center and Dr. Owen Cooper at NOAA/ESRL. The ENTLN dataset is prepared and provided by Steve Prinzivall at Earth Networks. We would like to ackowledge high-performance computing support provided by NCAR's Computational and Information Systems Laboratory, sponsored by the National Science Foundation (project code P35071370). We also thank the following individuals who have provided valuable advices and insights in relation to this study and assistance in developing the diagnostics and lightning parameterization modules for WRF-Chem: Dr. Linnea Avallone (LASP/ATOC), Dr. Georg Grell (NOAA/ESRL/GSD), Dr. Sasha Madronich (NCAR/ACD), Dr. David Noone (CIRES/ATOC), Dr. Steven Peckham (NOAA/ESRL/GSD), Dr. Gabriele Pfister (NCAR/ACD), Dr. Bill Skamarock (NCAR/MMM), Dr. John Worden (NASA/JPL). Finally, I would like to acknowledge and thank Dr. Tom Warner (NCAR/RAL, CU-Boulder/ATOC) for his support before he passed away on May 30, 2011.

Contents

Chapter

Tables

Table

Figures

Figure

Chapter 1

Introduction

Upper tropospheric ozone has significant impacts on the radiative and chemical budgets of the atmosphere (*Kiehl et al.*, 1999). The global tropospheric ozone burden has seen an increase of 71–130 Tg since the preindustrial period, with much of the uncertainties coming from the estimation of preindustrial emission scenarios for anthropogenic, biomass burning, and lightning sources (*Lamarque et al.*, 2005, and references therein). The radiative forcing resulting from this increase depends strongly on the vertical distribution and is the most sensitive near the tropopause (*Lacis et al.*, 1990). *Gauss et al.* (2006) calculated that the global net radiative forcing resulting from a 7.9–13.8 Dobson units increase in tropospheric ozone (ignoring stratospheric changes) varies between 0.25 and 0.45 $\mathrm{W\,m^{-2}}$. In particular, several models cited by *Gauss et al.* (2006) as well as *Stevenson et al.* (1998) estimated up to 0.5–1.1 $\mathrm{W\,m^{-2}}$ increase over parts of northern mid-latitude regions such as the United States and the Mediterranean region. The ozone increases over these areas are

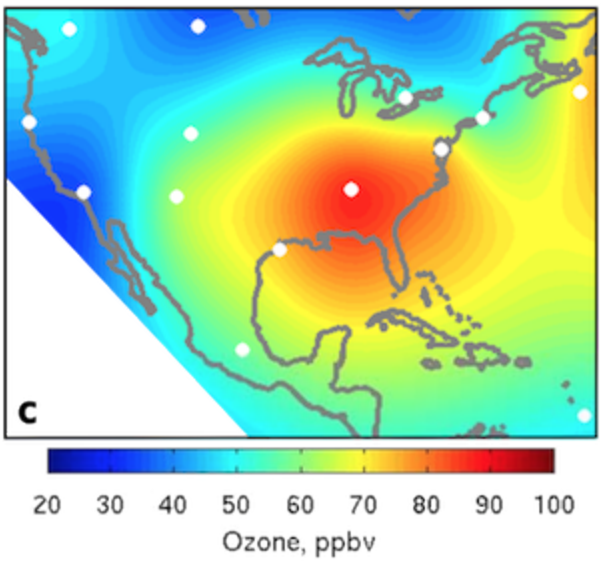

Figure 1.1: **Filtered upper tropospheric ozone from *Cooper et al.* (2007)** — Interpolated ozonesonde measurements between 10 and 11 km less stratospheric influence estimated using back trajectory (after *Cooper et al.*, 2007, Figure 2c).

also observed by ozonesonde records spanning periods between 1970's and 2004 (*Oltmans et al.*, 2006).

Recent studies have identified monsoonal accumulations of ozone precursors above North America (*Li et al.*, 2005; *Cooper et al.*, 2009, and references therein), Asia (*Park et al.*, 2007; *Worden et al.*, 2009), and equatorial Africa (*Bouarar et al.*, 2011) during summers in the upper troposphere. *Cooper et al.* (2007) calculated a median tropospheric ozone mixing ratio of 87 ppbv (after removing stratospheric intrusion) above Huntsville, AL in August 2006 (Figure 1.1). This is about twice the value measured along the United States west coast during the same period. The observed upper tropospheric ozone enhancement is linked to the North American Monsoon anticyclonic circulation, which traps ozone precursors that subsequently enhance ozone production (*Li et al.*, 2005). *Cooper et al.* (2006) estimated that up to 84% of the enhancement observed above the southern United States can be attributed to *in situ* ozone production from lightning-produced NO_x (LNO_x). The local radiative forcing of this enhancement is $+0.50\,W\,m^{-2}$, 70% of which is attributable to enhancement through LNO_x.

By leveraging improved lightning parameterization, online budgeting diagnostics, and passive tracers, this thesis intends to extend the results from previous studies and understand various contributing factors that led to the observed ozone distribution. To understand the processes involved in the NAM upper tropospheric ozone enhancement, the central topic of this thesis, the primary goals of this study are defined as follow:

(1) Simulate the observed ozone distribution using a regional chemistry transport model and evaluate the outputs against independent observations;

(2) Utilize online budgeting diagnostics and passive tracers to understand the evolution of the simulated ozone distribution;

(3) Conduct sensitivity simulations to evaluate how the ozone enhancement would react to different scenarios of anthropogenic, biogenic, and lightning emissions.

1.1 Tropospheric ozone chemistry

Since the primary goals of this study involve diagnosing the simulated ozone values, it is crucial to understand the basis and complexity of tropospheric ozone chemistry. Through its production-destruction cycle, ozone interacts with dozens of chemical species in the troposphere. In the presence of water and shortwave radiation, photodissociation of ozone is also a major precursor for hydroxl (OH) radicals through the following reactions:

$$\mathsf{O_3} + h\nu(\lambda < 330\,\mathsf{nm}) \rightarrow \mathsf{O}(^1\mathsf{D}) + \mathsf{O_2} \tag{1.1}$$

$$\mathsf{O}(^1\mathsf{D}) + \mathsf{H_2O} \rightarrow 2\mathsf{OH} \tag{1.2}$$

Since OH is the primary oxidizing agent for many volatile organic compounds (VOCs) in the atmosphere, by extension, ozone governs the oxidation capacity of the atmosphere and the lifetime of many trace gases, many of which exclusively originate from anthropogenic and biogenic emissions.

In a dry low-hydrocarbon atmosphere such as the stratosphere, the following reactions determine the steady-state level of ozone:

$$\mathsf{NO_2} + h\nu \rightarrow \mathsf{NO} + \mathsf{O}(^3\mathsf{P}) \tag{1.3}$$

$$\mathsf{O}(^3\mathsf{P}) + \mathsf{O_2} + \mathsf{M} \rightarrow \mathsf{O_3} + \mathsf{M} \tag{1.4}$$

$$\mathsf{O_3} + \mathsf{NO} \rightarrow \mathsf{NO_2} + \mathsf{O_2} \tag{1.5}$$

Reaction 1.4 is a termolecular reaction consuming a ground-state oxygen atom produced primarily from photolysis of $\mathsf{NO_2}$ (Reaction 1.3). However, the produced $\mathsf{O_3}$, or any other ozone molecule in the environment, may react with NO to form $\mathsf{NO_2}$ again (Reaction 1.5). This set of reactions does not destroy or produce ozone molecules, thus it implies a steady-state of ozone, which may be characterized by $[\mathsf{O_3}] \approx (J_{1.3}/k_{1.5})([\mathsf{NO_2}]/[\mathsf{NO}])$, where $J_{1.3}$ is the photolysis rate constant for Reaction 1.3 and $k_{1.5}$ is the rate constant for Reaction 1.5.

In the presence of volatile organic compounds (VOCs) and hydroxyl radicals (OH), however, the reaction set becomes much more complicated. VOCs may be oxidized to produce hydroperoxy radicals ($\mathsf{HO_2}$), e.g. from CO and HCHO, or other peroxy radicals with higher carbon numbers

(RO_2), e.g. methyl peroxy radical (CH_3O_2). These products may then compete with Reaction 1.5 to consume the available NO without the cost of an ozone molecule in the process:

$$HO_2 + NO \rightarrow HO + NO_2 \tag{1.6}$$

$$RO_2 + NO \rightarrow RO + NO_2 \tag{1.7}$$

Of course, the produced NO_2 may now proceed to be photolyzed through Reaction 1.3 and perpetuate the ozone cycle. Incidentally, an excess presence of HO_x from the oxidation of VOCs is capable of reducing ozone level through two reactions:

$$O_3 + HO \rightarrow HO_2 + O_2 \tag{1.8}$$

$$O_3 + HO_2 \rightarrow HO + 2O_2 \tag{1.9}$$

Thus excessive presence of hydrocarbons without sufficient NO to carry out Reactions 1.6 and 1.7 also has the potential of destroying ozone by shortcutting the ozone recycling reaction chain.

All the reactions between O_3, NO_x, HO_x and VOCs result in an ozone level determined by the balance between NO_x and VOCs concentrations as well as photolysis rates. Too much NO_x without sufficient VOCs may cause "NO_x-titration," a process which reduces ozone concentration through Reaction 1.5. On the other hand, in an environment with sufficient VOCs but NO_x is scarce, ozone is also destroyed. Thus, for high ozone level to occur (such as in photochemical smogs), compatible levels of both NO_x and VOCs are required. In theory, the variability of ozone concentration in a homogeneously mixed volume may be explained by looking at the ratio between NO_x and VOCs, and identifying the corresponding NO_x-limited and VOC-limited regimes. In practice, transport and mixing complicates such approximation.

1.1.1 Sources for Volatile organic compounds (VOCs)

The definition of volatile organic compounds, or VOCs, varies. For consistency, we use the following definition from the United States Environmental Protection Agency (EPA):

> Volatile organic compounds (VOC) means any compound of carbon, excluding carbon monoxide, carbon dioxide, carbonic acid, metallic carbides or carbonates,

> and ammonium carbonate, which participates in atmospheric photochemical reactions (*EPA*, 2012).

The extended definition also explicitly excludes specific chemicals for "negligible photochemical reactivity," e.g. methane, ethane, CFCs, HCFCs, HFCs. Sources for VOCs can be partitioned largely into anthropogenic and biogenic emissions, with episodic contributions from biomass burning and volcanic eruptions.

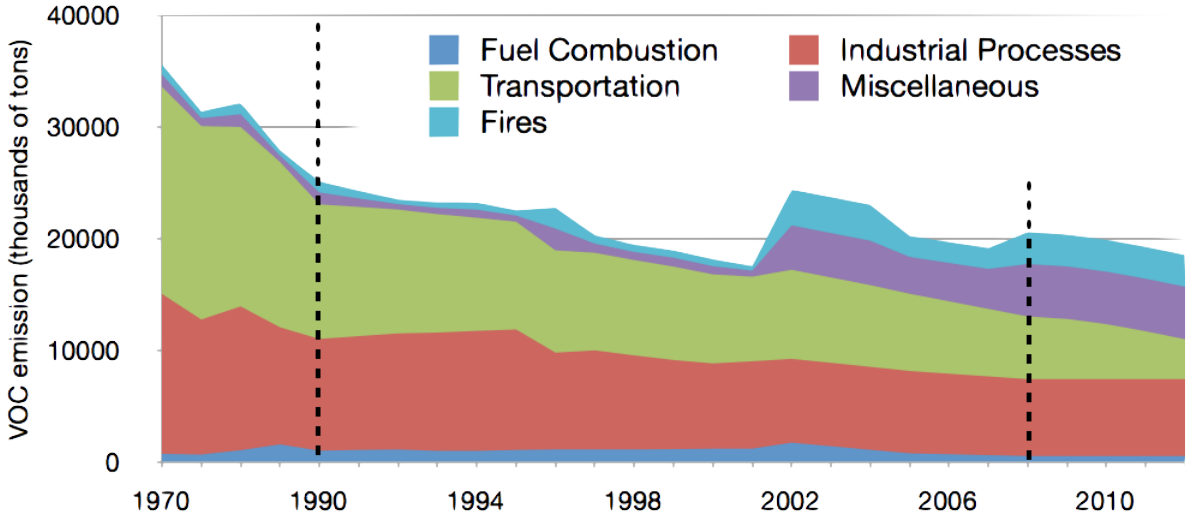

Figure 1.2: **National Emission Inventory (NEI) VOC emission trend** — Trend for total NEI VOC emission for 1970–2012. Data points prior to 1990 were reported every 5 years. 2006 and 2007 are interpolation of 2005 and 2008 data. After 2008, except for transportation, all other emissions were assumed constant. While some changes are real, some are due to changes in inventory methodology.

According to the EPA's 2008 National Emission Inventory (NEI), the leading sources for anthropogenic VOCs in the United States are industrial processes, emitting 6.9×10^6 tons and contributing to a third of the national anthropogenic VOC budget including wild fires (Fig. 1.2). VOC emission from transportation was 5.6×10^6 tons (27% of total). These numbers are to be compared to 2005 figures of 7.4×10^6 tons (36% of total) for industrial processes and 6.9×10^6 tons (34%) for transportation. Further reduction in emission from transportation is seen in 2011, down to 4.3×10^6 tons. However, emission from wild fires have drastically increased to 2.8×10^6 tons

(4%) in 2008 from 1.9×10^6 tons (3%) in 2005[1] . Also, emission from the "miscellaneous" category, which includes sources such as prescribed fire and gas stations, also increased from 3.3×10^6 tons (9%) in 2005 to 4.7×10^6 tons (14%) in 2008. Totals excluding wild fire were 18.3×10^5 tons for 2005 and 17.7×10^6 tons for 2008.

NEI2008 also estimated $31.7 \times 10^6\,\mathsf{tons}$ of biogenic VOCs (BVOCs) in the contiguous United States (CONUS). In rural areas, BVOCs naturally dominates. On the synoptic scale, as anthropogenic VOC emission is being reduced through regulatory efforts, the impact of BVOCs on tropospheric chemistry is also becoming more important. Of the hundreds of BVOCs identified, the global flux is dominated by isoprene ($\mathsf{C_5H_8}$) (*Guenther et al.*, 2006), which is primarily emitted by terrestrial foliage. Bottom-up global estimates of isoprene emission using the Model for Emissions of Gases and Aerosols from Nature (MEGAN) gives about 600 Tg for 2003 (*Guenther et al.*, 2006), and its regional distribution has been further constrained with satellite observation of formaldehyde (HCHO) column from satellite instruments such as the Global Ozone Monitoring Experiment (GOME) instrument on board of ERS-2 (*Palmer et al.*, 2001, 2003, 2006), the SCIAMACHY instrument on board of the ENVISAT (*Dufour et al.*, 2009; *De Smedt et al.*, 2008, 2010), and the Ozone Monitoring Instrument (OMI) on board of the EOS Aura satellite (*Millet et al.*, 2008; *Marais et al.*, 2012).

Due to ozone's nonlinear sensitivity to changes in VOC, the simulation of ozone depends heavily on the accurate characterization of the emission inventory inputs or parameterization, which is the sole source for many hydrocarbons such as toluene or alkanes of high carbon numbers. Of particular interest to this study is how changes in each of these sources may impact the observed upper tropospheric ozone level and ultimately the chemistry budget.

[1] This increase is partially due to re-classification of "open burning" emissions into two separate categories of wildfires and prescribed burning in 2008.

1.1.2 Anthropogenic sources for Nitrogen oxides (ANO_x)

Due to the large contribution from BVOCs, the ambient ozone level is controlled by the oxides of nitrogen ($NO_x \equiv NO + NO_2$), which is dominated by anthropogenic NO_x (ANO_x). The straightforward conjecture is that the more NO_x is available, the higher the ozone concentration. However, this is not the case in either "clean" air, wherein VOC level is low, or in the presence of excessive NO_x. Either case can induce NO_x-titration, which is discussed briefly in Section 1.1. In addition, lightning-generated NO_x, or LNO_x, and soil[2] NO_x are also identified as an important natural source for atmospheric NO_x. Introduction to LNO_x is provided in the next section (Section 1.2).

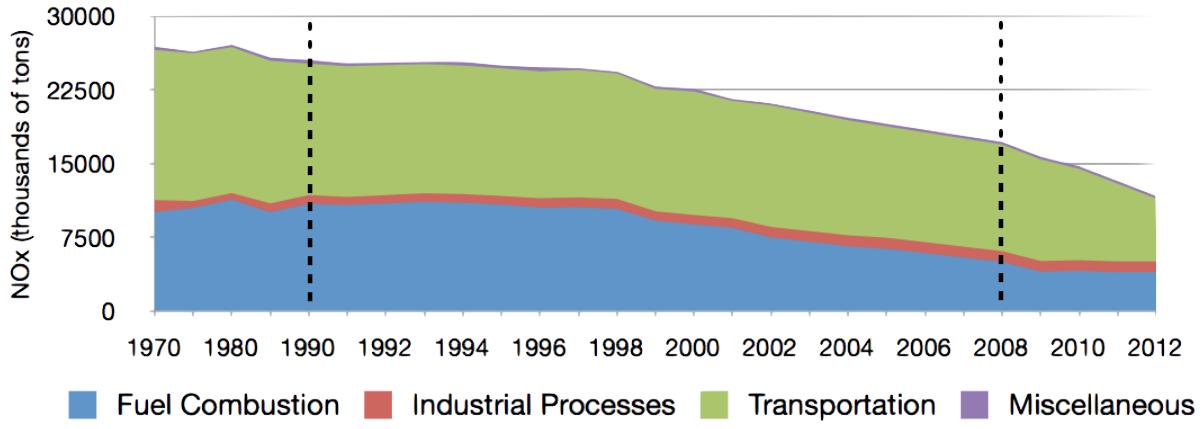

Figure 1.3: **National Emission Inventory (NEI) NO_x emission trend** — Trend for total NEI NO_x emission for 1970–2012. Data points prior to 1990 were reported every 5 years. 2006 and 2007 are interpolation of 2005 and 2008 data. After 2008, except for transportation, all other emissions were assumed constant. While some changes are real, some are due to changes in inventory methodology.

Global ANO_x emission has gradually decreased over the last two decades. *Müller* (1992) estimated a 72 Tg N/yr global emission for during the 1980's. The Intergovernmental Panel of Climate Change (IPCC) Third Assessment Report (AR3) estimated 28–32 Tg N from fossil fuel combustion, out of an approximately 50 Tg N annual global total NO_x sources at the end of the 20th century (*Schumann and Huntrieser*, 2007; *Lamarque et al.*, 2010, and references therein). In

[2] Emissions of NO_x from soil due to bacterial denitrification and biodecay are sometimes classified as biogenic emission.

particular, emission of $\mathrm{ANO_x}$ in the United States has been reduced substantially over the years. Figure 1.3 shows the NEI national trend expressed in thousands of tons of total $\mathrm{NO_x}$. The primary sources of $\mathrm{ANO_x}$ in the U.S. have been consistently dominated by the transportation and fuel combustion sectors, contributing to 63% and 29%, respectively, of the total $\mathrm{ANO_x}$. Comparing 2005 and 2008 NEI, $\mathrm{NO_x}$ from transportation has been reduced by 4.2% and $\mathrm{NO_x}$ from fuel combustion has been reduced by 21%. Such trend has also been observed through combined model-satellite studies (*Kim et al.*, 2009).

Similar to VOCs (Section 1.1.1), the reduction in $\mathrm{ANO_x}$ has gradually increased the relative importance of its natural counterparts. Nonetheless, the overall decline in $\mathrm{ANO_x}$ does not preclude the role of $\mathrm{ANO_x}$ in tropospheric ozone chemistry. Specifically, the co-location of $\mathrm{ANO_x}$ and various anthropogenic sources for VOCs continues to dominate the anthropogenic-factor of tropospheric ozone production (e.g. *Kim et al.*, 2011).

1.2 Parameterizing Lightning-generated $\mathrm{NO_x}$ ($\mathrm{LNO_x}$)

The global emission rate of $\mathrm{LNO_x}$ is highly uncertain and largely unconstrained because of the transient nature of lightning, thus introducing uncertainties in ozone climate simulations. The best current estimate for $\mathrm{LNO_x}$ is $5 \pm 3\,\mathrm{Tg\,N}$ per year globally, which contributes to around 10% of the total $\mathrm{NO_x}$ emission (*Schumann and Huntrieser*, 2007). Despite being a smaller direct source than $\mathrm{ANO_x}$, $\mathrm{LNO_x}$ has a comparable potential for ozone production due to its direct emission in the free troposphere, where it has a much longer lifetime than in the boundary layer (*Lamarque et al.*, 1996; *Allen et al.*, 2000; *Schumann and Huntrieser*, 2007, and references therein). *Hauglustaine et al.* (2001) used the Model for OZone And Related chemical Tracers (MOZART) to study the ozone produced from $\mathrm{LNO_x}$ and found ozone enhancement of over 140% at 250 mb in January above southern Atlantic, Africa, and south America. Similarly, *Cooper et al.* (2007) also found that the North American Monsoon upper tropospheric ozone enhancement, the central topic of this thesis, is largely due to $\mathrm{LNO_x}$.

1.2.1 Overview of lightning physics

Lightning flashes are the result of spontaneous electric discharges from accumulated charge volumes within a thunderstorm. Empirical studies point to the likelihood that the dominant electric charge generating process within convective systems is the non-inductive charge transfer arisen from the asymmetric elastic collisions between ice crystals and graupel within the updraft region (*Reynolds et al.*, 1957; *Jayaratne and Saunders*, 1985; *Saunders et al.*, 2006, and references therein). Charge separation is then promoted by the differential terminal velocities between particles of different sizes. Further charge transport is facilitated by the rapid convective motion within the storms. By observing changes in electric field measured from the ground. *Wilson* (1916) was the first to observe through experiments that thunderstorms typically exhibit a positive dipole structure, wherein positive charges are situated on top. More recent studies such as *Stolzenburg et al.* (1998) also suggested multipole structures within mesoscale convective systems (MCS) as illustrated in Figure 1.4. Regardless of the presumed charge structure, the initial charging zone is governed by the presence of a heterogenous mixture of frozen cloud particles, which leads to the temperature and microphysics dependence used by many parameterization.

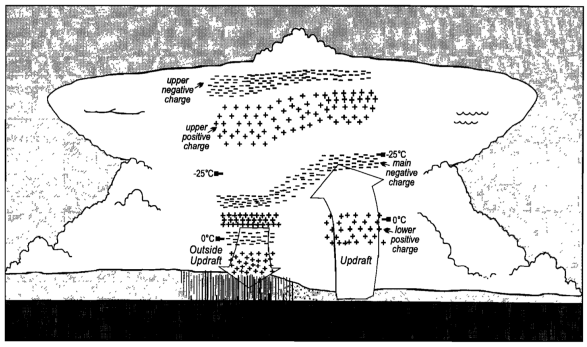

Figure 1.4: **Illustration of MCS electric charge structure from *Stolzenburg et al.* (1998)** — Illustration of a mesoscale convective system (MCS) with a multipole charge structure (after *Stolzenburg et al.*, 1998, Figure 3).

A common approach to modeling the triggering process given a charge distribution is the stochastic dielectric breakdown model formulated by *Niemeyer et al.* (1984); *Wiesmann and Zeller* (1986). For example, *Mansell et al.* (2002), in constructing an explicit scheme for lightning parameterization, used a height-varying initiation threshold with upper and lower bounds of $30\,\mathsf{kV\,m^{-1}}$ and $125\,\mathsf{kV\,m^{-1}}$. Once the threshold has been reached, a branched stepped leader (discrete connected

charged link) begins to form with an average downward propagation speed of $2 \times 10^5\,\mathsf{m/s}$ and peak pulse current $> 1\,\mathsf{kA}$ (*Uman and Krider*, 1989). For a negative cloud-to-ground (CG-) lightning, once the stepped leader (-) connects with an upward-moving discharge from the ground (+), a return stroke is formed. The first return stroke is typically one that carries most of the charges in a flash, with a median positive peak current is about 20–30 kA, but can exceed 200 kA (*Orville et al.*, 2010; *Cummins and Murphy*, 2009).

Discharging roughly $4 \times 10^8\,\mathsf{J\,flash^{-1}}$, lightning channels may reach a temperature in excess of $10,000\,\mathsf{K}$ during the first return stroke. This rapidly heated channel then expands and generates an outward-propagating shockwave, which is observed as thunder from afar. Finally, both the channel itself and the shock front are rapidly cooled through mixing. This rapid heating and cooling has been identified as the source for $\mathsf{LNO_x}$ (see Section 1.2.3).

1.2.2 Flash rate parameterization

A common first step to parameterizing $\mathsf{LNO_x}$ emission is to constrain the lightning flash count distribution. Many studies have attempted to reduce its spatiotemporal uncertainty through a combination of ground-based lightning detection instruments (e.g. *Boccippio et al.*, 2001; *Hansen et al.*, 2010), satellite-borne instruments (e.g. *Ushio et al.*, 2001; *Jourdain et al.*, 2010; *Martini et al.*, 2011), convective outflow measurements (e.g. *Pickering et al.*, 1998; *Skamarock et al.*, 2003), and chemistry transport models (e.g. *Price et al.*, 1997; *Allen et al.*, 2010, 2012; *Ott et al.*, 2010). Using the predicted flash rate, one may then deduce the $\mathsf{LNO_x}$ emission and its distribution once provided a method for flash-to-emission conversion, which will be discussed in the next section (Section 1.2.3).

Work by Bernard Vonnegut (1914–1997) laid down the theoretical foundation for a physically-based parameterization of lightning flash rate. Based on the works of *Vonnegut* (1963) and *Williams* (1985), *Price and Rind* (1992) constructed a lightning parameterization based on cloud-top height. The theoretical basis may be summarized as follow (after *Boccippio*, 2002).

Conceptualize the electric structure of a thunderstorm as two tangential spherical charge volumes of radius R and charge density $\pm\rho$. Compared to more recent studies, which point to tripole (*Williams*, 1989) or multipole (*Stolzenburg et al.*, 1998) charge structures, a dipole approximation is an obvious but reasonable simplification by accounting for the dominating region for charge separation. Then, assume an aspect ratio of unity, *i.e.* horizontal dimensions are similar in size to the vertical dimension. *Boccippio* (2002) noted the potential of an "at best" factor-of-two inaccuracy under this assumption. A third simplification asserts that the dipole is maintained through a generator current modeled as a net charge transport velocity. Finally, it is assumed that the variation of this current is small. Expressing the generator power as a product of the generator current (I) and the electric potential of the dipoles (Φ), we have $P = I\Phi$. Applying the definitions of I and Φ and applying Gauss' Law, *Boccippio* (2002) writes [3]

$$P \sim \varepsilon^{-1}\rho^2 V_Q A z_d^2 \tag{1.10}$$

where V_Q is the charging velocity, $A = \pi R^2$ is the horizontal cross-section area of the charge volume, and $z_d = 2R$ is the dipole separation. Hence a fundamental conclusion is arrived here stating that the geometric term dominates the generator power. If power dissipation by lightning varies monotonically with the generator power and that each flash dissipates a constant amount of energy, then flash rate f is proportional to the generator power P and we write

$$f \sim \rho^2 V_Q A z^2 \tag{1.11}$$

Here, z_d has been simplified to storm height z. Three more final assumptions on storm properties can be made to make this relationship operationally viable. (1) Applying the assumption on the storm aspect ratio, A is replaced with z^2. (2) Using w as the best approximation for V_Q. (3) Charge density has negligible variability at least within the dominant dipole regions. These simplifications produce the following relationship.

$$f \sim w z^4 \tag{1.12}$$

[3] Assuming different charge geometry can lead to a different scaling relationship, e.g. asserting 2D charge plates instead of spheres would lead to $P \sim \rho_{gen} V_Q R^2 z_d E_{crit}$ (*Boccippio*, 2002).

Compiling data from several studies between 1962 – 1979, *Williams* (1985) observed a linear relationship between vertical velocity and cloud size for continental storms. This empirical relation allows one to further simplify 1.12 to obtain the continental flash rate f_c:

$$f_c \sim z^5 \tag{1.13}$$

This scaling relationship has been shown to be operationally viable in several studies (e.g. *Yoshida et al.*, 2009; *Ushio et al.*, 2001). Compiling data from *Williams* (1985), the empirical relationship of flash rate and cloud top height for continental storm is written as (*Price and Rind*, 1992, hereafter PR92)

$$f_c(z) = 3.44 \times 10^{-5} z^{4.9} \tag{1.14}$$

Alternatively[4] , f_c may be written as a function of the maximum updraft velocity $w_{\max}$, giving $f_c \sim w_{\max}^{4.54}$. While the linear relationship between $w_{\max}$ and cloud top height in continental clouds is confirmed by *Price and Rind* (1992), w_m for marine clouds appear to scale much slower with cloud size:

$$w_m = 2.86 z^{0.38} \tag{1.15}$$

Subsequently, a separate parameterization for marine clouds is formulated as $f_m = 6.2 \times 10^{-4} z^{1.79}$. Due to the lack of data, the marine relationship is not tested thoroughly and thus Equation 1.15 has been frequently challenged. *Michalon et al.* (1999), taking into account the effects of marine cloud condensation nuclei (CCN), rewrites f_m as $6.57 \times 10^{-6} z^{4.9}$. However, this has been quickly shown to produce excessive flash rates (**?**). Soon after, *Boccippio* (2002) shows that PR92's marine formulation is formally inconsistent with *Vonnegut* (1963) by correlating continental flash rates with marine cloud top heights, *i.e.* $f_c(z_m)$.

Price and Rind (1993) used the flash data from eleven states in the western United States, detected by wide-band magnetic direction finders, in combination with thunderstorm radar and radiosondes data to find a relation for the IC:CG ratio (Z) from cold-cloud depth (d), defined as

[4] *Baker et al.* (1995) theoretically derived $f_c \sim w^6$ instead.

the distance from the freezing level to cloud-top.

$$Z = 0.021d^4 - 0.648d^3 + 7.49d^2 - 36.54d + 63.09 \tag{1.16}$$

In *Price and Rind* (1994), a "calibration factor" (c) for the resolution dependency of PR92 is introduced by regridding 5 km data between 1983 and 1990 from the International Satellite Cloud Climatology Project data set (ISCCP; *Rossow and Schiffler*, 1991) to different horizontal grid sizes. The resulting equation is as follow

$$c = 0.97241 \exp(0.048203 \Delta A^\circ) \tag{1.17}$$

where ΔA° is the grid area in squared degrees. *Price and Rind* (1994) claims that there is no dependence of c on latitude, longitude, or season.

Other bulk-scale or resolved-scale storm parameters may also be correlated with lightning flashes for the purpose of formulating alternative parameterization schemes. For instance, *Allen and Pickering* (2002) and *Allen et al.* (2010) implemented a parameterization of flash rate to the square of deep convective mass flux. *Zhao et al.* (2009) and *Choi et al.* (2005) based the flash rate prediction on both the deep convective mass flux and the convectively available potential energy (CAPE). *Allen et al.* (2012) used a flash rate prediction scheme based on the convective precipitation rate. *Petersen et al.* (2005) gave a linear relation between flash rate and ice water path (IWP). *Deierling and Petersen* (2008) investigated a linear dependence of flash rate on updraft volume for $T < 273\,\mathsf{K}$ and $w > 5\,\mathsf{m\,s^{-1}}$. *Hansen et al.* (2012) produced a lookup-table for flash rate from convective precipitation and mixed phase layer depth by correlating data from observations. *Barthe et al.* (2010) compared several of these methods including PR92, through two case studies, and showed that while the polynomial orders are lower in the non-cloud-top based formulations, the level of uncertainties may still be higher than PR92 due to a combination of errors from model biases in the parameters used, e.g. hydrometeors, and observational biases in the datasets used for constructing the relationships. *Futyan and Del Genio* (2007) arrived at a similar conclusion about the reduced reliability of precipitation-based approaches in global climate simulations for

predicting lightning flash rate. Explicit schemes, wherein electrification within convective cells are resolved, also exist (e.g. *Barthe et al.*, 2005; *Zhang et al.*, 2003). However, they are often too costly for synoptic modeling and thus their usages are limited to single-storm case studies.

1.2.3 Lightning-generated $\mathsf{NO_x}$

Lightning-generated $\mathsf{NO_x}$ ($\mathrm{LNO_x}$) is produced shortly following a channel formation. One prevalent theory for explaining $\mathrm{LNO_x}$ production is the shockwave heating theory, which describes NO molecules being formed in the air surrounding the lightning channel according to the Zel'dovich mechanism (*Zeldovich*, 1966; *Borucki and Chameides*, 1984, and references therein): When the cylindrical shock is propagating outwards from the current, air is heated to $\sim 2500\,\mathsf{K}$ at the shock front, which produces a high NO-to-$\mathsf{N_2}$ equilibrium ratio. Behind the shock front, air is rapidly cooled to the ambient temperature, which "freezes" the NO-to-$\mathsf{N_2}$ ratio obtained at the prior instant. However, *Stark et al.* (1996) argued that the shockwave does not travel fast enough to produce the necessary temperature for Zel'dovich mechanism.

Using experimental data, *Wang et al.* (1998) relates the production of NO (in $10^{21}\,\mathsf{molecules/m}$) to peak current ($I$) and pressure ($p$):

$$n_{\mathsf{NO}}(I) = 0.14 + 0.026I + 0.0025I^2 \tag{1.18}$$

$$n_{\mathsf{NO}}(p) = 0.34 + 1.30p \tag{1.19}$$

The correlation factor (r^2) for the above fits to measurements are 0.89 and 0.67 respectively, but it should be noted that the coefficients in Equation 1.18 have significant relative uncertainty (± 0.33, ± 0.036, ± 0.0009 respectively).

Using the mean peak current from remote sensing measurements, *Price et al.* (1997) estimated that intracloud (IC) flashes produce only 10% of the energy produced by cloud-to-ground (CG) flashes and thus deducing that the moles of NO per flash from IC is also a factor of 10 smaller than that from CG, which is calculated at 1.1 kmoles per CG flashes. However, more recent studies have found that such ratio is grossly overestimated and that both IC and CG flashes produce

approximately the same amount of NO. *Ott et al.* (2010) estimated 500 moles NO per flash or 7 kg N per flash with a range of 360–700 moles NO per flash. This is compared to a calculation using the median peak current from North American Lightning Detection Network (NALDN; *Orville et al.*, 2002) and relationship in *DeCaria et al.* (2000) after *Wang et al.* (1998).

After the total emission of a flash is estimated, one may want to assign a spatial distribution to the molecules. In models that are capable of resolving explicit electrification, flash path, and stroke tortuosity (e.g. *Mansell et al.*, 2002), those details may be leveraged in combination with Equation 1.19 to compute the vertical distribution (*Barthe and Pinty*, 2007). In regional models, a fixed column profile based on cloud extent or observations are often used instead. *DeCaria et al.* (2000) prescribes a Gaussian-like distribution for emissions from CG flashes and a bimodal distribution for IC flashes. Horizontal distribution based on 20 dBZ reflectivity is also proposed by *DeCaria et al.* (2005) based on *MacGorman and Rust* (1998). *Pickering et al.* (1998) derived total LNO_x profiles with a peak at the detrainment level and a maximum in the boundary layer by using measurements from multiple campaigns and 2D models. *Ott et al.* (2010) corrected these profiles by using a 3D model, and found that convective updraft removes the boundary layer maximum and places a single maximum at 6–9 km for midlatitude storms. *Hansen et al.* (2010) also investigated the vertical distribution of flash segments for four storms and found that profiles can exhibit large variabilities.

Several modeling studies have approached LNO_x parameterization using scaling/assimilation techniques. For example, *Hudman et al.* (2007) used the 500 moles NO per flash from *Ott et al.* (2010) in combination of NLDN CG flash counts adjusted by IC:CG ratio suggested by *Boccippio et al.* (2001). *Jourdain et al.* (2010) scaled flash rates regionally to Optical Transient Detector/Lightning Imaging Sensor (OTD/LIS *Boccippio et al.*, 2000) monthly and 44 flashes/s globally annually to be consistent with climatology from *Christian et al.* (2003). The scaled LNO_x strength is further constrained using observation of O_3 by Tropospheric Emission Spectrometer (TES *Beer*, 2006). *Schumann and Huntrieser* (2007, Table 24) also compiled a list of 78 studies with dependence on

LNO_x production rate since 1981 and found that large number of studies without sufficient a priori reasons for choosing their prescribed source strength.

In conclusion, lightning parameterization remains a major uncertainty in tropospheric ozone modeling. Many methods have been proposed with varying degrees of generality and complexity. This study has elected to use the simplest method available for flash rate parameterization, *i.e. Price and Rind* (1992), which is evaluated in depth in Chapter 2.

1.3 Summary

This chapter has summarized various aspects of ozone chemistry relevant to the upper tropospheric ozone enhancement studied by *Li et al.* (2005) and *Cooper et al.* (2007). While residing in the upper troposphere, due to the nonlinearity of the O_3-VOC-NO_x chemistry, the ability to simulate and analyze the ozone enhancement depend heavily on the model's skill in simulating vertical transport (convective or advective), chemistry, as well as prescribing or parameterizing emissions. Of the three primary emission sources (anthropogenic, biogenic, and lightning), lightning NO_x is the least well-constrained because of its transient nature and its sensitivity to cloud parameters, for which the values will be obtained from parameterized convection in this study. Furthermore, *Cooper et al.* (2009) found that the ozone enhancement depends strongly on lightning emission. Therefore, before conducting the modeling study to understand the upper tropospheric ozone enhancement (Ch. 3), the parameterization of lightning emission is evaluated and discussed in depth Ch. 2.

Even though previous studies have already investigated the enhancement phenomenon and shown with confidence the contributions from dynamics and emissions to the inter-annual variability, little research has been done in understanding the spatiotemporal structure of the chemistry at higher granularity. Using a single high-resolution model, *Barth et al.* (2012) showed substantial daily variability during the 2006 North American Monsoon. By trading off resolution and accuracy especially in convection, this study mimics *Barth et al.* (2012) and supplements its results with

additional diagnostics and sensitivity simulations. Reiterating the goals stated at the beginning of this chapter, and given the additional background information on the intricacy of studying upper tropospheric ozone, this thesis intends to answer the following questions:

(1) Trading off model resolution and parameterizing convection, how well can the model simulate the ozone enhancement? This will be addressed through detailed validation exercises against various observations in Chapter 3.

(2) Considering the various factors controlling ozone, what is the relative importance of each component to the overall ozone level? By using various diagnostics and techniques, this question will be addressed in Chapter 4.

(3) Focusing on each emission source, how sensitive is the ozone enhancement to various scenarios? Separate simulations are performed by varying emission parameters, this is evaluated in Chapter 4.3.

Chapter 2

Lightning parameterization

Over the last decade, predictions of lightning flash statistics in numerical weather and climate models have garnered increasing interests. One of the likely drivers is the advances in online chemistry models, wherein chemistry is simulated alongside of physics (e.g., *Grell et al.*, 2005). Lightning-generated nitrogen oxides (LNO_x) are predicted to be very efficient in accelerating the production of tropospheric ozone, which is identified as a significant greenhouse gas in the upper troposphere (*Lacis et al.*, 1990; *Kiehl et al.*, 1999). *Cooper et al.* (2007) showed that , lightning can contribute 25–30 ppbv of upper tropospheric ozone during the summertime North American Monsoon. *Choi et al.* (2009) has remarked on the increasing importance of LNO_x in tropospheric ozone production as anthropogenic sources of NO_x are being reduced in the United States. Furthermore, the inherent nonlinearity between NO_x emission and commonly validated quantities such as radiative balances and ozone concentration makes it challenging to quantify the skill of a LNO_x parameterization through proxy or total NO_x measurements. Therefore, it is important to evaluate existing lightning parameterizations by directly validating flash rate predictions in order to more accurately interpret results from models that incorporate LNO_x emission.

The most commonly used method for parameterizing lightning flash rate is perhaps that by *Price and Rind* (1992, 1993, 1994). It has been used by chemistry transport modeling studies such as GEOS-Chem (*Hudman et al.*, 2007), MOZART-4 (*Emmons et al.*, 2010), and CAM-Chem (*Lamarque et al.*, 2012). Continental flash rates are related to the fifth-power of cloud-top height by *Williams* (1985) and *Price and Rind* (1992, hereafter PR92) through empirical evidences that

are consistent with the theoretical scaling arguments of *Vonnegut* (1963). The partitioning between intracloud and cloud-to-ground flashes, or IC : CG ratio, is estimated with a fourth-order polynomial of cold cloud-depth, i.e., distance between freezing level and cloud-top, in *Price and Rind* (1993, hereafter PR93). Finally, the parameterization is generalized for different grid sizes with an extrapolated "calibration factor" in *Price and Rind* (1994, hereafter PR94).

The goals of this study are to evaluate the cloud-top height based parameterization (PR92, PR93, and PR94) across the bridging resolutions between those commonly used by global chemistry models ($\Delta x \sim \mathsf{O}(1^\circ)$) and cloud-resolving models ($\Delta x < 5\,\mathsf{km}$), and report on statistics over time periods useful for studying upper tropospheric chemistry ($\mathrm{O}(\mathsf{month})$) (*Stevenson et al.*, 2006). It is, however, not the goal of this study to invalidate previous studies, but to draw attention to the need for careful implementation and validation of the use of these parameterizations. Here we report on experiments using PR92, PR93, and PR94 implemented into the Weather Research and Forecasting model (WRF; *Skamarock et al.*, 2008), focusing on results from simulations performed at 36 km and 12 km grid-spacing. A simulation at 4 km grid spacing for 2 weeks in July and August 2006 is also analyzed to demonstrate how PR92 behaves transitioning from cloud-parameterized to cloud-permitting resolutions and provide insights on how or whether such transition can be done.

Similar studies have been performed for global models (e.g., *Tost et al.*, 2007), but previous regional-scale modeling studies utilizing PR92 at comparable horizontal grid spacings have not provided evaluations of the lightning parameterization. Thus, there has been insufficient information to understand the behavior of PR92 in this regime. Even though these formulations were derived using near-instantaneous data at a cloud-permitting resolution (5 km), past applications often utilize temporally and spatially averaged cloud-top height outputs or proxy parameters. While the effects of spatial averaging is addressed by the PR94 scaling factor, effects of temporally averaging cloud-top heights are rarely addressed and may lead to significant underestimation due to the fifth-power sensitivity (*Allen and Pickering*, 2002). Addressing the potential issue of temporal averaging, instantaneous cloud-top heights and updraft velocities at each time step are leveraged. Comparisons are then performed for temporal, spatial, and spectral features.

The next section (Sect. 2.1) outlines the methods used in this study, which includes the formulation and overview of the parameterization (Sect. 2.1.1), relevant aspects of the model setup, practical considerations of implementing PR92 (Sect. 2.1.2), and the data used for validation (Sect. 2.1.3). Section 2.2 describes the model results and discusses the implications of various statistics from validation against observations of precipitation, flash rate, and IC : CG ratios. Section 2.3 discusses how the performance of PR92 transitions between different resolutions (Sect. 2.3.1) and between theoretically similar formulations (Sect. 2.3.2). Finally, Sect. 2.4 provides a summary of key results and cautionary remarks on specific aspects of the utilization of PR92, PR93, and PR94.

2.1 Methods

2.1.1 Parameterization overview

In PR92, a fifth-power relation between continental lightning flash rate (f_{c}) and cloud-top height (z_{top}) is established with observational data following the theoretical and empirical frameworks of *Vonnegut* (1963) and *Williams* (1985). Assuming a dipole structure with two equal but opposite charge volumes and a cloud aspect ratio of approximately one, it is first formulated, based on scaling arguments of *Vonnegut* (1963), that the flash rate would be proportional to maximum vertical updraft velocity ($w_{\max}$) and fourth-power of cloud dimension. Imposing a linear relation between $w_{\max}$ and cloud dimension, the flash rate relationship can be reduced to fifth power of z_{top} (*Williams*, 1985). It is empirically fit to radar and flash rate data from several measurements between 1960–1981 to give the continental equation (*Price and Rind*, 1992):

$$f_{\mathsf{c}}(z_{\mathsf{top}}) = 3.44 \times 10^{-5} z_{\mathsf{top}}^{4.9}. \tag{2.1}$$

PR92 also estimated that $w_{\max} = 1.49 z_{\mathsf{top}}^{1.09}$ for continental clouds, thus allowing a second formulation based on maximum convective updraft:

$$f_{\mathsf{c}}(w_{\max}) = 5 \times 10^{-6} w_{\max}^{4.54}. \tag{2.2}$$

Table 2.1: WRF simulations performed for lightning parameterization study.

Case #	dx (km)	dt (s)	Output	Duration
1	36	90	hourly	JJA 2006
2	36	90	hourly	JJA 2011
3	12	36	3-hourly	Jul 2011
4	4	12	hourly	25 Jul–7 Aug 2006

A separate formulation of second-order, instead of fifth-order, is also derived by *Price and Rind* (1992) for marine clouds, for which updraft velocity is observed to be significantly slower:

$$f_{\mathsf{m(PR92)}}(z_{\mathsf{top}}) = 6.2 \times 10^{-4} z_{\mathsf{top}}^{1.73}. \tag{2.3}$$

Taking into account effects from cloud condensation nuclei, *Michalon et al.* (1999) modified the marine equation to fifth-order:

$$f_{\mathsf{m(M99)}}(z_{\mathsf{top}}) = 6.57 \times 10^{-6} z_{\mathsf{top}}^{4.9}. \tag{2.4}$$

The practical viability of the continental relation was proven by *Ushio et al.* (2001) and *Yoshida et al.* (2009) through several case studies. However, *Boccippio* (2002) showed that the marine equations are formally inconsistent with *Vonnegut* (1963), and that the marine equations cannot be inverted to produce cloud tops within the range of cloud-top observations.

Price and Rind (1993) used the flash data from eleven states in the western United States, detected by wide-band magnetic direction finders, in combination with thunderstorm radar and radiosondes data to find a relation for the IC : CG ratio (Z) from cold-cloud depth (d), defined as the distance from freezing level to cloud-top.

$$Z = 0.021d^4 - 0.648d^3 + 7.49d^2 - 36.54d + 63.09 \tag{2.5}$$

In *Price and Rind* (1994), a "calibration factor" (c) for the resolution dependency of PR92 is introduced by regridding 5 km data between 1983 and 1990 from the International Satellite Cloud Climatology Project dataset (ISCCP; *Rossow and Schiffler*, 1991) to different horizontal grid sizes.

The resulting equation is as follows:

$$c = 0.97241 \exp(0.048203R) \tag{2.6}$$

where R is the grid area in squared degrees. *Price and Rind* (1994) claim that there is no dependence of c on latitude, longitude, or season. For the grid sizes used in this study, the values of c are 0.9774 for 36 km, 0.973 for 12 km, and 0.9725 for 4 km.

2.1.2 Model setup and implementation

Simulations in this study are performed using the Weather Research and Forecasting (WRF) model version 3.2.1 (*Skamarock et al.*, 2008) over the contiguous United States (CONUS), including part of Mexico and Canada (Fig. 2.1). The simulations have slightly different model domains because the simulations were developed and performed for objectives independent of validating the lightning parameterization. Meteorology is initialized and continuously nudged (horizontal winds, temperature, water vapor) with the National Center for Environmental Prediction (NCEP) Global Forecasting System (GFS) final (FNL) gridded analysis at 6 h intervals (00:00 UTC, 06:00 UTC, 12:00 UTC, 18:00 UTC). Four simulations are performed (Table 2.1), two at 36 km grid spacing, one at 12 km grid spacing, and one at 4 km grid spacing. All cases use the same vertical coordinates with 51 sigma levels up to 10 hPa. The Grell–Devenyi ensemble convective parameterization (*Grell and Devenyi*, 2002) with *Thompson et al.* (2008b) microphysics is used for the simulations where grid-spacing $\Delta x > 10$ km, for which a convective parameterization is needed. The implementation of the GD scheme employed in this

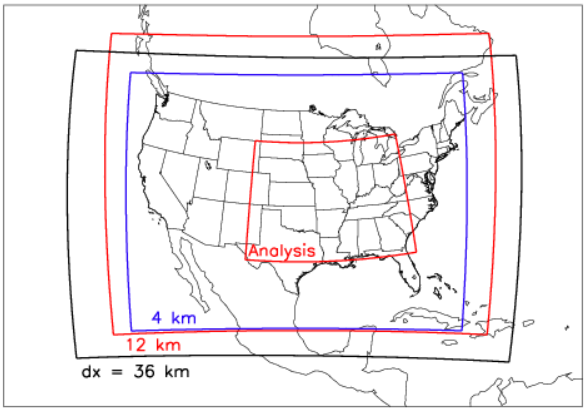

Figure 2.1: **Domain for lightning simulations** — Non-nested domains for WRF simulations and region for lightning simulations.

study consists of $3 \times 3 \times 16 = 144$ ensemble members comprising of interactions between different dynamic control and static control/feedback closures. The maximum moist static energy (MSE) is then used as input with entrainment to calculate the level neutral buoyancy (LNB), or cloud top. For further information about the convective parameterization, readers are encouraged to refer to *Grell* (1993).

Since the simulations were designed independently, some physics options used are not consistent. The planetary boundary layer (PBL) parameterization is handled by the Yonsei University scheme (*Hong et al.*, 2006) at 36 km and Mellon–Yamada–Janjic (MYJ) scheme (*Janjić*, 1994) at 12 km and 4 km. At 36 km, the surface layer physics option used is based on Monin–Obukhov similarity theory. The surface layer option used at 12 km and 4 km is also based on Monin-Obukhov theory but includes Zilitinkevich thermal roughness length.

While theoretically the scaling argument of *Vonnegut* (1963) does not distinguish between definitions of cloud-top height, the data used to derive the PR92 relation are radar reflectivity cloud-top heights at a certain reflectivity threshold. In the WRF implementation of Grell–Devenyi convective parameterization, the level of neutral buoyancy (LNB) is computed, with convective entrainment and detrainment accounted for within the calculation of cloud moist static energy, and readily available as a proxy for sub-grid cloud-top height. Thus, instead of 20 dBZ reflectivity cloud top, z_{top} is approximated by reducing LNB by 2 km, which will be shown to produce results within the range of the observed values. Section 2.5 contains detailed discussions of the choice of 2 km cloud-top reduction and how it compares to offline computations of 20 dBZ cloud tops. Alternative methods for estimating the difference between the two heights can be formulated by directly taking into account their respective definitions. However, echoing *Barthe et al.* (2010), such addition of complexity increases the number of sources for uncertainty, especially in the context of parameterized convection. Similarly, using modeled cloud particle variables would also add an additional level of sensitivity due to sub-grid variability in hydrometeor mixing ratios. Therefore, reflectivity calculations are only performed in the 4 km simulation and only for the purpose of redistributing lightning flashes horizontally as described below.

For case 4 (Table 2.1), convection is explicitly simulated with a modified *Lin et al.* (1983) microphysics scheme. Since no convective parameterization is used, the resolved maximum vertical velocities ($w_{\max}$) within the convective core are utilized (*Barth et al.*, 2012), and Eq. (2.2) is used instead of Eq. (2.1) for estimating flash rate. In addition, since a single storm may often cover multiple model grids, flashes are redistributed to within regions with a minimum reflectivity of 20 dBZ calculated using hydrometeor (rain, snow, graupel) information that is now better constrained at 4 km. The IC : CG ratio is prescribed using a coarse version of the *Boccippio et al.* (2001) 1995–1999 climatological mean, which was computed using data from the Optical Transient Detector (OTD; *Boccippio et al.*, 2000) and the National Lightning Detection Network (NLDN; *Cummins and Murphy*, 2009). Because PR92 developed Eq. (2.2) based on data at 5 km resolution, no resolution scaling is done to this simulation. Because this particular simulation was driven by the meteorology of its own WRF outer domains, it is restarted "cold" on 2 August to be consistent with the outer domain meteorology.

Most of the implementations used in these simulations are arguably "untuned" and not scaled to climatology or observations by any additional tuning factors, with the exceptions of the 2 km cloud-top height reduction used in the cases with parameterized convection and the prescribed climatological IC : CG ratios in case 4. Therefore, the correctness and predictiveness of the flash rate parameterization are not guaranteed at the time of the simulation given the lack of supporting validations of PR92 at the tested grid spacings. However, without feedback to the meteorology (except in case 4) and providing sufficient linearity in the biases of flash prediction, offline comparisons should reveal any tuning requirements for operational and research uses.

2.1.3 Data description

While desirable, event-by-event analysis would be technically challenging because the simulation may not produce the same strength, timing, and location of each convective event. Furthermore, an event-by-event analysis is unnecessary in the context of a mesoscale upper tropospheric chemistry study, of which the meaningful timescales often average biases from many individual

events. Therefore, a large area where thunderstorms commonly occur is selected. The "analysis domain," defined as 30°– 45°N, 80°– 105°W (Fig. 2.1), is used for time series and statistical comparisons.

The predicted lightning properties depend strongly on how the model simulates convection. Thus, in Sect. 2.2.1, WRF simulated precipitation is compared against National Weather Service (NWS) precipitation products to evaluate the model's skill in representing convective strengths. The data are collected from radars and rain gauges and improved upon using a Multi-sensor Precipitation Estimator (MPE). Manual post-analyses are then performed by forecasters to identify systematic errors (http://www.srh.noaa.gov/abrfc/?n=pcpn_methods). The final data products used here are mosaic CONUS precipitation maps from 12 River Forecast Centers (RFCs) during JJA 2006 and 2011. The data are gridded into 4 km resolution and are available as 24 h totals over a hydrological day beginning and ending at 12:00 UTC.

The simulated CG flash counts, computed online as predicted total flashes × predicted CG fraction, are compared against data from the Vaisala US National Lightning Detection Network (NLDN; *Cummins and Murphy*, 2009). The network provides continuous multiyear CONUS and Canada coverage of $> 90\,\%$ of all CG flashes with ongoing network-wide upgrades (*Orville et al.*, 2002, 2010). The median location accuracy is 250 m, which is well within the resolutions employed in this study. Multiple strokes are aggregated into a single flash if they are within 1 s and no more than 10 km apart. Weak positive flashes with < 15 kA have been filtered from all data. Finally, the flash data are binned into hourly flash counts for each model grid cell for comparison against model output.

Data from Earth Networks Total Lightning Network (ENTLN), previously WeatherBug Total Lightning Network (WTLN), are used to validate the model-produced IC : CG ratios. ENTLN employs a wide-band system that operates between 1 Hz to 12 MHz (*Liu and Heckman*, 2011). The theoretical detection efficiency (DE) for CG flashes across CONUS is 90–99 %, while the IC DE falls between 50–95 % (50–85 % within the analysis domain). Since the mappings of the corresponding DEs are not available with the data, 95 % and 65 % are used for CG and IC DEs, respectively,

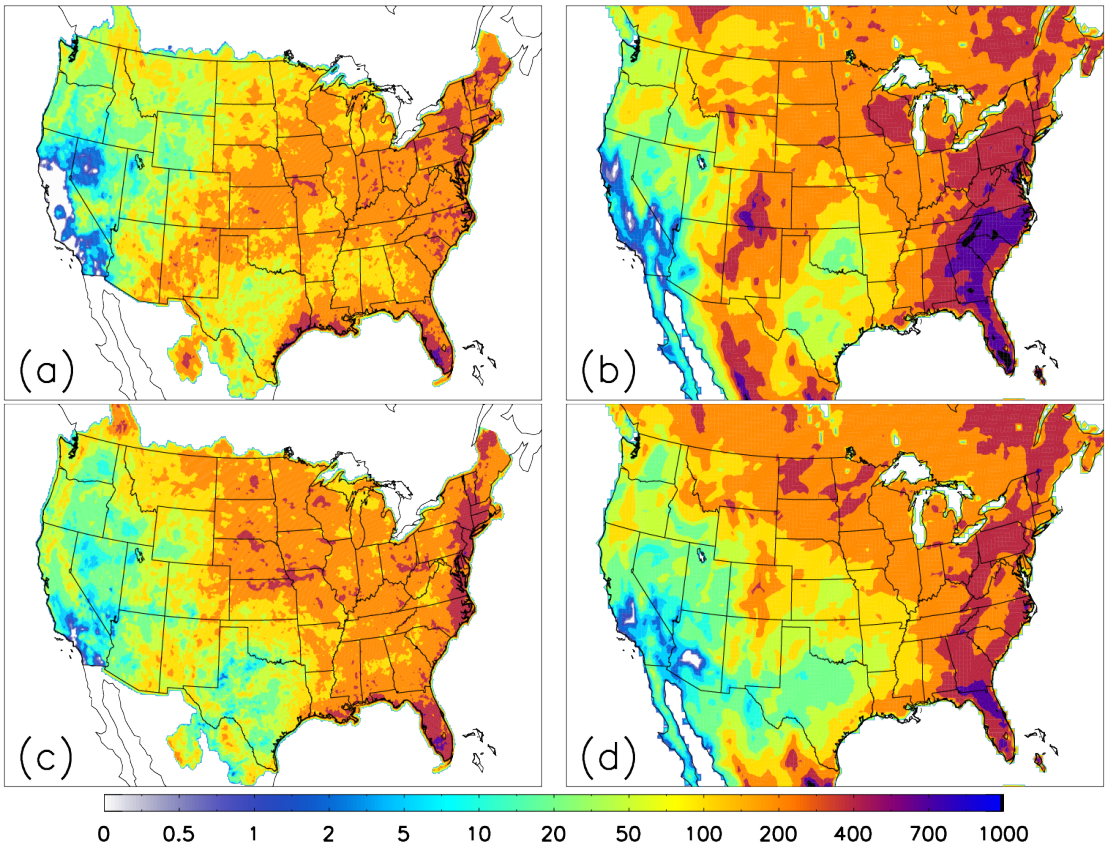

Figure 2.2: **Spatial distribution of JJA total precipitation in 2006 and 2011** — Spatial distribution of 2006 and 2011 JJA total precipitation in millimeters. **(a)** and **(c)** are NWS precipitation degraded to 12 km resolution. **(b)** and **(d)** are 36 km WRF-simulated total precipitation over the same periods with data above water surfaces masked out.

in analyses for which a prescribed DE is required. To address the concern of the impact of this simplification, the range of possible flash counts, IC : CG ratios, and biases will be provided when appropriate within the discussion in Sect. 2.2 to place bounds on the uncertainty. Due to the limited deployment duration of the network, only the IC : CG ratios during JJA 2011 within the analysis domain (see Fig. 2.1) are estimated and compared. For consistency with the comparisons against NLDN CG flash counts, the stroke aggregation criteria used here are 10 km and 1 s as done by NLDN, instead of the 10 km and 700 ms window typically used by Earth Networks to generate flash statistics.

2.2 Results and discussions

2.2.1 Precipitation

While lightning does not directly depend on precipitation, they are both the results of the same processes that promote ice–graupel collisions. Further, precipitation is observed robustly and continuously, thus giving us a high quality measurement for validating model results. On the other hand, while convective mass flux may produce a more consistent correlation with lightning, the lack of well-controlled direct observations and the large uncertainty in model calculations make it an inferior proxy for convective strength in this context.

Figure 2.2 shows the total precipitation during JJA 2006 and 2011 over the CONUS as simulated at 36 km grid spacings by WRF and observed by NWS. The gradients across the CONUS for both years are well captured by the model, but WRF has a high bias for 2006. WRF also simulates up to an order of magnitude more precipitation for coastal regions for both years but primarily for 2006. The time series for mean daily area-averaged precipitation and frequency distributions for JJA 2006 within the analysis domain (Fig. 2.3a and c) also reveal a median model bias of 37 %. In particular, WRF predicted more than twice the precipitation between late-June and mid-July in 2006. In contrast, the median bias for 2011 is 4.9 % with almost equal occurrence of over- and under-predictions. The model frequency distribution for both years also closely track

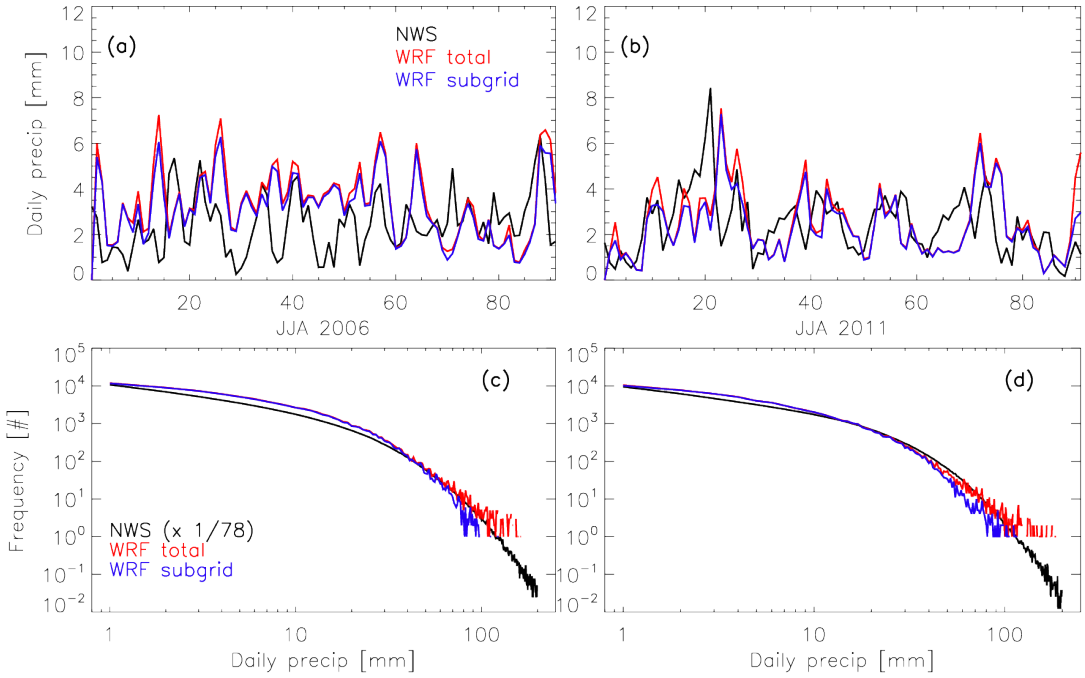

Figure 2.3: **Time series and frequency distribution for 2006 and 2011 daily precipitation** — Time series and frequency distributions for JJA 2006 and 2011 area-averaged daily precipitation within the analysis region (see Fig. 2.1). Distributions for NWS are scaled by the ratios between total grid counts in WRF at 36 km and total grid counts in NWS within the analysis boundaries ($\sim$ 1/78). WRF subgrid is the portion of precipitation from subgrid cumulus parameterization. Only grid points with more than 1 mm of precipitation are included.

those observed (Fig. 2.3c and d) except at the high end of the distribution where limits of model grid resolution induces significant noise.

The simulated daily precipitation at 12 km is higher than the NWS observed precipitation by 24 % during July 2011. However, an anomalously strong diurnal cycle is simulated at 12 km grid spacing that is not present in the 36 km simulation. Comparing the area-averaged 12 km nocturnal precipitation over the entire analysis domain to that of 36 km output, nocturnal precipitation at 12 km is too low but the daytime precipitation is too high. One-day simulations were performed to evaluate the impact from the differences in model physics, but there remained significant unidentified discrepancies between the precipitation amount in the two runs that cannot be explained by horizontal resolution differences alone; thus, it is concluded that there is no value in redoing the entire simulation. The identified causes for the differences between the two simulations are, in decreasing order for magnitude of influence, initial conditions for soil temperature and soil moisture, differences in planetary boundary layer scheme (Sect. 2.1.2), and the land surface model option. Such difference in diurnal behavior in the simulations is expected to have significant impact on how the lightning parameterization is evaluated, but the full impact can be minimized through incorporation of precipitation into the analysis.

Large scale meteorology and moisture inputs are unlikely the causes for these biases due to nudging. In 2006, biases mostly occurred in the low-to-mid end of the distribution (i.e., light precipitation events, Fig. 2.3c), indicating that the problem lies in parameterizing subgrid events. Despite the differences in the eastern United States, convection over the central United States is reasonably represented. Finally, the goal of this study is not to evaluate the convective parameterization nor specific model setup, but rather to evaluate the performance characteristics of the lightning parameterization when implemented into a regional model with all the expected (and unexpected) defects.

2.2.2 CG flash rate

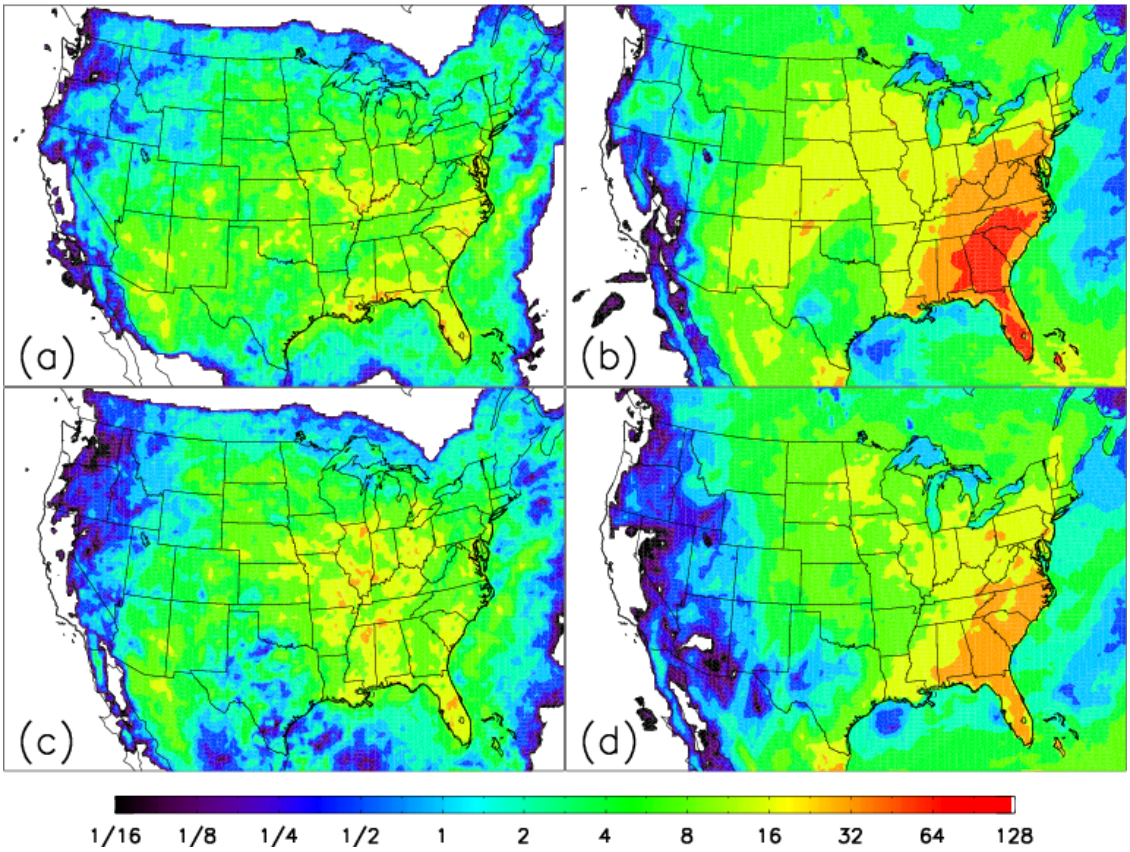

Figure 2.4: **Spatial distribution of NLDN and WRF-predicted CG flash counts** — Total CG flashes in number per km^2 per full-year during JJA 2006 (first row) and 2011 (second row). First column (**a** and **c**) shows the NLDN observed density gridded to WRF 36 model grid, and second column (**b** and **d**) shows the modeled flash density output by WRF at 36 km.

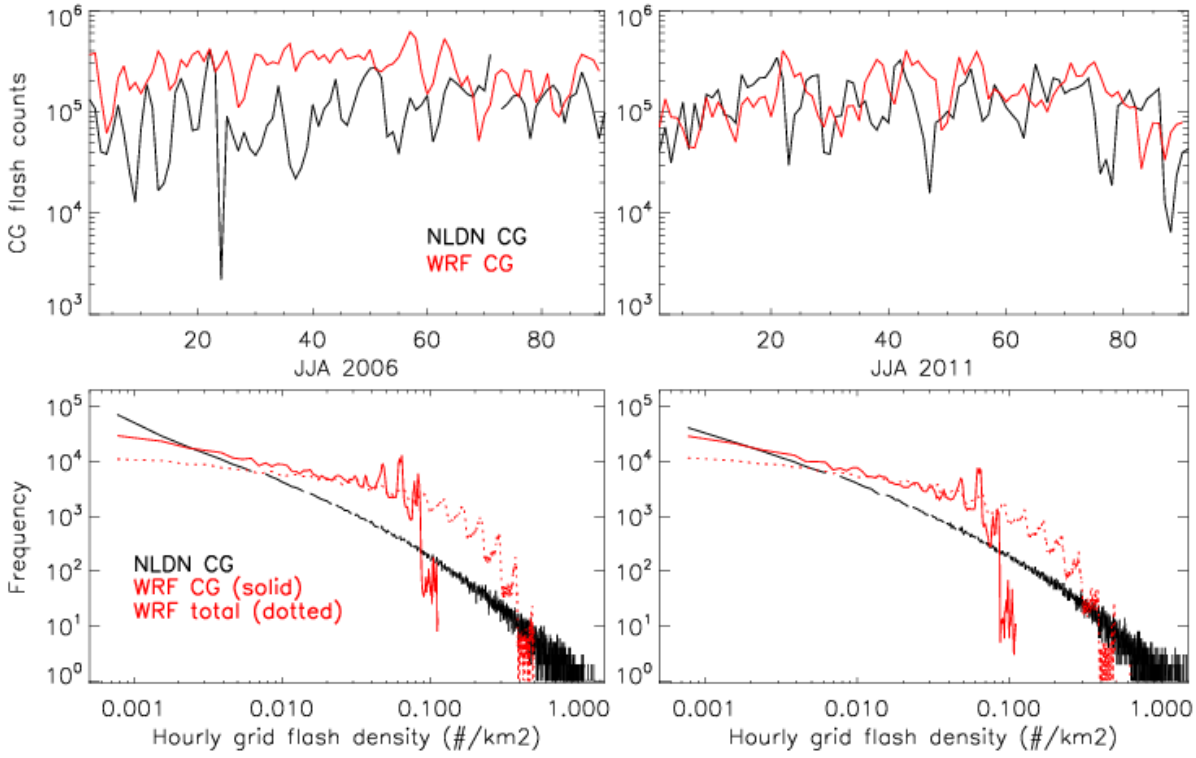

Figure 2.5: **NLDN and WRF CG flash counts** — Comparisons of time series and frequency distributions between NLDN CG flash counts (black) and WRF predicted CG flash counts (red) at 36 km within the analysis domain defined in Fig. 2.1. Total flash counts predicted by WRF are shown as dotted red lines.

Figure 2.4 shows the CONUS CG flash density (units in number per km^2 per year). WRF is consistently higher along the East Coast for 2006 where positive bias is also observed in the modeled precipitation, which is used as a proxy for quantifying the comparison of simulated convective strength against observations. Similarly, both flash rate and precipitation are over-predicted in the Colorado and New Mexico region for 2006. On the other hand, the low precipitation bias in Arizona simulated by WRF for 2011 is coincident with a severe low bias in the same region for the CG flash density. Otherwise, flash densities are within the order of magnitude of those observed for regions where simulated precipitation is consistent with NWS observations.

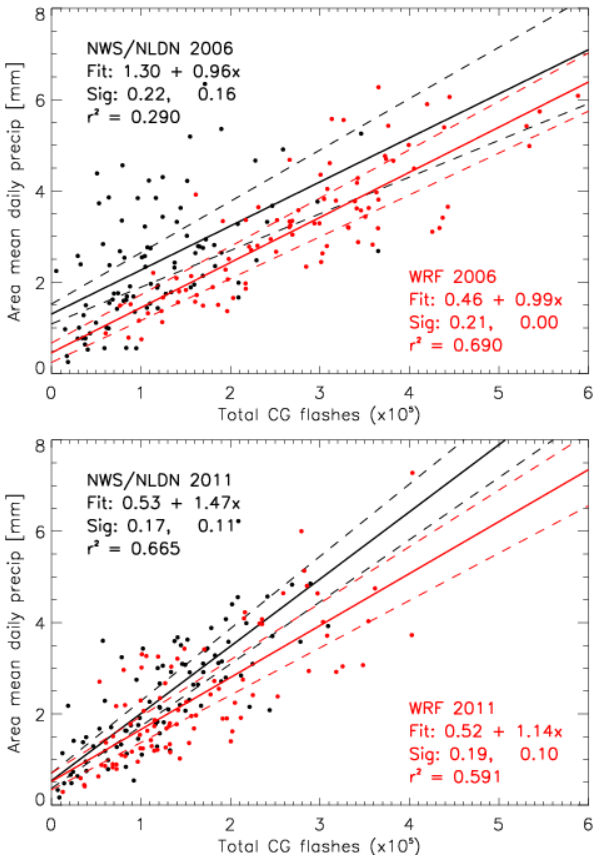

Figure 2.6: **CG flashes vs. precipitation** — Total CG flashes (#) versus area-mean daily precipitation (mm) within the analysis domain (Fig. 2.1). Solid line is the least-square linear fit and dashed lines are $\pm 1\sigma$ for both the constant terms and first-order coefficients. WRF is simualted at 36 km.

The over-prediction of CG flash density along the East Coast in 2006 dominates the regional mean and produces significantly high biases compared to 2011. Figure 2.5a and 2.5b show the time series of the total number of ground flashes predicted by WRF and observed by NLDN within the analysis region (Fig. 2.1). The median daily CG bias is 140 % for 2006 and only 13 % for 2011. It should be noted that these values were obtained by sampling all 3 months. Sampling one month would produce varying results. For instance, while JJA 2011 produces an overall median bias of 13 %, July 2011 alone produces about twice as much lightning as observed but is offset by under-predictions in June and August. Because the lightning detection efficiency of NLDN varies spatially, the CG bias can vary over ranges of

116–154 % for 2006 and 1.7–20 % for 2011. The differences between the median biases for the two summers can be attributed largely to the differences in the total precipitation biases, as illustrated in the previous section (Sect. 2.2.1), for which 2006 is 37 % too high while 2011 is only 5 % higher than observations.

To take into account the bias in the simulated convective strength, area-averaged daily precipitation is correlated with total CG flash count. While the relation is likely nonlinear, the area averages over the analysis domain are roughly linear in both WRF-simulated and observed data (Fig. 2.6). The slopes for the 2006 data are statistically the same, there is a constant positive bias for model produced flash counts over observed values. In contrast, 2011 results are close for small values but modeled and observed values diverge for more intense events. Such inconsistency between years demonstrates the potential for strong inter-annual variability in the correlation between flash rate and precipitation.

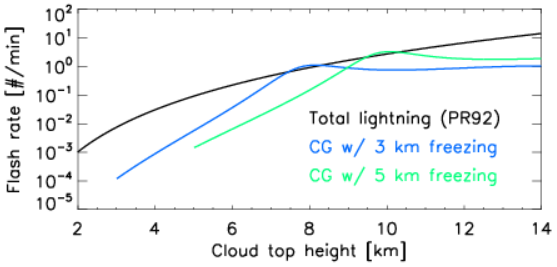

Figure 2.7: **PR92-predicted total lightning as a function of cloud-top** — Total lightning and CG flash rates computed using PR92 and PR93 for various cloud-top heights and freezing levels, demonstrating the source of spectral cut-off in Fig. 2.6.

Figure 2.5c and d show the frequency distributions of the hourly grid flash density. From the spectra, it is apparent that the over-prediction observed in the time series occurs between flash densities of 0.003 to 0.1 $\mathsf{CG\,flashes\,km^{-2}\,h^{-1}}$. However, the abrupt cutoff beyond $\sim$ 0.11 in both 2006 and 2011 modeled distribution indicates that PR92 fails to replicate the observed distribution. The occurrence of this cutoff can be explained by the local maximum when combining the PR92 total flash rate parameterization and PR93 IC : CG ratio parameterization (Fig. 2.7). Together, the predicted CG flash rate is capped at a certain limit, depending on the freezing level regardless of the cloud-top height. In addition, the total flash rate is also under-predicted for high flash rate events (dotted red lines in the figures), thus contributing to the truncated model frequency distribution.

An initial comparison of the model results against the Lightning Imaging Sensor (LIS) total flash data also shows a high bias ($\sim 2.3\times$) in overall flash count but an underestimation of the high flash count events, similar to the results demonstrated by the NLDN comparison. However, comparisons against the LIS data for this study have a low confidence level because of the relatively short time period simulated and the many uncertainties, such as variable detection efficiency and shifting diurnal sampling bias of LIS data, associated with the analysis.

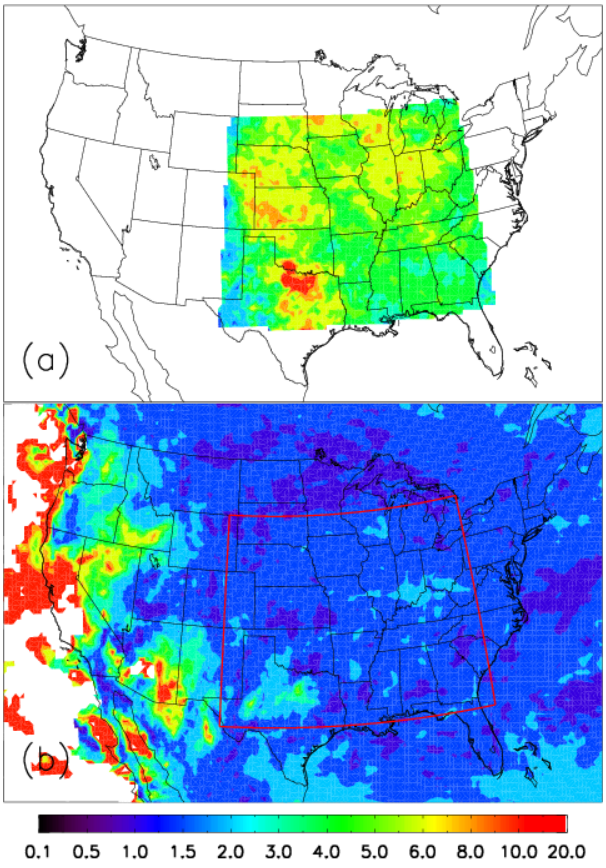

Figure 2.8: **ENTLN and predicted IC:CG bulk ratios** — IC : CG bulk ratios for JJA 2011 as **(a)** observed by ENTLN and **(b)** predicted by WRF at 36 km grid spacing using PR93. The ENTLN detection efficiency used here is 0.65 for IC and 0.95 for CG.

2.2.3 IC : CG ratio

The JJA 2011 IC : CG bulk ratios ($\equiv \sum_t \mathrm{IC}(\boldsymbol{x},t)/\sum_t \mathrm{CG}(\boldsymbol{x},t)$) are calculated within the analysis domain (Fig. 2.8a) using constant detection efficiencies of 95 % and 65 % for CG and IC flashes, respectively. While WRF produced a median IC : CG ratio of 1.74 within the region, ENTLN observed a median of 5.24 with a possible range of 3.80 to 7.17 due to the spatial variability in both IC and CG DEs. Considering the ambiguity in the choice of cloud-top definition described in Sect. 2.1.2, a possible solution to increase the IC : CG ratio computed using Eq. (2.5), thus achieving better comparison against observations, is by eliminating the cloud-top height reduction, an option that maintains the conceptual interpretation of the parameterization but has the potential of offsetting the bias. For consistency, the cloud-top height used in the total lightning parameterization needs to be un-adjusted as well.

To learn whether reasonable lightning flash rates and IC : CG ratios can be estimated by using just the level of neutral buoyancy (LNB), an offline calculation is made of the daily flash counts with the cloud-top height adjustment eliminated. The offline calculation is performed using instantaneous, hourly model output of LNBs and temperatures (for determining freezing levels). While the offline calculation is able to replicate almost precisely the online flash count prediction, which causes both time series to appear overlapping in Fig. 2.9, the CG flash rate frequency distribution is severely degraded because of vertical discretization of cloud tops to model levels and lowered temporal resolution to hourly outputs. When LNB is used for the cloud-top height (with no adjustment), the prediction of both CG and total lightning flash rates increase, as expected. The CG median bias over ENTLN increases from 44 – 51 % to 158 – 172 %, and the total lightning median negative bias of 53 – 25 % becomes a positive bias of 23 – 95 % for the aforementioned range of DEs. Furthermore, even though the frequency distribution of total lightning is closer to the observed distribution, the CG distribution still experiences the truncation as described in Sect. 2.2.2.

2.3 Resolution dependency

A goal of this study is to evaluate the applicability of the PR92 parameterization to resolutions between fully parameterized and partially resolved convection. Thus, it is useful to evaluate how the parameterization behaves as the grid size changes. To test the behavior of the PR94 calibration factor, a 12 km simulation for July 2011 is used. As grid sizes are reduced to allow convective parameterization to be turned off, the transition to $w_{\max}$ based formulation of PR92 (Eq. 2.2) is tested with a 4 km simulation between 25 July–7 August 2006. The domains for these simulations are shown in Fig. 2.1. Together, the results from these simulations will provide insights and recommendations on how to achieve resolution-awareness or independence while using PR92.

2.3.1 Sensitivity to grid size

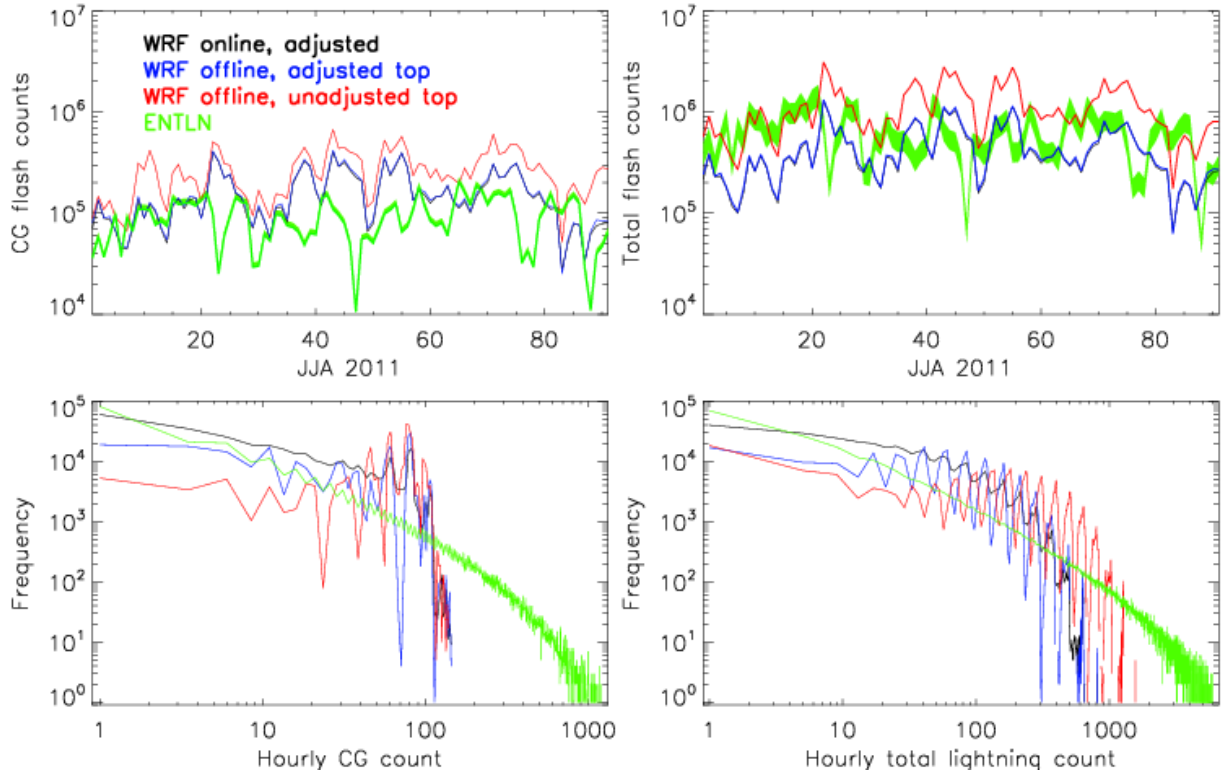

Figure 2.9: **ENTLN and predicted total lightning** — Comparison of WRF predicted lightning flash counts generated online and offline with and without $-2\,\mathrm{km}$ cloud-top height adjustments against ENTLN CG and total flash counts. Thicknesses of the ENTLN bands in the time series are computed using the minimum and maximum theoretical IC and CG detection efficiencies within the analysis domain. Noisiness of offline calculated distributions are associated with using hourly outputs only rather than accumulating flashes at every model time step. It should be noted that online (black) and offline (blue) WRF outputs with adjusted top appear coincident in the time series, but are evidently different from the frequency distribution.

At 12 km, the resolution dependency factor or "calibration factor" (c) from *Price and Rind* (1994) is negligibly smaller (0.56 %) than that applied to 36 km. However, comparison against the 36 km simulation and observations shows that there is a factor of $\sim$ 10 high bias. While there are differences in the statistics of convective strengths between the two simulations, as quantified by precipitation in Sect. 2.2.1, they are too minor to fully reconcile the large bias at 12 km. Therefore, an areal ratio scaling factor ($1/9 = 12^2/36^2$) is applied offline to partially reconcile the differences on top of $c(\sim 1)$, which was applied online.

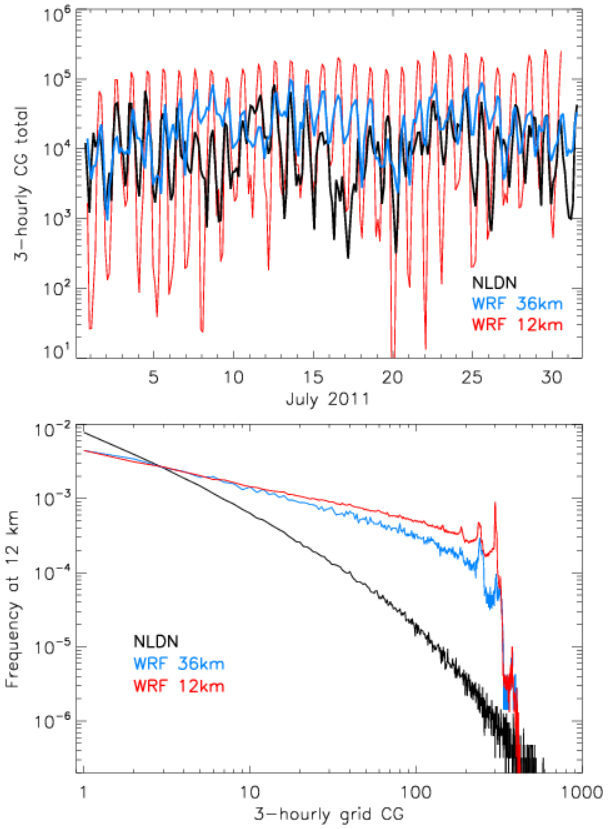

Figure 2.10: **Resolution-dependency of lightning prediction** — Time series and frequency distributions of 3-hourly CG flash counts compared to NLDN gridded to 12 km. The WRF 36 km distribution is adjusted by $\times 9$ to account for the grid per area difference. The choice of computing the distributions for flash rate per grid as opposed to flash density is to demonstrate the consistency of the spectral drop-off at different resolutions.

There are two reasons why the use of areal scaling instead of PR94 is justified in this study. The first reason pertains to why PR94 failed while it has been shown to work in GCMs. The PR94 calibration factor was derived from area-averaged cloud-top heights for progressively larger grid sizes from the original ISCCP 5 km resolution to $8° \times 10°$. On the contrary, the LNBs from the convective parameterization are expected to change only slightly with grid resolution as long as the environmental parameters such as buoyancy remain similar.

The second reason addresses why the areal ratio is expected to work for regional scales. PR92 produces flash counts in unit of number of flashes per storm; thus, when approaching almost convection-resolving resolutions, where major storm size is comparable to grid size, the appropriate scaling should be done according to the expected number of convective cores per grid. Since

$\Delta x = 36\,\mathsf{km}$ gives a reasonable flash rate compared to observations over 3 months, we assumed one storm per grid at this resolution and scaled the flash counts from $\Delta x = 12\,\mathsf{km}$ as an areal ratio. However, the base case resolution may spatially vary because of the dynamics controlling the minimum-permitted distance between convective cores. At coarse grid sizes, the area covered by the convective storm systems may only be a fraction of the grid cell area. Thus, the area scaling ratio may not be applicable when changing from base-case grid spacing (with approximately one storm per grid) to much coarser grid sizes. A possible solution is to include a cloud fraction estimate as part of the scaling factor between grid sizes.

After scaling by 1/9, WRF at 12 km predicts a median of 40 % more 3-hourly lightning flashes than observed by NLDN (Fig. 2.10). This is to be compared with 36 km, which predicted double the 3-hourly lightning for the same period. Simulating an anomalously strong diurnal cycle in precipitation, the 12 km flash count also shows a much more prevalent diurnal variation, associated with the poor simulation of the diurnal cycle of precipitation as previously noted. Much of the over-prediction is compensated by the negative biases in the nocturnal flash rates in the final statistics. Despite the differences in diurnal skill, the parameterization was able to produce the same drop-off in grid frequency distribution beyond 200 flashes per grid per 3 h, for which the primary cause is discussed in Sect. 2.2.2.

2.3.2 Sensitivity to formulation

Comparing the 36 km simulation to the 4 km simulation provides insight into how the predicted flash density changes between resolutions using $f(z_{\mathsf{top}})$ for parameterized convection and $f(w_{\max})$ for resolved convective systems. This is an important factor to be considered if flash rate predictions are to be included in nested simulations or models permitting non-uniform grid-spacings such as Model for Prediction Across Scales-Atmosphere (MPAS-A; *Skamarock et al.*, 2012).

The area-averaged daily precipitation predicted by the 4 km WRF-Chem simulation is 70 % too high prior to 2 August 2006 and only 7.5 % too high after 2 August. On 2 August, the 4 km WRF simulation was re-initialized (with no clouds) to be consistent with the re-initializations of

the outer domain WRF simulations that drove this 4 km simulation described in *Barth et al.* (2012). The flash rate predicted by the 4 km simulation follows the precipitation trend. A 26 % decrease in flash rate occurs between the period before 2 August and the period afterwards.

While the 36 km simulation over-predicted lightning flash rate for this period (25 July–7 August 2006), the 4 km simulation under-predicted the flash rate, exhibiting a −83 % bias relative to the NLDN flash counts prior to the cold-start and a −95 % bias after (Fig. 2.11). Similar underestimation of the $w_{\max}$ formulation has been noted for both tropical (Hector storm near Darwin, Australia) and US continental storms (*Cummings et al.*, 2013). These results indicate that it is important to evaluate the flash rate parameterizations with observations. It is insufficient to use high resolution model results as "truth" for coarse resolution simulations.

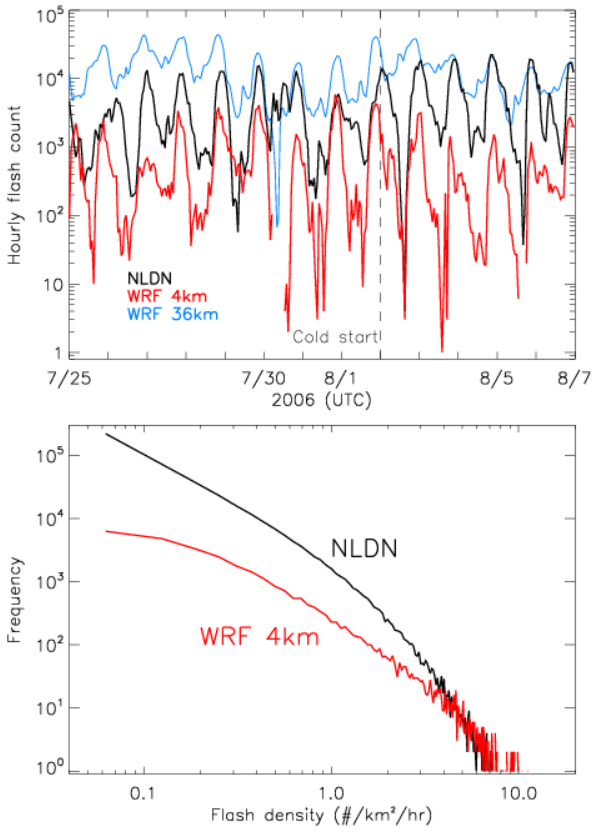

Figure 2.11: **Formulation dependency of lightning prediction** — Time series and frequency distributions of hourly CG flash counts within the analysis domain as observed by NLDN and simulated by WRF at 4 km grid spacing.

Despite the low bias in flash rate prediction, the 4 km WRF-Chem simulation matches the observed distribution of flashes for high flash rate events and placed the burden of underestimation on the low-end of the distribution, which causes the distribution to appear flatter than observed. Since we are using a constant IC : CG ratio based on *Boccippio et al.* (2001) climatology instead of the PR93 parameterization, the erroneous drop-off in the CG flash rate distribution found in the other cases using PR93 is not

present. Such improvement in spectral characteristics suggests that constant climatological IC : CG ratios may be a reasonable if not superior alternative to PR93.

2.4 Conclusions

We have implemented the WRF-Chem model parameterizations for lightning flash rate using prescribed IC : CG ratios and the associated resolution dependency by *Price and Rind* (1992, 1993, 1994), which are based on cloud-top height. In our implementation, the cloud-top height is estimated by the level of neutral buoyancy (LNB), adjusted by $-2\,\mathsf{km}$ to reconcile the difference between LNB and radar reflectivity cloud top. No additional tunings and changes to the parameterizations are done. The modeled precipitation and lightning flash rate are evaluated for the simulations with $36\,\mathsf{km}$, $12\,\mathsf{km}$, and $4\,\mathsf{km}$ grid spacings over CONUS for JJA 2006 and 2011.

The first result is that, after a $2\,\mathsf{km}$ reduction, the use of LNB as a proxy for cloud-top simulated at $36\,\mathsf{km}$ grid spacing produces CG flash rates at the same order of magnitude as NLDN observations. For models using other convective parameterizations, alternative choices of cloud-top proxies may be available and thus the appropriate methods of cloud-top adjustment should be determined on a case-by-case basis. Taking into account model biases in convection, as quantified by precipitation, the precipitation–lightning relation from the model and observations are statistically indistinguishable. While there is up to a factor of 2.4 median bias in the flash counts from the 2006 $36\,\mathsf{km}$ simulation, it is accompanied by a 37 % over-prediction in precipitation. In contrast, the 2011 $36\,\mathsf{km}$ simulation has a precipitation bias of 5 %, which leads to a 13 % over-prediction in flash counts. For the $12\,\mathsf{km}$ simulation the lightning flash rate bias is linked to the anomalously strong diurnal cycle simulated for convection, indicated by precipitation. Such bias in the simulated convection may be caused by a number of other model components.

Second, despite the correct CG count, it is shown that PR92 is incapable of producing the correct frequency distribution for CG flashes, which are truncated at a much lower flash density than observed. The most likely cause is the function form of combining the PR92 total flash rate parameterization and the PR93 IC : CG ratio parameterization, which produces an upper-limit in

the permitted maximum CG flash rate. This brings into question the validity of PR93 in contexts where spectra characteristics are a concern. It is recommended that using constant bulk ratios such as the climatology presented in *Boccippio et al.* (2001) or one derived from total lightning measurements may produce equal, if not better, spectra. Considering that the observed JJA 2011 IC : CG ratio also displays significant departure from the *Boccippio et al.* (2001) climatology for certain areas, it would be useful to revisit the subject of IC : CG climatology in future studies, taking advantage of the advances in continuous wide-area lightning detections over the past two decades.

Third, due to the use of LNB from the convective parameterization instead of area-averaged cloud-top heights, using the PR94 factor to adjust for different horizontal resolutions is not applicable and an areal ratio factor should be used instead to reconcile the resolution dependencies. Since the 36 km base cases produced relatively satisfying results, the 12 km simulation is scaled with an areal ratio relative to 36 km. However, it may be argued that the outcome from the 36 km simulations is only a corollary of the probability of having exactly one convective core within a single model grid. Therefore, other choices of "base case" grid spacings near 36 km may also produce similar results for CONUS, specifically within the analysis domain (Fig. 2.1), and other areas with different storm density may require a different base-case resolution for scaling. On the other hand, area ratios may not be appropriate at coarser resolution as convective core number density is highly non-uniform.

Finally, at 4 km, we used a theoretically similar formulation of PR92 based on $w_{\max}$ within convective cores identified as regions with 20 dBZ or greater radar reflectivity. While the parameterization includes the high flash rate storms, thereby giving a frequency distribution shaped similar to that observed without the erroneous drop-off, the flash count is under-predicted by up to a factor of 10. From this experiment, we see the need to evaluate flash rate parameterizations with observations for the locations and periods specific to the simulations. It is insufficient to use high resolution model results as "truth" for coarse resolution simulations. Hence, validation and tuning prior to further usage of $f(w_{\max})$ from Eq. (2.2) is encouraged. Furthermore, parameterizing flash

rate in cloud-resolving models based on other storm parameters (*Barthe et al.*, 2010) should also be tested.

To summarize, we recommend the following when applying the Prince and Rind parameterizations for lightning flash rates:

(1) Proper adjustment to cloud top should be made to match the expected 20 dBZ radar reflectivity top when applying PR92;

(2) PR93 for IC : CG partitioning should be used only if it is unnecessary to get information on the frequency distribution of flashes;

(3) Scaling for resolution dependency may be performed by areal ratio against a base-case resolution, defined as that producing 1 storm per grid within the domain of interest (36 km grid spacing in this study).

To further the confidence of the lightning flash rate parameterizations and IC : CG partitioning, long-term wide-area total lightning detection and data archiving should be accompanied by coincident observations of cloud-top or other convective properties with well-defined error characteristics in observations and quantifiable predictability in numerical models.

2.5 Comments on cloud-top height reduction

In this study, we used the level of neutral buoyancy (LNB) from the WRF implementation of the Grell–Devenyi convective parameterization (*Grell and Devenyi*, 2002) as a proxy for sub-grid cloud-top heights for the purpose of testing a flash rate parameterization by *Price and Rind* (1992, 1993, 1994). A reduction of 2 km is used to reconcile the differences between LNB and the cloud top that would be obtained if defined at a 20 dBZ reflectivity threshold. While this method produces an integrated flash count consistent with that observed after taking into account model biases in convective precipitation, we acknowledge that storm-to-storm variability cannot be captured by such a simple approach. Presented in this section are offline calculations of both 20 dBZ cloud tops

and LNB cloud tops from a 13-day simulation at 4 km grid spacing to understand the margin of potential errors.

Radar reflectivity is estimated by using rain, snow, and graupel particle information from hourly outputs. For consistency, the offline calculation of reflectivity uses the same modified equations from *Smith et al.* (1975) and criteria as those used in the 4 km simulation. The highest model level with more than 20 dBZ is then defined as the 20 dBZ top.

LNB is estimated by a simple "parcel method," rather than emulating the full algorithm in the parameterization as implemented in WRF. Therefore, the result may differ from what would be produced within the model. First, the dew point depression at the surface model level is determined, which is then used to seek the lifting condensation level (LCL) assuming adiabatic ascent. From the LCL, the moist adiabatic lapse rate (Γ_m) is calculated and the level of free convection (LFC) is determined by linearly extrapolating the moist adiabat using the lower level's Γ_m to the model level immediately above. From the LFC, a search is performed at incremental model levels until the LNB is exceeded. Grid points with LFCs < 500 m or above-freezing temperature at LNBs are discarded.

In total, 1.34×10^6 columns with sufficient reflectivity and cloud-top heights greater than 5 km AGL are found. The distribution of the difference $\langle h_\mathrm{LNB} - h_\mathrm{dBZ} \rangle$ indicates that LNB is higher than the 20 dBZ top 62 % of the time with a mean of 1.1 km and a standard deviation of 2.3 km. Other metrics for defining the required offsets between the two heights can produce different results. For example, to minimize the bias after applying PR92 with $\left| \langle (h_\mathrm{LNB} - \delta h)^5 / h_\mathrm{dBZ}^5 \rangle - 1 \right|$, the reduction δh evaluates to 3.27 km. While the 2 km reduction used in this study differs from the two computed here, it is within the calculated range and thus can still be considered a median representation, especially when the uncertainties in the methods used for the offline LNB and radar reflectivity computations are taken into account.

Finally, it is essential to re-emphasize that the choice of cloud-top reduction is specific to the use of the Grell–Devenyi convective parameterization in WRF or other models producing LNB as the best-available proxy for sub-grid cloud-tops. In other models, cloud-top proxies other than

LNB may be present. In those cases, an adjustment specific to those proxies should be used if PR92 is the preferred method for parameterization. An alternative would be to reformulate PR92 to be based on LNB, which lies beyond the scope of this paper and may be attempted in the future as needed.

Chapter 3

2006 North American Monsoon Case Study — Part I

Upper tropospheric ozone (O_3) has significant impacts on the radiative and chemical budgets of the atmosphere (*Kiehl et al.*, 1999). The global tropospheric ozone burden has seen an increase of 71–130 Tg since the preindustrial period, with much of the uncertainties coming from the estimation of preindustrial emission scenarios for anthropogenic, biomass burning, and lightning sources (*Lamarque et al.*, 2005, and references therein). The radiative forcing resulting from this increase depends strongly on the vertical distribution and is the most sensitive near the tropopause (*Lacis et al.*, 1990).

Previous studies have identified upper tropospheric (UT) ozone enhancements, associated with monsoons, above North America (*Li et al.*, 2005; *Cooper et al.*, 2009, and references therein), Asia (*Park et al.*, 2007; *Worden et al.*, 2009), and equatorial Africa (*Bouarar et al.*, 2011) during summers. *Cooper et al.* (2007) calculated an ozone enhancement of 29–52 ppbv between 10–11 km above Huntsville, Alabama. This observed upper tropospheric ozone enhancement has been linked to the North American Monsoon anticyclonic circulation, which traps ozone precursors that subsequently enhance ozone production. *Li et al.* (2005) pointed out the importance of boundary layer ozone precursors to the UT ozone enhancement using a global chemistry transport model. Their model sensitivity simulations showed that the ozone enhancement is mostly of anthropogenic origin, but lightning-generated nitrogen oxides within the anticyclone and $\mathsf{HO_x}$ precursors from formaldehyde, which is produced from biogenic emissions over the southeast US, both contributed to the O_3 production in the UT. *Cooper et al.* (2009) stressed the importance of lightning-generated nitrogen

oxides, suggesting that more than 80% of the upper tropospheric NO_x within the enhancement is due to lightning, and that it is responsible for 25–30 ppbv ozone at 250 hPa. Furthermore, it has been estimated that the ozone enhancement generates a positive radiative forcing of about 0.50 $W\,m^{-2}$ (*Cooper et al.*, 2007; *Choi et al.*, 2009).

These previous studies suggested the convective transport of boundary layer air, especially in the Gulf Coast region (*Li et al.*, 2005), and lightning-generated NO_x from the western US and Mexico are the primary regions contributing to the O_3 enhancement in the UT. Here, we use a regional-scale model depicting chemistry and passive tracer transport to differentiate further the source regions of the O_3 enhancement for the 2006 North American Monsoon.

The control simulation is evaluated with both meteorological and chemical composition data to show the model's ability in representing dynamics and chemistry. Then, the contribution of boundary layer air (BL), stratospheric air (ST), and air from outside the model domain (boundary condition, BC), to the O_3 enhancement is represented. Correlations between ozone and carbon monoxide are investigated to show the chemical regime of the upper tropospheric ozone enhancement region in comparison to the air just outside this region.

3.1 Model Description

The case study simulation is performed using the Weather Research and Forecasting model (*Skamarock et al.*, 2008) with Chemistry (WRF-Chem; *Grell et al.*, 2005) version 3.4.1 over July and August of 2006. The model is configured with a horizontal grid spacing of 36 km on a Lambert conformal projection centered over the contiguous United Status (CONUS) as shown in Figure 3.1. Vertical levels are discretized into 51 levels of variable

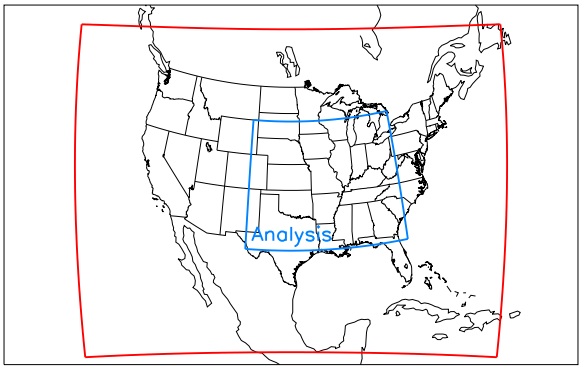

Figure 3.1: **Model domain** — WRF-Chem model domain (red). The marked inner region (blue) is used for the meteorological analysis.

thicknesses (with $<$ 100 m grid spacing near the surface and 600–800 m grid spacing near the troposphere) up to 10 hPa.

The meteorology is initialized and assimilated with data from the National Center for Environmental Prediction (NCEP) Global Forecasting System (GFS) final (FNL) gridded analysis at 6-hr intervals (00, 06, 12, 18 UTC). Nudging is performed for temperature and water vapor above the planetary boundary layer (BL). Nudging for horizontal winds is performed above model level 10 where the pressure is 843 ± 55 hPa. Advection for moisture, chemicals, and passive tracer variables are performed with positive-definite and monotonic limiters (*Skamarock*, 2006; *Wang et al.*, 2009).

To represent sub-grid scale convection, the Grell-3 (G3) convective parameterization, a modified version of the *Grell and Devenyi* (2002) ensemble scheme, is used. The G3 scheme has 144 ($= 3 \times 3 \times 16$) dynamic control and static control/feedback closures with varying parameters. The G3 scheme includes subsidence over neighboring grid cells, but for the 36 km grid size used here, subsidence only occurs within the same column. In addition, shallow convection is enabled to permit ventilation of BL air by weak convection. Cloud microphysics is represented by the *Thompson et al.* (2008b) scheme. Shortwave radiative transfer is represented with the Goddard two-stream method (*Chou et al.*, 1998). Longwave radiative transfer uses the Rapid Radiative Transfer Model (RRTM; *Mlawer et al.*, 1997). The boundary layer (BL) processes are parameterized with the NOAH land surface model (*Chen and Dudhia*, 2001) and the Yonsei University (YSU) scheme (*Hong et al.*, 2006).

The chemical mechanism used in this study is the Regional Acid Deposition Model version 2 (RADM2; *Stockwell et al.*, 1990) compiled with a "WRF-conformed" version of the Kinetic Preprocessor (KPP; *Sandu and Sander*, 2006). No aerosol is included in the simulation. Photolysis rates are calculated using the fast Tropospheric Ultraviolet-Visible (FTUV) scheme (*Tie et al.*, 2003). Chemical initial and boundary conditions are obtained from the Model for OZone and Related chemical Tracers (MOZART-4) global chemistry model (*Emmons et al.*, 2010).

Anthropogenic emissions are prescribed using the 2005 National Emission Inventory (NEI05) from the Environmental Protection Agency (EPA) and is reset everyday at 06 UTC, or 11:00

pm to 2:00 am local time, to allow switching between weekdays (Monday – Friday), Saturday, and Sunday emissions. Biogenic emissions are parameterized using the Model for Emissions of Gases and Aerosols from Nature (MEGAN2; *Guenther et al.*, 2006). MEGAN2 uses a combination of climatological leaf area index (LAI), vegetation speciation, predicted model temperature, and predicted model solar radiation to compute the biogenic VOC emissions consistent with the model meteorological state.

Lightning-generated NO_x emission is parameterized using a modified *Price and Rind* (1992) method based on cloud-top height, which is determined from the G3 convective scheme's level of neutral buoyancy (LNB) adjusted by -2 km (*Wong et al.*, 2013), and scaled down by a factor of 10 to match the observed total flash count estimated from the cloud-to-ground (CG) records of the National Lightning Detection Network (NLDN; *Cummins and Murphy*, 2009) and a crude estimate of the CG-fraction from the *Boccippio et al.* (2001) climatology. The NO emission is set to 350 moles per flash, consistent with *Barth et al.* (2012), and is placed vertically following the *Ott et al.* (2010) distributions.

Three passive tracers are released from the lateral boundary (BC), boundary layer (BL), and the stratosphere (ST). The magnitudes of the tracers are reset to 1.0 at their respective sources for every time step. Note that the sum of the three tracers can be greater than 1.0 because the BL or ST tracers overlap with the lateral boundary (BC) tracer. Further, because the BL and ST tracers are continually being replenished throughout their respective source region, we cannot estimate the percent contribution of each region to a specific grid cell. A lightning NO_x (LNO_x) tracer is also emitted with LNO_x emission. All four tracers have a decaying twin with a lifetime of 24 hours. Each decaying twin is reduced at each time step by q/τ where q denotes the tracer mixing ratio and τ is the loss rate. The effective age of air is then computed as $-\tau \ln \overline{Q}^t / \overline{Q'}^t$, where $\overline{Q}^t$ is the passive tracer value and $\overline{Q'}^t$ is the decaying tracer value integrated over space and time, to allow simple estimates of the time since the tracer has left its source region. These tracers are then allowed to be transported by advection, convective transport, and mixing.

3.2 General results and Model Evaluations

3.2.1 Meteorology

The influence of meteorology on chemistry is important for the formation of the North American Monsoon ozone enhancement (*Li et al.*, 2005; *Cooper et al.*, 2007; *Barth et al.*, 2012). In particular, convection has been shown to detrain boundary layer air, which has relatively low ozone mixing ratios (compared to the upper tropospheric background values) yet is rich in ozone precursors, into the upper troposphere, thus perturbing UT ozone distributions (*Dickerson et al.*, 1987; *Kar et al.*, 2004; *Li et al.*, 2005; *Weinstock et al.*, 2007). Moreover, thunderstorms generate NO_x from lightning, providing the means to accelerate the ozone production in the convective outflow by supplementing to the NO_x-poor BL air. Because of the importance of convection on upper tropospheric ozone, we evaluate the model-predicted precipitation and lightning flash rate with observations.

Precipitation

While precipitation is not a good measurement of the immediate convective strength, the accuracy and availability of information from the National Weather Service (NWS) Advanced Hydrological Prediction Service (AHPS) allows continuous evaluation of the model's prediction. The data product used here is the daily precipitation product from NWS AHPS, a national mosaic product using the combined data from 12 River Forecast Centers (RFCs).

A comparison of the simulated precipitation amount by WRF and the observed precipitation from NWS AHPS during July and August of 2006 is shown in Figure 3.2. WRF is producing a comparable spatial distribution to NWS but with a high bias at the Arkansas/Texas border and a low bias over Tennessee and Kentucky. Another low bias is located in North Carolina east of the Blue Ridge Mountains. The simulated coastal rainfall north of the Gulf of Mexico is also generally lower than observed except for regions near Houston, TX. The simulated bulk convective

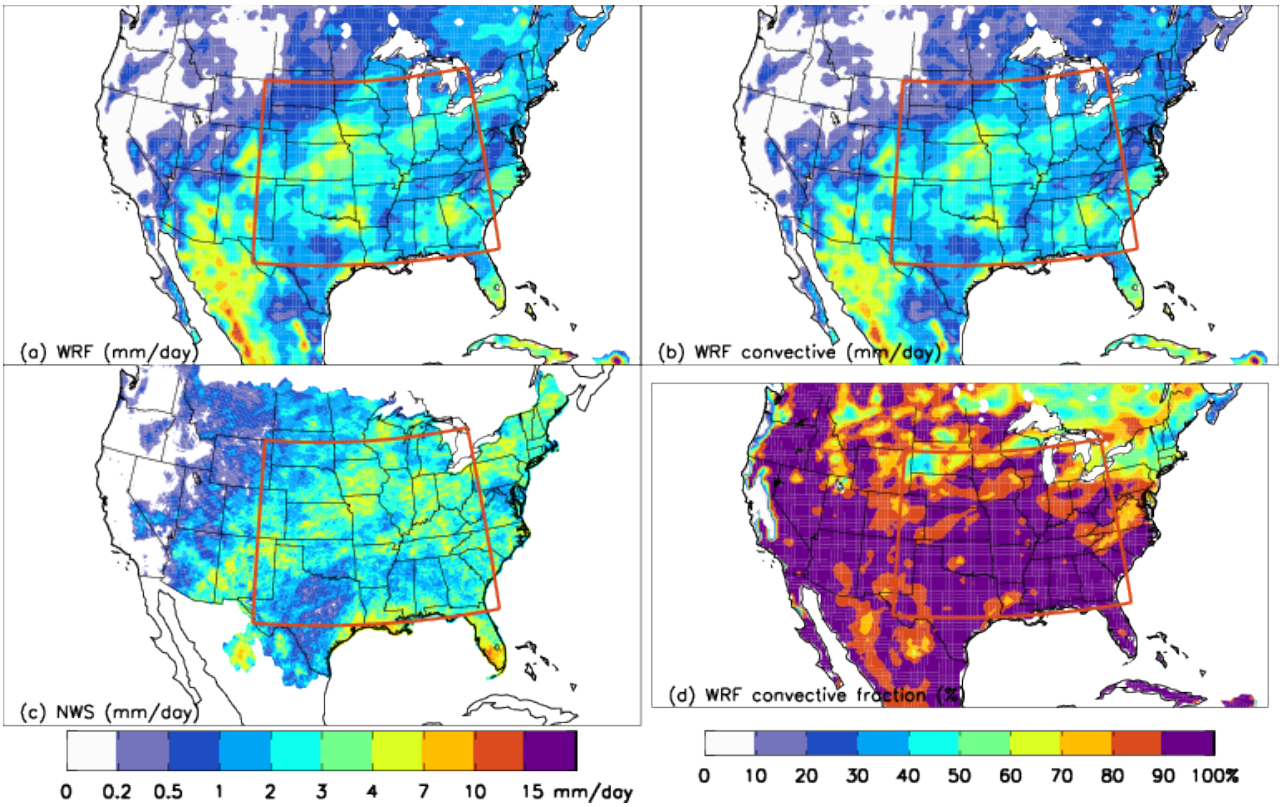

Figure 3.2: (a) WRF-simulated total precipitation, (b) WRF-simulated convective precipitation, and (c) total NWS AHPS precipitation in mm/day. (d) Parameterized fraction (%) of model simulated precipitation.

fraction is relatively high, with more than 90% of the precipitation coming from the convective parameterization over the majority of CONUS.

The WRF-predicted area mean precipitation amount of 71 mm during August for the analysis region shown in Figure 3.1 is 14% less than the 82 mm reported by the NWS (Figure 3.3). This error in precipitation is caused by under-prediction in the frequency of heavy precipitation events above 15 mm/day (Figure 3.3**b**). A possible cause is that weak convective events are over-predicted, thus reducing the availability of moisture and latent heat for heavier events.

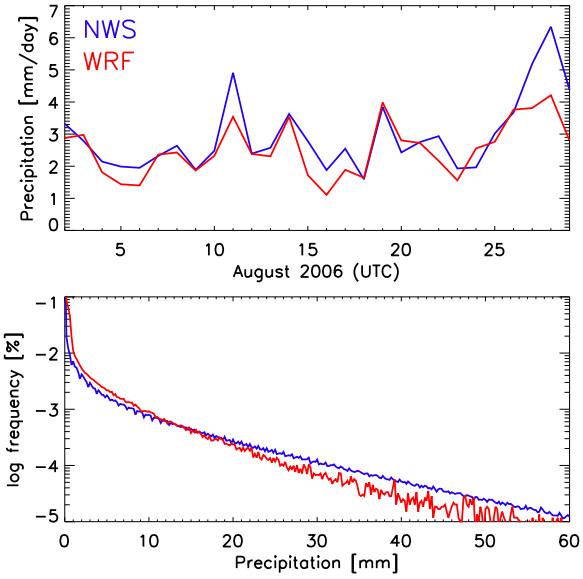

Figure 3.3: **Time series of simulated and observed precipitation** — (a) WRF and NWS daily area mean precipitation within the inner analysis region shown in Figure 3.1 during August 2006. (b) Frequency distribution within the analysis region with bin size 0.2 mm/day.

Lightning

As lightning is tied to NO_x production, an important O_3 precursor, modeled lightning flash rate is also evaluated. We use Vaisala U.S. NLDN data for our evaluation of lightning flash rates. The network provides continuous multiyear CONUS coverage of $> 90\%$ of all CG flashes with ongoing network-wide upgrades since 1984 (*Orville et al.*, 2002, 2010). The frequency range at which the sensors operate allows detection of primarily CG flashes and a small number of IC flashes. Low peak current strokes < 15 kA are eliminated from the data set due to potential misclassification. The median location accuracy is 250 m, which is well within the model grid size used in this study. Multiple strokes are aggregated into a single flash if they are within 1 second and no more than 10 km apart.

Since NLDN reliably detects only CG flashes in 2006 and the current implementation of WRF-Chem produces total flash counts without IC : CG partitioning, flash count outputs from WRF are scaled by 1/4, or an IC : CG ratio of 3-to-1, to account for a crude average of the CG fraction in the southeastern United States according to *Boccippio et al.* (2001). The *Price and Rind* (1992) CG flash count estimation is over-predicting by about an order of magnitude. After scaling the flash rate by 0.1, the predicted flash count, summed over the analysis region for the two months simulated, is 7% higher than that observed by NLDN (Figure 3.4). While the magnitude of the integrated flash count is similar to the NLDN observations, its distribution truncates prematurely at $\sim$ 200 flashes/grid/day (Figure 3.4b) and compensates the deficit with an overestimation of flashes below 100 flashes/grid/day. This early truncation is consistent with the findings discussed by *Wong et al.* (2013).

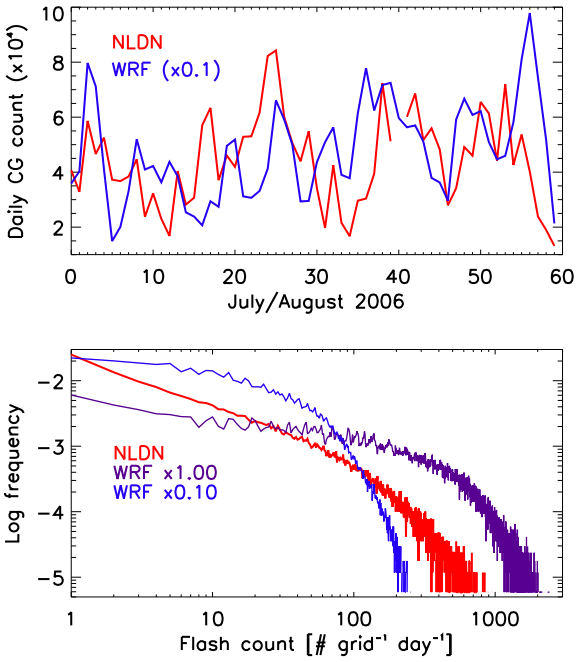

Figure 3.4: **Simulated and observed flash counts** — (a) NLDN CG daily flash count ($\times 10^4$) within the analysis region, with WRF-simulated total flash count $\times 1/4$ to account for CG fraction and $\times 0.1$ to account for systematic bias. (b) Daily grid flash count frequency distributions from NLDN and WRF with different scaling factors.

3.2.2 Ozone

Since the ozone enhancement occurs primarily above the southern United States, it is useful to define a region of focus different from that used in the precipitation evaluation. We define the "anticyclone region" based on the August mean geopotential height ($\overline{Z}_{300}$) at 300 hPa simulated by the model. The anticyclone region is determined by columns with $\overline{Z}_{300} > 9730$ m. While the

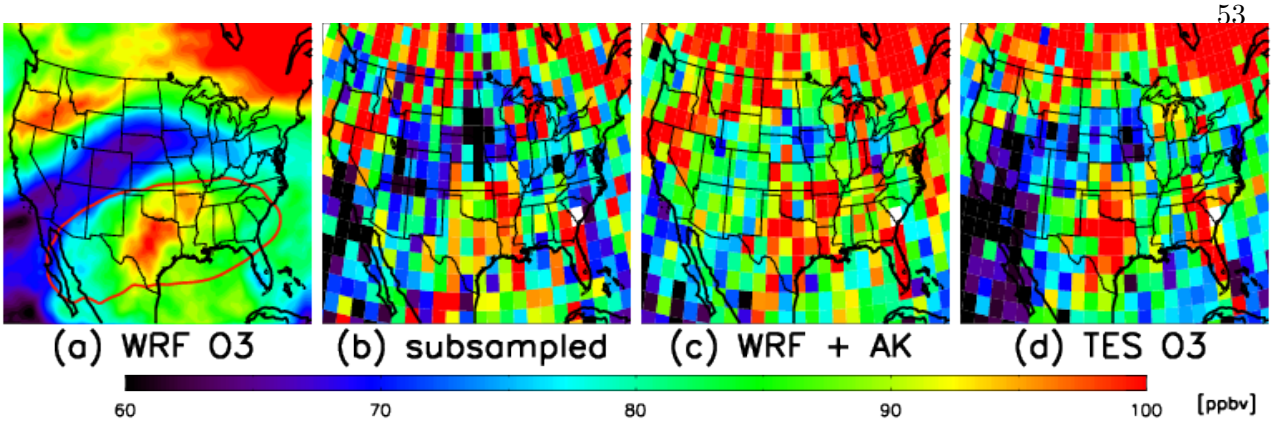

Figure 3.5: (a) Simulated ozone (ppbv) and geopotential height (m) at 300 hPa averaged for August 2006. The 9730 m geopotential height contour indicates the "anticyclone region" used for various analyses. (b) Ozone 3-hourly outputs sampled to all TES transects during August, and gridded to $2° \times 2°$ regular grids. (c) Previous panel with the TES averaging kernel applied. (d) Gridded average of all August TES transects.

anticyclonic circulation is not stationary, using the mean circulation maximizes the duration during which characteristics of the ozone enhancement can be captured.

The August mean 300 hPa ozone and geopotential heights are shown in Figure 3.5a. The location of the ozone enhancement is consistent with that observed and simulated by *Cooper et al.* (2007). The ability to position the enhancement only requires the correct large-scale dynamical features, which are constrained by nudging to NCEP GFS reanalysis. North of the jet stream, persistently high ozone concentration is simulated due to stratospheric ozone. It is found that some of this ozone is occasionally mixed across the jet in the continental outflow region (northeast corner of the model domain) and is then circulated into the anticyclone.

A finger-shaped low-ozone structure of $\sim$ 65 ppbv between the 9650 and 9700 m isohypses over south-central California separates the ozone enhancement core and the northern stratospheric ozone as the result of repeated low-ozone episodes flowing from the subtropical Pacific via the southwest corner boundary condition provided by the MOZART global model prediction. The

occurrence and path of this feature is controlled by the monsoonal circulation and creates the gradient in the monthly mean that partially forms the shape of the ozone enhancement.

Evaluation against TES retrievals

To evaluate the simulated ozone, retrievals from the satellite-borne Tropospheric Emission Spectrometer (TES) are used to provide spatial snapshots along selected transects. TES is a high resolution infrared Fourier-transform spectrometer with a spectral resolution of 0.06 cm^{-1} (*Beer*, 2006). The data products used for the transect-by-transect comparisons below are from version 4 (V004), all of which are special observations in step-and-stare mode with footprints of 5.3 km×8.3 km and 35 km gaps between stares. Through comparisons with ozonesondes, an evaluation with V002 showed that TES ozone had a 3–10 ppbv high bias in the troposphere, but it is still able to pick up the general variability (*Nassar et al.*, 2008). TES products have been used in numerous studies on tropospheric chemistry (e.g. *Hegarty et al.*, 2010; *Voulgarakis et al.*, 2011), convection and water budget (e.g. *Brown et al.*, 2008; *Risi et al.*, 2010), and air quality (e.g. *McMillan et al.*, 2010; *Wang et al.*, 2011).

To compare model O_3 to TES profiles, the model profiles are transformed in the same way as the satellite data. Let $\mathbf{x}_{\mathsf{WRF}}$ be the log of the ozone column vector extracted from WRF-Chem and interpolated onto TES pressure levels, then the averaging kernel is applied as follows:

$$\mathbf{x}_{\mathsf{WRF}}^{\mathsf{TES}} = \mathbf{x_a} + \mathbf{A}\left(\mathbf{x}_{\mathsf{WRF}} - \mathbf{x_a}\right) \tag{3.1}$$

where $\mathbf{x_a}$ is the a priori constraint, $\mathbf{A}$ is the averaging kernel, and $\mathbf{x}_{\mathsf{WRF}}^{\mathsf{TES}}$ is how TES would have observed the WRF-Chem ozone column. Furthermore, columns with potential problems are filtered out using the master quality assurance flag, the C-curve flag to remove retrievals with anomalously high surface ozone (*Zhang et al.*, 2010), and the criteria that $trace(\mathbf{A}) > 4.0$ to ensure sufficient degrees of freedom.

We first compare the ozone mean profile (Figure 3.5) against TES. To do so, WRF-Chem 3-hourly output column vectors are selected for each TES retrieval pixel during August (Figure 3.5b),

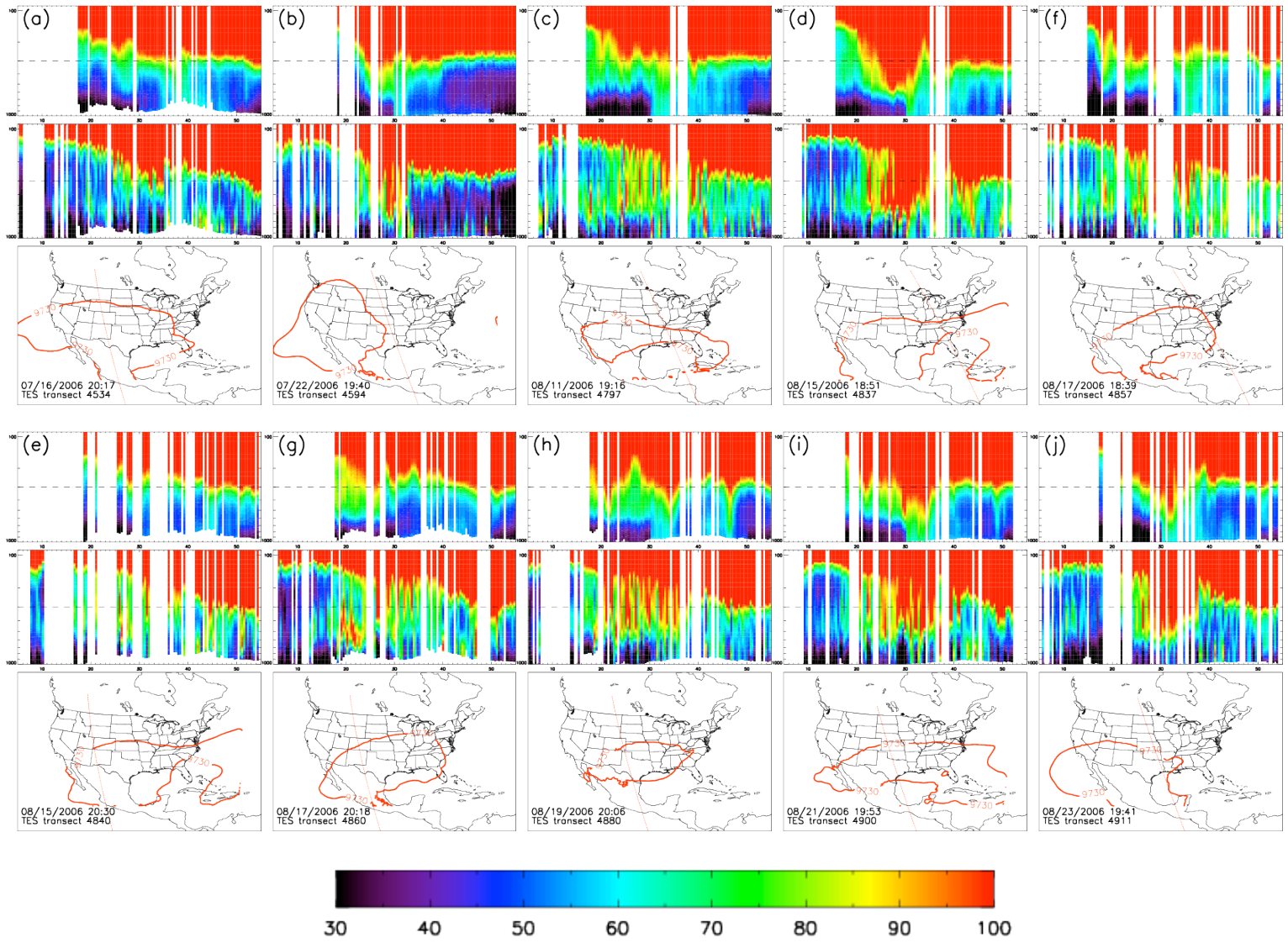

Figure 3.6: First row for each panel is the WRF-Chem ozone profiles in ppbv mapped onto the TES pressure coordinates after applying Eqn. 3.1. Second row is the TES profile. Horizontal dashed line indicates the 300 hPa level. Third row shows the TES transect and the 9730 m geopotential contour at 300 hPa from WRF. Time indicated is the 30°N-crossing time in UTC.

then the averaging kernel is applied (Figure 3.5c). This can be compared to the monthly average TES product at 300 hPa, gridded onto $2^\circ \times 2^\circ$ grids (Figure 3.5d) each of which receives 0–16 pixels for a total of 4699 pixels within the simulation domain. The temporal subsampling of the WRF-Chem output introduce noise that prevents clear identification of the ozone enhancement, although a high bias can still be discerned. Nonetheless, the general spatial distribution is consistent with TES observations.

We next compare the ozone curtain profiles. Between July 15 and August 23, ten TES transects are selected and compared to the WRF-Chem output of the corresponding date at 18 UTC or 21 UTC, whichever is closer to the 30°N-crossing time (Figure 3.6). These transects are selected because they either show signs of upper tropospheric ozone enhancement, or intersect regions with 300 hPa geopotential height greater than 9730 m while passing over the United States.

Figure 3.6 shows the comparisons of model outputs and satellite retrievals along TES transects. Qualitatively, the heights of the 100 ppbv ozone isopleths are well simulated north of 30°N. South of 30°N, upper tropospheric ozone is often over predicted. These over-predictions occur either within Mexico, where the terrain of the Sierra Madre triggers frequent large-scale thunderstorms, or the Gulf of Mexico, where LNO_x marine emission is unconstrained due to lack of observations. For example, transect 4911 (Aug 23, Figure 3.6j) is able to capture the ozone enhancement between 28–47°N, followed by a ridge-like low ozone structure at 40°N attributable to a low-ozone air mass transported from the subtropical Pacific. South of 28°N, where the transect was passing over the Gulf of Mexico, WRF-Chem is

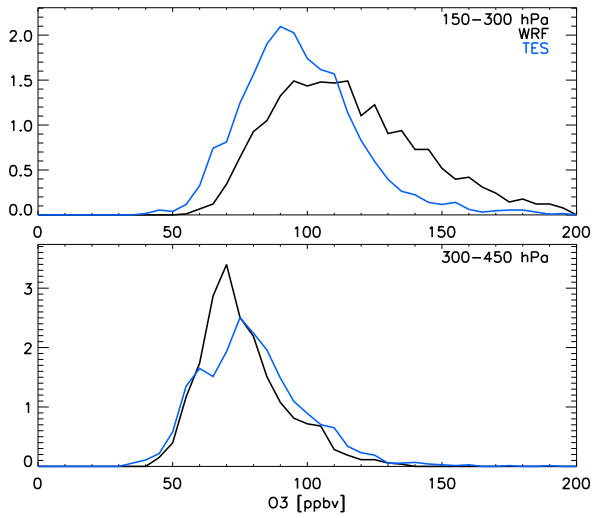

Figure 3.7: **WRF-Chem and TES ozone frequency distributions** — Normalized frequency distributions (%/ppbv) of TES and WRF-Chem ozone mixing ratios between (a) 150–300 hPa and (b) 300–450 hPa between 25–40°N.

biased high with the 100 ppbv ozone isopleth reaching 300 hPa while TES observed only 70–90 ppbv up to 150 hPa. Similar high biases are also seen for transects 4837 (Aug 15, Fig 3.6d) and 4900 (Aug 21, Figure 3.6i).

By compiling frequency distributions of the upper tropospheric and mid-tropospheric ozone during the simulation period, we find that WRF-Chem simulates higher ozone than observed by TES in the upper troposphere (150–300 hPa) between 25–40°N (Figure 3.7). TES observed a mean ozone mixing ratio of 100 ppbv with a standard deviation of 22 ppbv. In contrast, WRF-Chem simulated 120 ± 31 ppbv. The larger standard deviation from WRF-Chem indicates that the predicted upper tropospheric ozone is less well-mixed than observations suggest. The mid-troposphere (300–450 hPa) frequency distributions are much more similar in both mean and width, with 78 ± 17 ppbv and 82 ± 19 ppbv for WRF-Chem and TES, respectively.

The comparison against TES retrievals shows that while ozone is overestimated in the upper troposphere, the existence of the ozone enhancement and its location are well-simulated. Some drawbacks of using TES are the results' dependencies on a priori constraints and sparse temporal resolution.

Evaluation against IONS-06

To complement the evaluation against TES, we use ozonesonde profiles taken during the INTEX-B Ozonesonde Network Study of 2006 (IONS-06; *Thompson et al.*, 2008a). During this campaign, 410 ozonesondes were launched from 14 sites strategically positioned to represent major sources, sinks, and pathways of tropospheric ozone in North America. These sondes used electrochemical concentration cell (ECC) sensors that have precisions within ±(5–10)% in the troposphere (*Smit et al.*, 2007). Between different models of the instruments, measurement biases due to variation in potassium iodide sensing concentration may be on the order of 2–3% (*Smit et al.*, 2007). Data from this campaign and its predecessor, IONS-04, have been used to support studies on continental tropospheric ozone distributions (e.g. *Cooper et al.*, 2007), inferring local ozone sources

(e.g. *Thompson et al.*, 2008a), and evaluations of air quality models (e.g. *Tarasick et al.*, 2007) and satellite retrievals (e.g. *Nassar et al.*, 2008).

Ozonesondes launched during August 2006 within the model domain are compared to WRF-Chem ozone vertical profiles. As an example, comparison at Huntsville, Alabama is shown in Figure 3.8. Despite the prevalent over-prediction of ozone concentration in the upper troposphere, the timing of the occurrences of upper tropospheric ozone enhancement episodes corresponds well with ozonesonde measurements. Specifically, termination of the first enhancement on August 11 followed by a drop in ozone throughout the entire column is seen in both WRF-Chem results and the ozonesonde profiles. Similarly, the onset and termination of the second enhancement on August 23/24 is also simulated. These events are likely caused by the synoptic movements of the enhancement controlled by dynamical features. Over all North American sites within the model domain, we find that the simulated ozone mixing ratios above 200 hPa is a factor of 2–3 higher because convective detrainment is occurring at these high altitudes, which will be discussed in more details in the the next chapter.

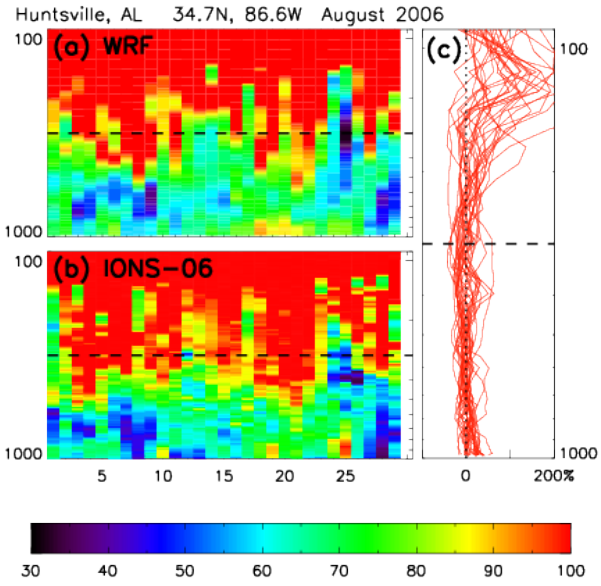

Figure 3.8: **Comparison against Huntsville ozonesonde** — WRF-Chem ozone vertical profiles in ppbv during August IONS-06 ozonesonde launches at Huntsville, Alabama and the relative bias against the measured ozone mixing ratios. Horizontal dashed lines indicate the 300 hPa levels in each panel.

In conclusion, WRF-Chem is able to simulate an upper tropospheric ozone enhancement that coincides with the "anticyclone region," but the ozone mixing ratios are overestimated primarily in the upper troposphere. Despite the high bias, spatiotemporal variabilities controlled by large-scale dynamics are observed at individual locations affected by the ozone enhancement.

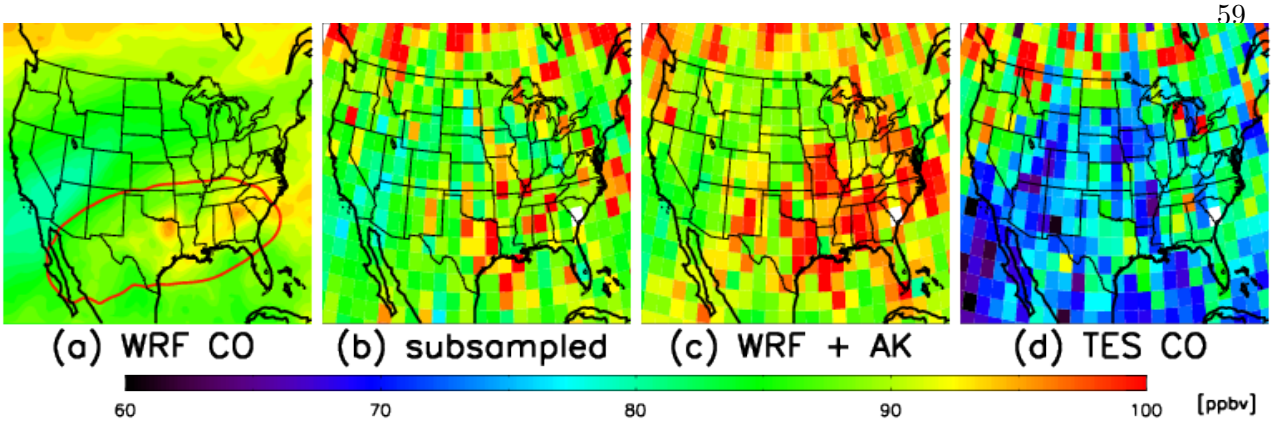

Figure 3.9: Same as Figure 3.5, except for carbon monoxide.

3.2.3 Carbon Monoxide

To understand the ozone bias, it is useful to examine its chemical precursors. Carbon monoxide (CO) is widely used for tracking boundary layer air and pollutants (e.g. *Pan et al.*, 2007; *Weinstock et al.*, 2007). Emitted through incomplete combustion, CO is an excellent indicator for anthropogenic emission sources and biomass burning. It is also produced chemically through OH oxidation of a wide range of VOCs. Furthermore, its 2–3 month lifetime in the troposphere allows CO to be an effective tracer for long-range transport.

Figure 3.9a shows the August mean CO mixing ratio at 300 hPa. At the center of the anticyclone circulation is a distinct CO maximum over northeastern Texas. This feature may be the result of a combination of CO accumulating via the NAM circulation and local convective detrainment of boundary layer air. Considering the Texas/Arkansas region shows a high bias in convective precipitation (Sect. 3.2.1), this feature should be weaker than shown. On the other hand, the high CO simulated over Georgia and neighboring states may have been underestimated because of the under-prediction in convection along the Blue Ridge Mountains. North of the jet stream, anomalously high CO found near the tropopause is a result of CO being transported from the western domain boundary. This influx of CO can be linked to intercontinental transport of widespread wild fires across the Siberian plateau during July. Between these two regions of high

CO is an air mass with low CO and low ozone transported from the subtropical Pacific into the inner CONUS between the 9600 and 9700 m isohypses.

Evaluation against TES retrievals

To evaluate the predicted CO, we compare WRF-Chem results against TES CO products. The instrument characteristics of TES are already described in Section 3.2.2. The TES CO product has been evaluated against the Measurements of Pollution in the Troposphere (MOPITT) satellite retrievals (*Luo et al.*, 2007a; *Ho et al.*, 2009) and aircraft measurements (*Luo et al.*, 2007b; *Lopez et al.*, 2008). These studies found that TES CO products show slightly lower column CO values compared to MOPITT and a ±10% bias relative to in-situ measurements. The primary contributions to the bias are smoothing errors and the dependency on the a priori constraint used for TES retrieval. Except for instances of poor spatiotemporal coincidences, correlation coefficients between in-situ measurements and TES retrievals are between 0.61 and 0.92. Therefore, while retrieval values may be biased, the relative variabilities of CO are expected to be realistic.

The TES CO product is often utilized in tandem with the TES ozone product. *Logan et al.* (2008) used these two products to investigate the impact of El Niño on tropospheric composition. Similarly, *Voulgarakis et al.* (2011) used them to investigate the global O_3-CO correlation. We compare WRF-Chem CO to the TES CO product using the procedure outlined in Equation 3.1, similar to the comparison done with ozone in the previous section except for a minimum degrees of freedom of 0.8 and without the C-curve flag. Similar to ozone, the August model output has been subsampled and transformed in Figure 3.9 to compare with the gridded TES monthly average. The predicted mixing ratio value is seen substantially overestimated although the spatial variability is represented well.

Figure 3.10 shows the WRF-Chem CO mapped onto the TES transects along with TES CO products. Again, WRF-Chem is biased high in the mid-to-upper troposphere. There are three possible causes for a high bias in CO. The first being an underestimation of the CO loss rate, governed by dry deposition and chemical losses via CO + OH, which may be subsequently

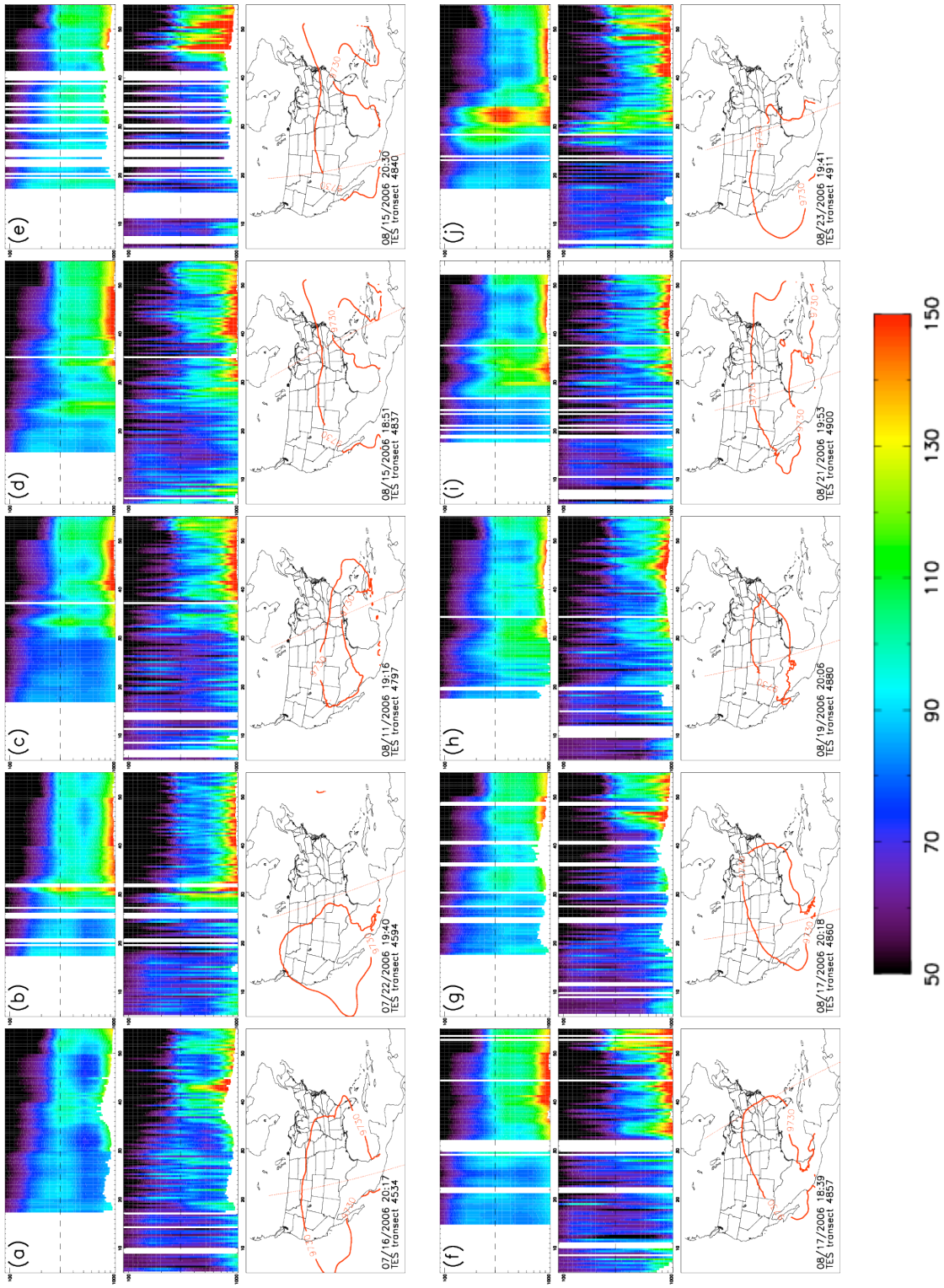

Figure 3.10: Same as Figure 3.6, except for carbon monoxide.

attributed to photolysis as OH is primarily controlled by the photolysis rate $J(O_3)$ to form $O(^1D)$. The second possible cause is an overestimation of boundary layer air detrainment. Even though precipitation has been under-predicted overall (Sect. 3.2.1), there is substantial over-prediction in the frequencies of light precipitation events < 15 mm/day (Figure 3.3b). Finally, the high bias may be due to the application of the TES averaging kernel and a priori constraint. Though not utilized within the interior of the WRF-Chem simulation, the MOZART model output also shows a high bias when compared to TES (Figure 3.11).

While there is a high bias in the upper troposphere connected to convective transport or loss rate, there is a low bias at northern latitudes within the lower-to-mid troposphere. A source for these low biases is that the current simulation did not prescribe biomass burning emission via wildfire events. Using the fire products from the Moderate Resolution Imaging Spectroradiometer (MODIS; *Justice et al.*, 2002), several enhanced CO plumes in the TES transects can be identified as fire related. On July 16, transect 4534 (Figure 3.10a) captured a wildfire at Soda Creek, WY (43.5°N, 110.2°W). On August 15 and 17, multiple transects (Figure 3.10e–g) captured the downwind plumes of widespread fires from Oregon as heightened CO signature between 46–53°N. Finally, transect 4911 captured the plume from the Idaho fires on August 23 (Figure 3.10j). Excluding wildfire events, WRF-Chem is almost always biased high.

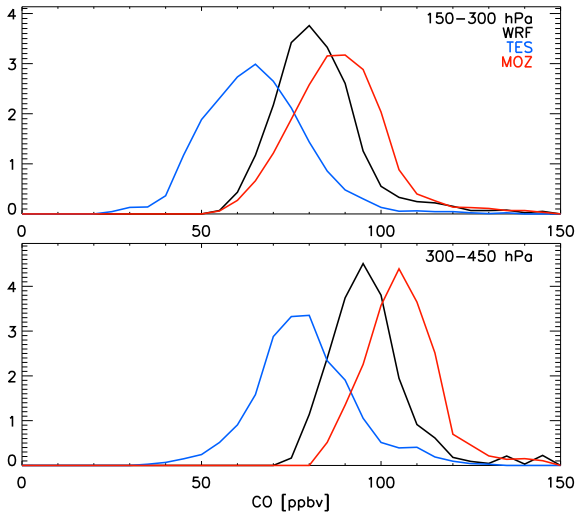

Figure 3.11: **WRF-Chem and TES CO frequency distributions** — Same as Figure 3.7, except for carbon monoxide and TES-adjusted MOZART distributions are also provided for reference.

The CO frequency distributions from the WRF-Chem results and TES CO retrievals for data between 25–40° are shown in Figure 3.11. The computed mean values for the upper tropospheric distributions are 85 ppbv and 68 ppbv for WRF-Chem and TES respectively, and thus WRF-Chem

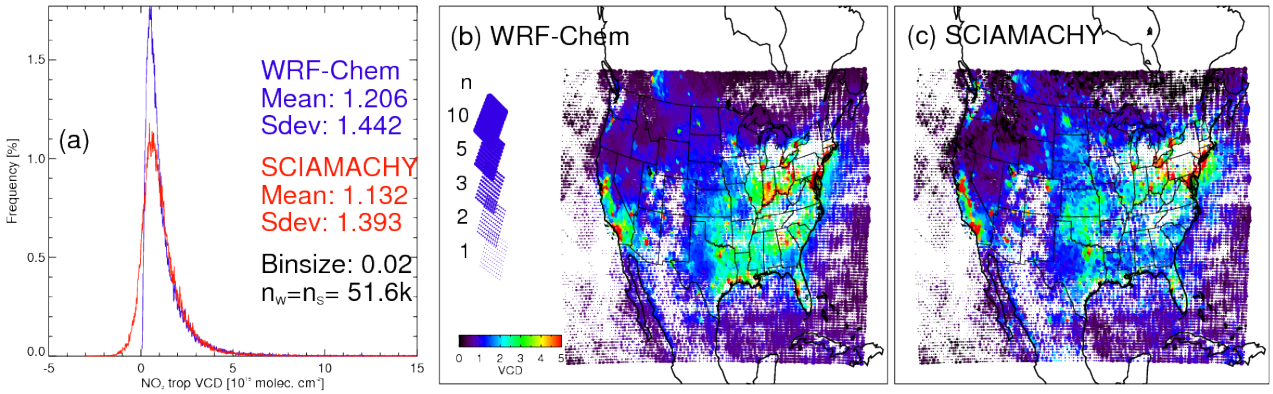

Figure 3.12: (a) Frequency distributions of WRF-Chem and SCIAMACHY NO_2 tropospheric VCDs in 10^{15} molec cm^{-2} during July and August 2006. (b) Mean WRF-Chem tropospheric VCDs in 10^{15} molec cm^{-2} with pixel density indicating the number of samples used (up to $n = 15$ but saturates at 10) at each grid point. (c) Same as c, but for SCIAMACHY.

is 26% too high. In the mid-troposphere, the mean mixing ratios are 100 ppbv and 81 ppbv, thus WRF-Chem is 22% higher.

3.2.4 Nitrogen Oxides

To evaluate the model's output of NO_x, we compare tropospheric NO_2 vertical column densities (VCDs) to retrievals from the Scanning Imaging Absorption Spectrometer for Atmospheric Chartography (SCIAMACHY) instrument on board of the Environmental Satellite (ENVISAT) (*Burrows et al.*, 1995; *Bovensmann et al.*, 1999). The instrument measures scattered and reflected sunlight in the thermal IR spectral range, providing sensitivity to trace gases in the troposphere such as NO_2 and formaldehyde (HCHO). The retrieval used in this study is developed at the Royal Netherlands Meteorological Institute (KNMI) and obtained via the Tropospheric Emission Monitoring Internet Service (TEMIS) project (http://www.temis.nl). The retrieval algorithm uses the Differential Optical Absorption Spectroscopy (DOAS) method and a data-assimilation technique, which utilizes a chemistry-transport model (CTM) with ECMWF operational analyses meteorology to estimate the stratospheric portion of the retrieved column (*Boersma et al.*, 2004). Evaluation of the TEMIS NO_2 product has been performed by *Lambert et al.* (2004) against NDSC data, showing

bias up to 3.5×10^{15} molec cm^{-2}. The differences between retrievals have been attributed mostly to the tropospheric air mass factor (*van der A et al.*, 2010), which has a sensitivity to cloud fractions of up to 20% (*Boersma et al.*, 2004).

For the comparison, each SCIAMACHY tropospheric VCD data point is associated with a single WRF-Chem column determined by rounding the time of measurement to the nearest model output time (3-hourly). Due to ENVISAT's orbit, all measurements are taken between 15–21 UTC. Matched WRF-Chem NO_2 tropospheric columns are then accumulated using the tropospheric VCD averaging kernel for levels below the tropopause index computed using the WMO tropopause definition and provided with the satellite product. Over 61 days, 5.2×10^5 pixels were selected. An individual model grid receives anywhere between 0 to 15 pixels, which is less than 20 pixels (≈61 days/3 days per global survey) due to rejected measurements.

Using this procedure, the frequency distributions of WRF-Chem and SCIAMACHY NO_2 tropospheric VCDs are calculated (Figure 3.12a). While the WRF-Chem distribution is lognormal with a background close to 0.1×10^{15} molec cm^{-2}, the SCIAMACHY distribution is closer to a normal distribution skewing towards the left with a negative tail. Negative values in tropospheric column retrievals are permitted because of the retrieval process, which involves estimating and subtracting the stratospheric NO_2 partial column. Despite the differences in the distributions, the modes for both distributions are $\sim 0.5 \times 10^{15}$ molec cm^{-2}, consisting mostly of data points from the Pacific marine columns, Idaho/Montana, and Canada. Spatial distributions (Figure 3.12b,c) of most regions are well-simulated with a high bias in regions with high flash rates of $\sim 2 \times 10^{15}$ molec cm^{-2}, over a background of $0.5–1 \times 10^{15}$ molec cm^{-2}, which is within the potential range of retrieval biases.

3.2.5 Evaluation summary

A case study simulation is performed using WRF-Chem with specific physics and RADM2 chemistry options described in Section 3.1 for the 2006 North American Monsoon. We found that the model produces the following results compared to various in situ or remote sensing observations:

(1) Convective strength, proxied by precipitation, is generally distributed similarly to observations, but with an overall underestimation in integrated rainfall while overestimating at certain locations;

(2) Lightning flash rate is estimated to be within the range of variability of the NLDN CG flash counts when using a scaling factor of 0.1 and an approximated bulk IC : CG ratio of 3 : 1;

(3) Ozone is over-predicted by $\sim$ 20% in the upper troposphere but largely consistent with TES retrievals in the mid-to-upper troposphere in terms of spatiotemporal and frequency distributions;

(4) Carbon monoxide (CO) is over-predicted by $\sim$ 26% compared to TES retrievals in the upper troposphere;

(5) NO_2 VCDs are simulated within the range of retrieval uncertainties.

3.3 Tracer diagnostics

While the ozone enhancement occurs in the upper troposphere largely within the "anticyclone region," as previously defined as the columns with an August mean geopotential height of 9730 m or greater, the air that comprises the enhancement volume originates from various regions and sources. Thus, to connect the composition and air mass sourcing, we examine tracer-tracer correlations and passive tracer diagnostics, as described in Section 3.1.

3.3.1 O_3-CO relation

The relationship between ozone and carbon monoxide has been used to study the tropospheric-stratospheric transition in chemical regimes (e.g. *Pan et al.*, 2007; *Hegglin et al.*, 2009, and references therein). Similarly, such analysis may be applied to tropospheric data alone to identify contributions from various pathways (e.g. *Zhang et al.*, 2006; *Voulgarakis et al.*, 2011; *Cristofanelli et al.*,

2013). In the troposphere, CO has a high volume mixing ratio (VMR) near the surface and low VMR in the upper troposphere because of anthropogenic surface emissions. Ozone, on the other hand, has high values near the tropopause because of transport from the stratosphere. Together, the O_3-CO anti-correlation over a sufficiently expansive column can expect to form an "L"-shaped joint distribution.

Figure 3.13 shows the joint-distributions at three separate pressure ranges computed both inside ($\overline{Z}_{300} > 9730$) and immediately outside ($9710 < \overline{Z}_{300} < 9730$) the anticyclone north of 25°N for August between 15–21 UTC. Both distributions exhibit the expected "L"-shaped structure. The most frequent mixing ratios (modes) are near 55 ppbv CO/70 ppbv O_3 and 55 ppbv CO/50 ppbv O_3 for upper troposphere and mid-troposphere, respectively, for both within and just outside the anticyclone. However, the mode inside the anticyclone is 68 ppbv CO/30 ppbv O_3 while that just outside of the anticyclone is 52 ppbv CO/17 ppbv O_3 for levels below 700 hPa because of the large number of remote data points.

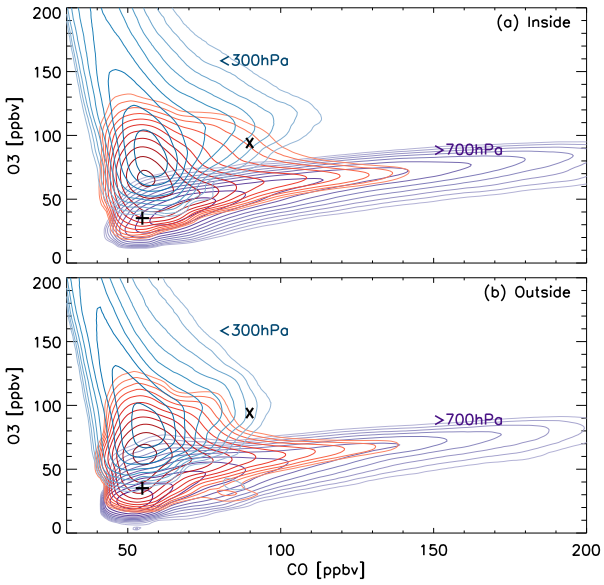

Figure 3.13: O_3-CO joint-distributions (a) inside ($\overline{Z}_{300} > 9730$ m) and (b) outside (9710 m$< \overline{Z}_{300} <$9730 m) the anticyclone region for the upper troposphere (100–300 hPa), lower troposphere (> 700 hPa), and mid-troposphere (300–700 hPa). Contours are calculated in log-scale with 10 levels between 10^{-3} to 10^{-1} % ppbv^{-2}. Features "X" and "+" are used for discussion in Sect. 3.3.

While there are many similarities between inside and just outside the anticyclone seen in the O_3-CO correlation, there are differences. The regime wherein both CO and O_3 are high indicates photochemical production is active. The data points with both high CO and high O_3 (feature "X" in Figure 3.13) are more commonly found within the anticyclone in the upper troposphere and only found within the mid-troposphere within the anticyclone. Thus, chemical production in the mid-to-upper troposphere is indeed enhanced

within the anticyclone region compared to outside the anticyclone. There is also a relatively larger fraction of data points within the mid-troposphere with both low CO and low O_3 outside the anticyclone (feature "+" in Figure 3.13), which is comprised largely of clean air from the Pacific.

3.3.2 Air mass tracers

Air mass passive (non-reactive) tracers can be used to diagnose the contribution of different tropospheric regions to the upper tropospheric anticyclone. Tracers released from the lateral boundaries (BC), the boundary layer (BL), the stratosphere (ST), and with lightning NO_x are shown in Figure 3.14. The impacts of the NAM circulation and its associated anticyclone region are clearly shown in the spatial distribution of the lateral boundary (BC) tracer (Figure 3.14a). Within the anticyclone region ($\overline{Z}_{300}$ >9730 m), the air mass has a grid-temporal-mean of $97.6 \pm 0.3\%$ (σ^2 computed from spatial variance) of BC tracer over August. A strong gradient is simulated as air is unable to mix across the western boundary of the anticyclone, resulting in little to no dilution of the anticyclone air with the clean, low O_3 from the subtropical Pacific.

The lightning NO_x tracer (LT) also shows substantial localized enhancement within the anticyclone (Figure 3.14g). The observed eastward shift from the 9730 m contour can be explained by the overall higher lightning flash rate in the southeastern United States. The maximum accumulated passive LT tracer is 3 ppbv within the anticyclone.

On the other hand, the boundary layer (BL) tracer has only a small correlation with the shape or positioning of the anticyclone. The lack of a distinct region of BL air within the region marked by the average 9730 m geopotential height could be due to the movement of the anticyclone during the month of August. The location of the 9730 m geopotential height on specific days during the month (Figure 3.6 or 3.10) is often offset from the average location (Figure 3.14). Thus, depending on the location of the daily anticyclone, the BL air may be circulated to regions outside the average location of the anticyclone once it is lofted via convection. Furthermore, spatial distribution of convective precipitation (Figure 3.2) is not distributed according to the circulation, thus BL air is detrained across CONUS inside and outside the anticyclone region. The stratospheric (ST) tracer

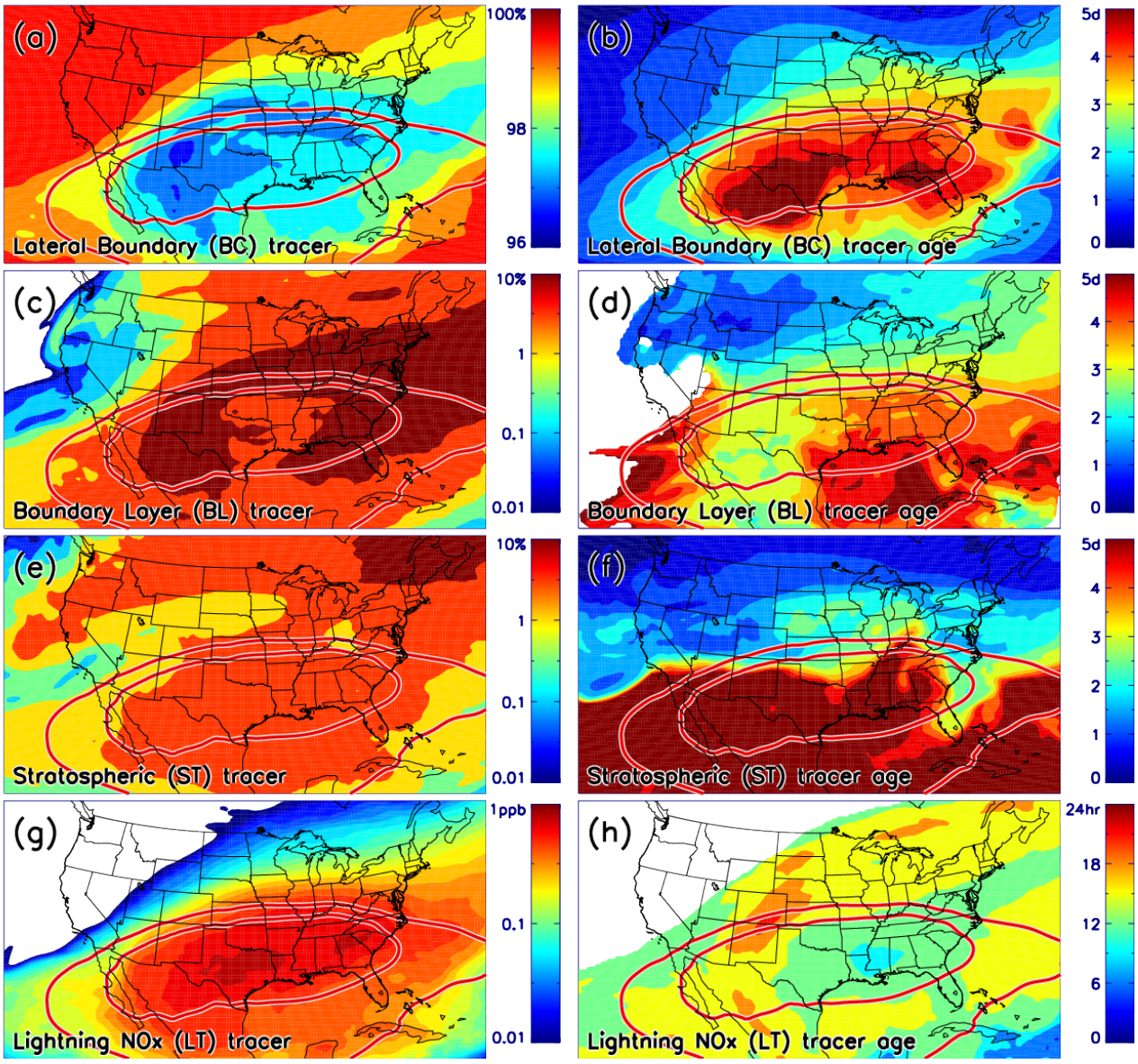

Figure 3.14: Passive tracer values (left column) and ages (right column) at 300 hPa averaged for August. The 9710 m and 9730 m geopotential heights are also shown.

has a similar curvature as the anticyclonic circulation on the western portion of the anticyclone, but does not show a gradient across the eastern boundary of the anticyclone because of the influx of high ozone air associated with mesoscale eddies in the region of strong wind shear near the jet in the continental outflow region along the eastern seaboard (see *Konopka et al.*, 2010).

The "equivalent" age of the tracer can be estimated based on the logarithmic ratio of the passive to decaying tracers (Section 3.1). Due to mixing by processes such as injection of fresh BL air by convective outflow into aged BL air, the age values should not be interpreted literally, but it gives us an idea of the general characteristics of the air mass. Both BC and LT ages show clear distinctions across the anticyclone region boundary. The range of ages for the BC tracer within the anticyclone is 3.9–5.5 days, while the range immediately outside the anticyclone between 9710 m and 9730 m is 2–5 days. LT tracer age ranges from 10.9–21.8 hrs within the anticyclone and 13.1–22.5 hrs just outside. Since the LT distribution is heavily influenced by areas with high lightning flash frequency, young LT tracers are expected and found only within the eastern $\sim 2/3$ of the anticyclone as well as towards the outflow region. Similar to tracer values, neither BL nor ST tracer ages show any differences across the anticyclone region boundary. BL and ST ages inside the anticyclone are 3.8 ± 0.6 days and 5.3 ± 1.1 days respectively, while the ages just outside the anticyclone are 4.1 ± 0.7 days for BL and 5.5 ± 1.4 days for ST tracers.

3.4 Discussion and Summary

Using the Weather Research and Forecasting model with Chemistry (WRF-Chem), we have simulated the upper tropospheric ozone enhancement during the North American Monsoon in 2006 and evaluated its sources of variability using tracer diagnostics computed within the model. Despite overestimation of upper tropospheric ozone and carbon monoxide, evaluated against TES satellite retrievals, we found that the positioning of the mean ozone enhancement is consistent with that found by *Cooper et al.* (2007) and seen in the TES retrievals. Furthermore, with a tuned lightning parameterization, we found that our NO_2 vertical column density is within retrieval bias of the SCIAMACHY product used.

By examining the O_3-CO relation, not only did we find enhanced chemical production within the anticyclone, but heightened presence of air with both low O_3 and low CO immediately outside the anticyclone at the mid-to-upper troposphere levels, indicating the existence of a source for dilution outside the anticyclone. Conversely, clean air from the southwestern model boundary is steered away from the mean circulation region, thus the absence of dilution adjacent to diluted region partially contributed to the observed "enhancement" gradients.

Passive tracers, computed along with the model simulation, reveal that contrary to previous studies (e.g. *Li et al.*, 2005; *Cooper et al.*, 2007; *Barth et al.*, 2012), boundary layer sourced tracer and stratospheric sourced tracer are simulated to have about the same value both within the North American Monsoon circulation and outside the anticyclone. On the other hand, it is shown that the air within the anticyclone has lower values of lateral boundary tracer, which includes clean air from locations such as the Pacific that can cause significant dilution outside. Thus, we hypothesize that the appearance of the ozone enhancement is not solely due to accumulation of boundary layer precursors as stated by *Li et al.* (2005), but also due to the lack of dilution relative to the Pacific Northwest. Finally, consistent with *Cooper et al.* (2007), lightning NO_x tracer shows enhanced values within the eastern-2/3 of the anticyclone, which subsequently enhances chemical production. However, the occurrence of this tracer enhancement can also be attributed to coincidence of regions with high flash rates instead of simply due to dynamics.

Finally, while $\mathsf{LNO_x}$ tracer shows an enhanced mean within the anticyclone region, the lower concentration on the western 1/3 over the Rocky Mountains indicate that the primary driver may not be the circulation, but rather the coincidence of high flash rate regions with the mean 9730 m geopotential height. To understand how lightning contributes to the observed ozone enhancement and its spatiotemporal variability, in the next chapter, we examine further the dynamical and chemical structure associated with the enhancement as well as the sensitivity of O_3 within the anticyclone to lightning NO_x emission.

Chapter 4

2006 North American Monsoon Case Study — Part II

Previous studies have identified upper tropospheric enhancements of ozone associated with the monsoons above North America, (*Li et al.*, 2005; *Cooper et al.*, 2009, and references therein), Asia (*Park et al.*, 2007; *Worden et al.*, 2009), and equatorial Africa (*Bouarar et al.*, 2011) during summers. *Cooper et al.* (2007) calculated an ozone enhancement of 29–52 ppbv between 10–11 km above Huntsville, Alabama. The observed upper tropospheric ozone enhancement has been linked to the North American Monsoon (NAM) anticyclonic circulation, which traps ozone precursors that subsequently enhance ozone production (*Li et al.*, 2005). *Cooper et al.* (2009) showed that more than 80% of the upper tropospheric NO_x ($\equiv NO + NO_2$) within the enhancement is due to lightning, and that it is responsible for 25–30 ppbv ozone at 250 hPa. Furthermore, it has been estimated that the ozone enhancement generates a positive radiative forcing of about 0.50 $W\,m^{-2}$ (*Cooper et al.*, 2007; *Choi et al.*, 2009). While these studies presented an overarching picture to explain the formation of the enhanced ozone and quantify its consequences, the details of the underlying physical and chemical processes remain unexplored. These previous studies also did not examine the nonlinearity of the sensitivity of ozone to the lightning-generated NO_x (LNO_x) tested.

This chapter examines the upper tropospheric ozone enhancement's spatial and temporal structures to quantify the advective, chemical, convective transport, and vertical mixing tendencies of upper tropospheric ozone during the North American Monsoon. Because of the importance of NO_x (*Cooper et al.*, 2009) and the uncertainty in the budget of LNO_x (*Schumann and Huntrieser*,

2007), this study focuses on analyses pertaining to the potential effects of LNO_x on the ozone enhancement and addresses the following questions:

(1) What is the vertical structure of the ozone chemical tendency? In order words, at which levels are ozone being produced?

(2) How does ozone chemistry respond to changes in LNO_x emission?

(3) What are the secondary effects of the response of ozone chemistry on LNO_x emission?

4.1 Model and methods

4.1.1 Model setup

Figure 4.1 shows the model domain for the WRF-Chem simulation performed for the 2006 North American Monsoon case study at 36 km horizontal grid size. Meteorology is initialized and nudged by the NCEP GFS reanalysis data.The Grell-3 convective parameterization scheme, a modified version of the *Grell and Devenyi* (2002) scheme, is used. In our simulations, the convective scheme is the primary source of precipitation. From this, we use the level of neutral buoyancy, reduced by 2 km (*Wong et al.*, 2013), as the cloud top height input for the *Price and Rind* (1992) lightning parameterization and scale the resulting flash rate down by a factor of 10 to obtain flash rates within $\sim 7\%$ of the National Lightning Detection Network (NLDN; *Cummins and Murphy*, 2009) observations.

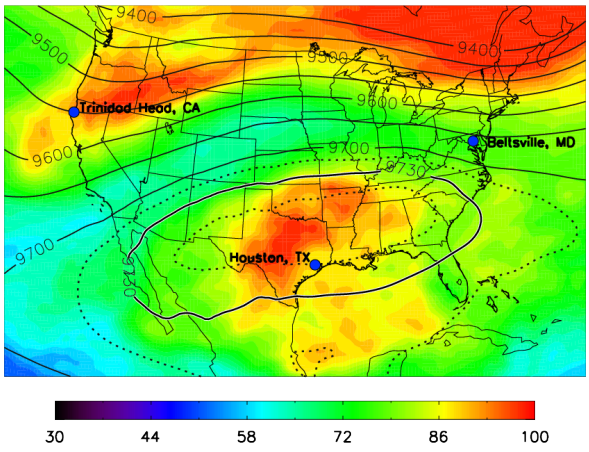

Figure 4.1: Simulated ozone (ppbv) and geopotential height (m) at 300 hPa averaged for August 2006. The three locations indicated on the map are used for the tendency analysis in Section 4.2.

The Regional Acid Deposition Model (RADM2; *Stockwell et al.*, 1990) is used for the chemical mechanism with the fast Tropospheric Ultraviolet-Visible (FTUV; *Tie et al.*, 2003) photolysis

scheme. Boundary and initial chemical conditions are defined by outputs from the Model for OZone and Related chemical Tracers (MOZART-4) global chemistry model (*Emmons et al.*, 2010). Additional model physics and chemistry options, as well as evaluation against in-situ and remote sensing observations are described in the previous chapter.

4.1.2 Diagnostic Outputs

In addition to the standard meteorological and chemistry outputs, we produced additional diagnostics computed within the model to aid our analysis. Three passive tracers representing the lateral boundaries (BC), the boundary layer (BL), and the stratosphere (ST) are used for air mass sourcing. These tracers are set to 1.0 at their respective sources (at the lateral domain boundaries, below the boundary layer height, and above the tropopause) at every time step. In the previous chapter, these tracers have been used to highlight that the anticyclonic monsoonal circulation prevents ozone-poor air from the western domain boundary from entering the anticyclone region, defined as the area with August mean geopotential height at 300 hPa greater than 9730 m. A LNO_x tracer is also emitted with the LNO_x emission. Each of the four tracers has a decaying twin with a lifetime of 24 hours. These tracers are transported by advection, convective transport, and mixing. In this chapter, we use these tracers to indicate, at specific locations, when $\mathsf{LNO_x}$, BL, and ST air is influencing the modeled air mass composition.

To diagnose what physical and chemical processes are contributing to the ozone variability in the upper tropospheric anticyclone, we have decomposed the tendency equation into its component operators $\mathcal{P}$: horizontal advection ($\mathbf{v} \cdot \nabla$), vertical advection ($w\delta_z$), convective transport (Δ_{conv}), vertical mixing/dry deposition (Δ_{vmix}), net chemical productions/losses (Δ_{chem}), emission (E), and other loss processes otherwise unspecified by the first five components such as wet deposition (L). Therefore, we may write the change of the mixing ratio of a chemical constituent C from time step t to $t+1$ as follow:

$$C^{(t+1)} - C^{(t)} = (\Delta_{chem} + \Delta_{conv} + \Delta_{vmix} + \mathbf{v} \cdot \nabla + w\delta_z)C^{(t)}\delta t + E_C^{(t)} + LC^{(t)} \tag{4.1}$$

We accumulate at every single time step the total tendency T for a chemical species C due to a single process p up to time t from initialization:

$$T_p^{(t)} = \sum_{\tau=0}^{t-1} \Delta_p S^{(\tau)} \delta\tau \tag{4.2}$$

All processes include nonlinear terms associated with the respective solver. The decoupled advective components are extracted from within the WRF dynamic core, while convective, vertical mixing, and chemical tendencies are computed by differencing the mixing ratios before and after their respective solver. Thus, no information is lost during the accumulation process. If $\langle E_C^{(\tau)} + LC^{(\tau)} \rangle_{\tau<t} = 0$, we may expect $\sum_{p\in\mathcal{P}} T_p^{(t)} \equiv C^{(t)} - C^{(0)}$ to hold. In the upper troposphere, emission (except for lightning-generated NO) should be zero as aircraft emission is not included in the simulations, and wet deposition of the species of interest (O_3, CO, $\mathsf{NO_x}$) is negligible. Thus the first five processes in Equation 4.2 should be sufficient in capturing the full tendency of these chemical constituents.

4.2 Tendency evalution

For the following analyses, we will be focusing on the three locations shown in Figure 4.1. The first location, Trinidad Head, California (40.80°N, 124.15°W), represents the continental inflow region, which is largely unaffected by conditions and air masses from within the anticyclone or contiguous United States (CONUS) in general. The modeled August average O_3 and geopotential heights show that Trinidad Head can have high O_3 due to stratospheric air just to the north (Figure 4.1) and remains outside of the anticyclone region. The second location is Houston, Texas (29.72°N, 95.40°W), representing the anticyclone region, which is the primary subject for this study. The third location, Beltsville, Maryland (39.04°N, 76.52°W), represents the continental outflow region, which periodically receives air from the jet and the anticyclone (Figure 4.1).

4.2.1 Temporal variability

The primary sources for local temporal variability are horizontal advection and vertical advection. Figure 4.2 shows the advective tendencies for ozone during August near Houston between 200–600 hPa, which includes mid-to-upper troposphere and encompassing altitudes covered by the remaining analyses performed in this study. Both the horizontal and vertical components are often the same magnitude as the total tendency. However, the combined advective tendency is frequently much smaller because the two components often have opposite signs. The residual tendency, i.e. the total ozone tendency without the two advective components, is the combined chemical, convective, and vertical mixing tendencies. It is useful to note that, because the components are not restricted to be either positive or negative, removing a tendency due to a specific process from the total tendency does not guarantee a smaller residual. In addition, while the time series shown is from Houston, the same results are applicable to the advective tendencies at other locations.

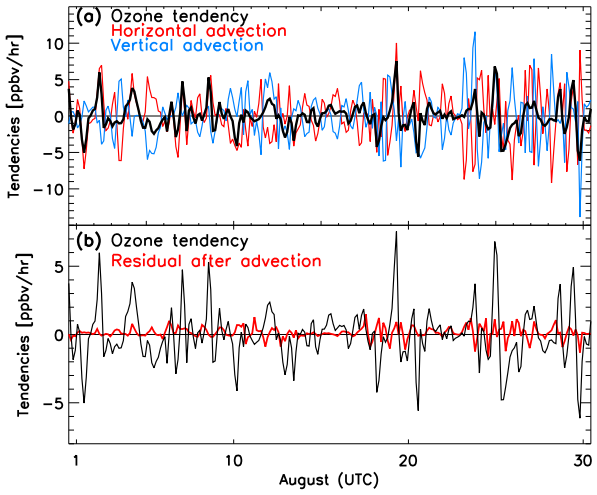

Figure 4.2: Ozone total tendencies (black lines) between 200–600 hPa, (a) horizontal (red) and vertical (blue) advective tendencies and (b) residual tendencies (red line) after removing advective components.

To characterize the residual tendency at the 300 hPa level, we examine the remaining components of the tendency accumulation equation (Eqn. 4.1) at the three locations between 270–330 hPa. All results are computed using the nearest 11 × 11 model grids to the IONS-06 site location. We find that the vertical mixing tendency is usually more than an order of magnitude smaller than the chemical and convective tendencies at this altitude, thus vertical component is omitted from the analysis and Figure 4.3. In addition to the time series of the two tendency components, Figure 4.3 shows the ozone mean mixing ratios and the range between its minimum and maximum values. To

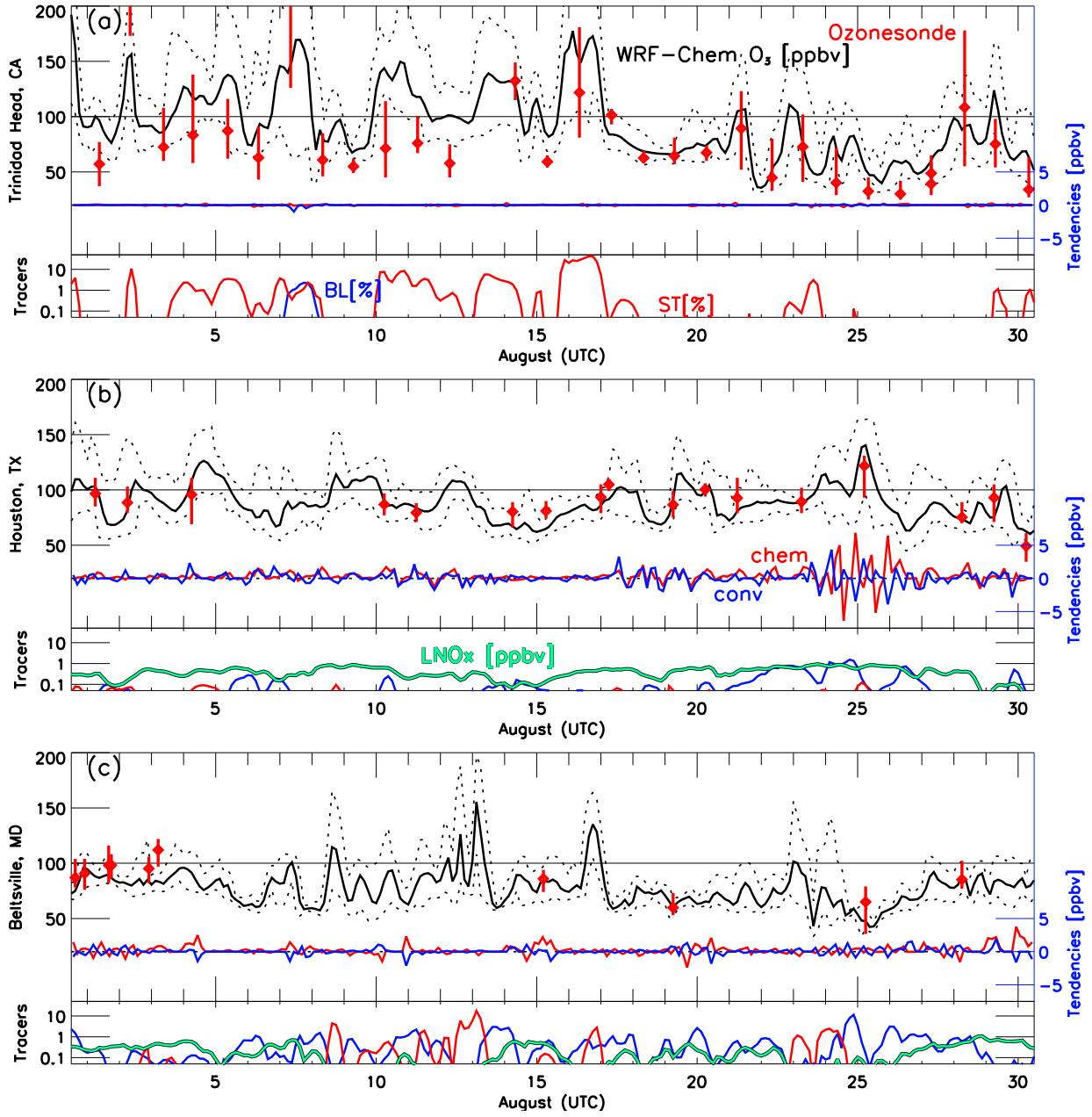

Figure 4.3: **Ozone mixing ratios, tendencies, and passive tracer time series** — Time series at (a) Trinidad Head, (b) Houston, and (c) Beltsville showing the minimum-mean-maximum ozone time series (black) between 270–330 hPa overlaid with IONS-06 ozonesonde measurements represented as red vertical lines for the range and solid ♢ for the mean value. Ozone chemical (red) and convective (blue) tendency components are given according to the right axis labels in units of ppbv accumulated for every 3-hourly output interval. Boundary layer (BL, blue) and stratospheric (ST, red) decaying tracers are given in %. LNO_x decaying tracer (green) is given in ppbv.

put into perspective the skill of the model in simulating the variability, distributions of ozonesonde measurements between 270 and 330 hPa from the IONS-06 campaign (*Thompson et al.*, 2008a) are overlaid on top of the model results. At the bottom of each panel, boundary layer (BL), stratospheric (ST), and lightning (LNO_x) decaying tracers are included to indicate time periods when these sources influenced the upper troposphere above each location.

Trinidad Head occasionally receives stratospheric ozone from the northern latitudes as evident in the ST tracer, which is responsible for the high ozone simulated for particular days (e.g. August 2 and August 7). The largest 3-hourly chemical tendency for Trinidad Head is 0.35 ppbv per 3 hours. This can be compared to that for advection, which has a mean 3-hourly absolute advective tendency of 82.8 ppbv. The accumulated August chemical tendency, including both positive and negative phases, is 0.096 ppbv, this can be compared to −2.0 ppbv for convective transport, 8.1 ppbv for vertical mixing, and −135 ppbv for the two advective tendencies combined. The large value from the advective tendency is the result of a high stratospheric ozone phase over Trinidad Head at the beginning of August and a low stratospheric ozone phase at the end of August. Thus, the ozone at Trinidad Head is controlled by the advective tendencies with vertical mixing and convective transport providing small contributions. The chemical tendency is negligible at this location.

Above Houston, August began with an event of high stratospheric contribution ($\sim$ 0.1% decaying ST) to O_3 and ended with negligible stratospheric contributions ($< 10^{-4}$%), thus resulting in a large accumulated total of −133 ppbv despite a large range of values if integrated for other periods. Chemistry is much more important here than Trinidad Head, the minimum/maximum chemical tendencies are −6.4/6.8 ppbv per 3 hours, a 20-fold increase from that in the continental inflow region. Moreover, the August total change due to chemical production is 80 ppbv, which is 3 orders of magnitude higher that that at Trinidad Head. The total convective tendency is also higher, with an August accumulated value of positive 12 ppbv. As will be shown in the next section, 300 hPa is well below the simulated main convective outflow level and experiences increases in ozone due to subsidence. Vertical mixing is substantially smaller (2 ppbv) due to generally smaller vertical gradients at 300 hPa above the southern United States. During August 23–26, there are

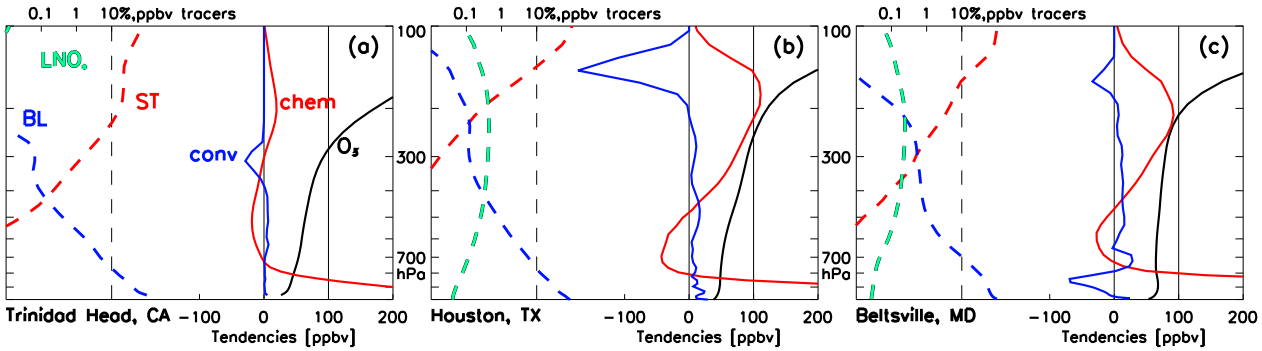

Figure 4.4: August average vertical profiles at (a) Trinidad Head, (b) Houston, and (c) Beltsville. Dashed lines are the mean 1-day decaying tracers for BL (blue, %), ST (red, %), and LNO_x (green, ppbv) according to the values on the top axis. Solid lines are the accumulated chemical tendency (red), convective tendency (blue), and the mean ozone profile (black) in ppbv according to the values of the bottom axis. The closest 11×11 grid points to each IONS-06 site are averaged to compute these profiles.

large convective transport and chemical tendencies. This event coincides with enhanced LNO_x and BL tracer values. However, due to comparably strong O_3 chemical losses, the accumulated total is much less than it would be otherwise.

Upper tropospheric air above Beltsville experienced $-2.4/3.8$ ppbv of minimum/maximum 3-hourly O_3 chemical tendency, with an August accumulated net change of 59 ppbv of O_3 due solely to chemistry. This value can be compared to the accumulated change due to convection (7.5 ppbv), vertical mixing (4.3 ppbv), and advection (-73 ppbv). Unlike Houston, however, Beltsville also shares some characteristics with Trinidad Head, both of which periodically receive high stratospheric ozone (e.g. August 8–13).

4.2.2 Vertical structure

While the time series analysis above, focusing at the pressure level (270–330 hPa) investigated by *Li et al.* (2005) (300 hPa) and near that by *Cooper et al.* (2007) (250 hPa), shows interesting variabilities, the vertical structure is not represented. Due to convective entrainment/detrainment, selected pressure levels can experience drastically different chemical properties. In the following analysis, we examine the August mean vertical structures of the chemical and convective tendency

components (Figure 4.4). As in the previous section, the ozone mixing ratios and passive tracer values are also provided to give context.

The continental inflow region (Trinidad Head) lacks both BL and LNO_x tracers in the upper troposphere. Despite having higher ozone mixing ratios than the other two locations, the accumulated chemical tendency remains low with a maximum of 19.4 ± 2.4 ppbv at 205 hPa, which is above the level of maximum convective outflow (300 hPa) at Trinidad Head. Because of the lack of LNO_x emission and in-situ chemical production, the ozone mixing ratio remains low between stratospheric intrusion or episodes of lowered tropopause, allowing the air to remain relatively "clean" until reaching Minnesota (Figure 4.1). This influx of low-ozone, chemically-"slow" air mass is responsible in generating the oval-shaped ozone enhancement that outlines the northwestern edge of the mean NAM circulation.

At Houston, near the center of the mean-state anticyclonic circulation, both the ozone chemical and convective tendencies are substantially higher than Trinidad Head. At 200 hPa, Houston experiences an August total change of 109 ± 17 ppbv due solely to chemistry, about 5 times higher than that in Trinidad Head. The largest O_3 chemical production occurs during the day, and is often partially balanced by O_3 chemical loss at night. On the other hand, ozone-poor air and BL tracers are transported into the upper troposphere through convection, detraining primarily at 145 hPa with a net change of -172 ppbv O_3 during August, in part caused by a nearby outlier with -1092 ppbv during the same period. The localized high convective tendency is an indication for stationary features such as convection triggered by coastlines or orography.

Beltsville, situated in the continental outflow region, shows small convective tendencies, with a peak at 175 hPa, but BL tracers and chemical tendencies are comparable to those at Houston. At the same time, Beltsville also experiences periodically high stratospheric ozone events in the upper troposphere similar to those at Trinidad Head. With these diagnostics, it can be inferred that the primary source for ozone precursors, including LNO_x in the continental outflow region is the advective influx from upwind regions rather than vertically transported from the local boundary layer via convection. This is contrary to that within the anticyclone, where chemical production

of ozone in the upper troposphere is enhanced by precursor sources located directly below at the boundary layer, as indicated by the simultaneous enhancements in both convective transport and chemical tendencies. An in-depth analysis of the ozone budget and variability at Beltsville and New England can be found in *Thompson et al.* (2007a,b), wherein data from IONS-4, the predecessor of IONS-06, are utilized. They found that tropospheric ozone in northeastern North America was composed of 10–15% BL sources, 10–15% regional sources including lightning, 20–25% stratospheric ozone, and $\sim$ 50% recently advected or aged air from elsewhere. While we do not produce exact values, the rankings from their study and those found in the present study for Beltsville are largely consistent.

4.3 Sensitivity to lightning

4.3.1 Spatial distribution

Cooper et al. (2007) attributed much of the enhanced upper tropospheric ozone in the anticyclone to $\mathsf{NO_x}$ produced by lightning. To understand the how $\mathsf{LNO_x}$ affects the ozone enhancement, we compare results from the control simulation, i.e. the simulation used in the previous section, to two additional sensitivity simulations. The first sensitivity simulation is a no-lightning case, where the lightning $\mathsf{NO_x}$ emission is suppressed entirely. The second sensitivity simulation is a high-$\mathsf{LNO_x}$ case, where lightning flash rate is 10 times greater than the control case. This scenario tests the case wherein model may substantially underestimate $\mathsf{LNO_x}$ with the potential of $\mathsf{NO_x}$-titration, which has been measured within convective outflows of large storms (e.g. *Stith et al.*, 1999; *Ridley et al.*, 2004; *Ott et al.*, 2007; *Cummings et al.*, 2013). The resulting mean spatial distributions of NO_x, HO_x, CO, and O_3 at 300 hPa during August are shown in Figure 4.5.

Although the no-lightning scenario shows higher ozone within the anticyclone compared to the immediate surrounding areas, there is an overall low bias compared to ozone observations (see previous chapter). In comparing results from the different simulations, we find NO_x is substantially increased within the anticyclone above background values in the Pacific Northwest region from

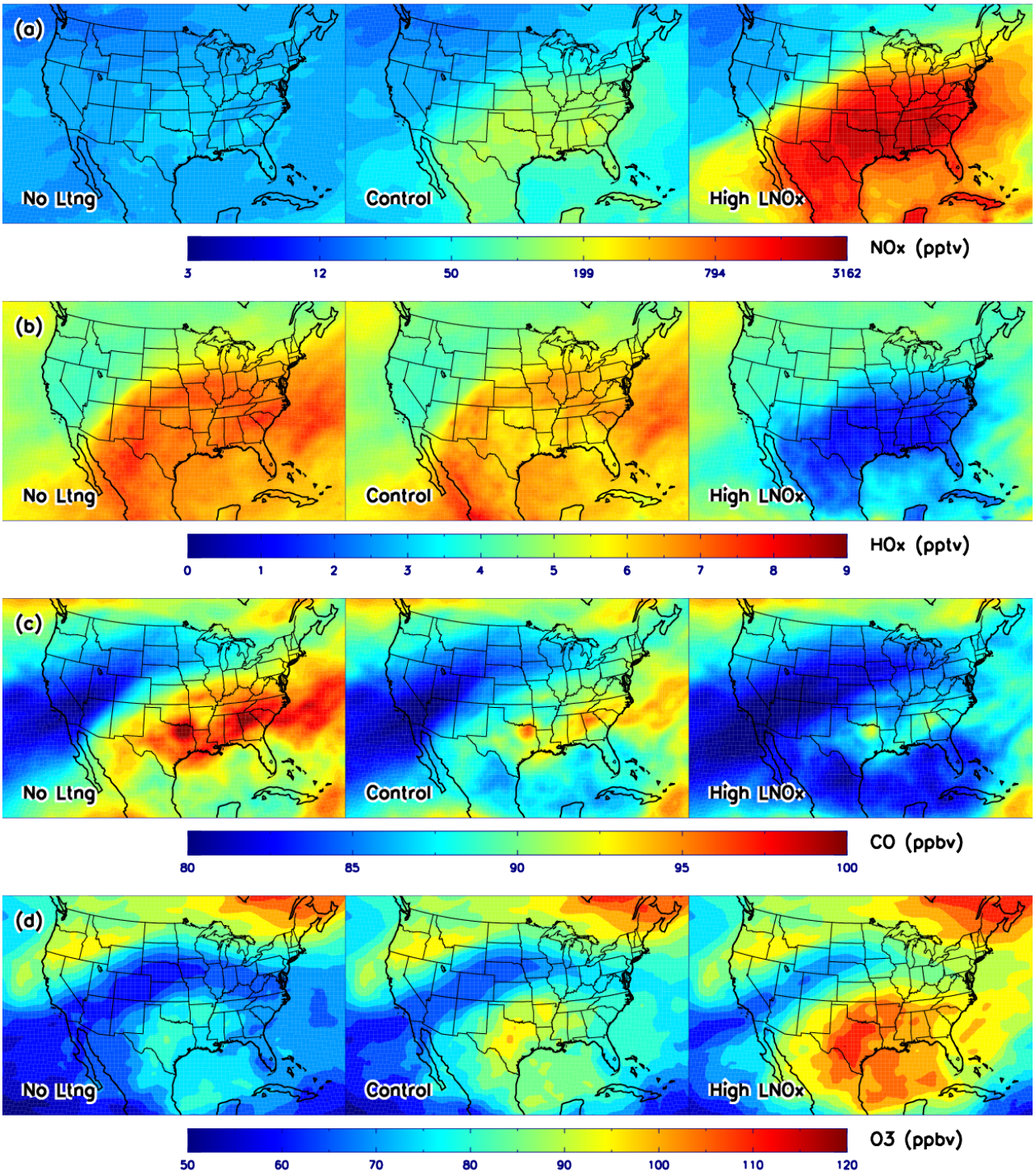

Figure 4.5: Model simulated mean (a) NO_x, (b) HO_x, (c) CO, and (d) O_3 for no-lightning (left column), control (center column), and high-LNO_x (right column) scenarios at 300 hPa during August. Note that NO_x is contoured on a log scale while the rest are contoured on linear scales.

31.6 ± 4.5 pptv to 135 ± 35 pptv in the control case and 1680±540 pptv in the high-$\mathsf{LNO_x}$ case. The contribution of total $\mathsf{NO_x}$ mixing ratio from $\mathsf{LNO_x}$ can be calculated as,

$$\Delta[\mathsf{NO_x}] = [\mathsf{NO_x}] - [\mathsf{NO_x}]_0 = (1 - f)[\mathsf{LNO_x}]$$

where f is the fraction loss of $\mathsf{LNO_x}$ in the atmosphere due to chemistry or deposition and $[\mathsf{NO_x}]_0$ is the $\mathsf{NO_x}$ mixing ratio without lightning. For small changes in the atmospheric composition, f should be constant and thus the addition of $\mathsf{LNO_x}$ is expected to linearly increase $[\mathsf{NO_x}]$. If one assumes that the change between no-lightning and control cases is linear, extrapolating to the high-$\mathsf{LNO_x}$ case would give 1070 pptv, which is less than the 1100–2200 pptv simulated. This is due to the decrease in $\mathsf{HO_x}$ (as discussed below), the primary reagent converting $\mathsf{NO_x}$ into reservoir species, in response to increasing $\mathsf{LNO_x}$. Subsequently, we have $\partial f/\partial[\mathsf{LNO_x}] < 0$, resulting in a superlinear increase of $\mathsf{NO_x}$.

$\mathsf{HO_x}$ is substantially decreased with increasing $\mathsf{LNO_x}$ emission. The initial August mean mixing ratio at 300 hPa without lightning is 6.94 ± 0.38 pptv within the anticyclone. This is larger than the ∼4–5 pptv in the Pacific Northwest and inflow regions. It is slightly decreased to 6.27 ± 0.37 pptv in the control simulation, or a 10% decrease from the no-lightning scenario. For the high $\mathsf{LNO_x}$ scenario, $\mathsf{HO_x}$ is further decreased to 1.80 ± 0.59 pptv, far below the value of the Pacific Northwest, and is 71% less than the control simulation, which is a larger decrease than that would have been obtained if one were to extrapolate the initial 10% decrease with an exponential model ($\sim 61\%$). The decreasing $\mathsf{HO_x}$ with increasing $\mathsf{NO_x}$ is the result of its interactions with O_3, $\mathsf{NO_x}$, and CO after production from $\mathsf{O(^1D) + H_2O}$, which is presumably proportionally increasing with the increased level of O_3.

Even though $\mathsf{CO + OH \rightarrow CO_2 + HO_2}$ is the only chemical loss pathway for CO specified in RADM2 and that $\mathsf{HO_x}$ is substantially decreased by a factor of 3.8 from no-lightning to high-$\mathsf{LNO_x}$, CO is simulated to decrease with increasing lightning. Without lightning, the August mean mixing ratio for CO is 92.8 ± 2.8 ppbv within the anticyclone. This is reduced to 89.8 ± 2.4 ppbv for the control simulation and 85.5 ± 2.4 ppbv for the high-$\mathsf{LNO_x}$ simulation. The anti-correlation of CO

with $\mathsf{LNO_x}$ is due to the primary effect of reduced in-situ production of CO from various VOC oxidations by OH.

Finally, O_3 is increased with increasing $\mathrm{LNO_x}$, consistent with prior studies on this subject (e.g. *Cooper et al.*, 2007; *Allen et al.*, 2010). Ozone mixing ratio is increased from 74.5 ± 5.3 ppbv to 86.4 ± 6.7 ppbv (+16%) at 300 hPa, which is a smaller increase than that found by *Cooper et al.* (2007). In the high-$\mathrm{LNO_x}$ case, averaged O_3 is further increased to 101.1 ± 6.8 ppbv, a 26.6 ppbv or 36% increase relative to the no-lightning scenario. The reduced sensitivity of O_3 to $\mathrm{LNO_x}$ at higher flash rates indicates a negative feedback process at play despite the superlinear increase in $\mathsf{NO_x}$ for the high-$\mathsf{LNO_x}$ scenario.

4.3.2 Vertical structure

Vertical distributions of species mixing ratios and tendencies are also affected by the $\mathsf{LNO_x}$ emission factor. Figure 4.6 shows the vertical profiles for O_3, CO, and $\mathrm{NO_x}$ and their tendencies from the three simulations averaged within the anticyclone column. With the exception of O_3 and $\mathrm{NO_x}$ in the high-$\mathrm{LNO_x}$ scenario, the shapes of the mixing ratio vertical profiles are consistent across simulations. When considering only the magnitude of changes, the greatest effect of $\mathrm{LNO_x}$ emissions on ozone occurs in the 300–500 hPa layer. The ozone mixing ratio increases by 33 ppbv in the control simulation compared to the no-lightning simulation. The ozone chemical tendency for August also increases substantially in this layer from -29 ppbv to $+187$ ppbv for the no-lightning to high-$\mathsf{LNO_x}$ cases. On the other hand, despite having a $\mathrm{LNO_x}$ emission peak in the mid-troposphere as prescribed according to *Ott et al.* (2010), $\mathrm{NO_x}$ is enhanced most prominently at the ~ 170 hPa level from 84 pptv to ~ 3 ppbv. This increase, together with the reversal in ozone chemical tendency at this level, suggests that $\mathrm{NO_x}$-titration potentially occurs.

In all simulations, the August mean ozone chemical tendencies within the anticyclone are positive in the boundary layer (BL) due to surface emissions, become negative just above the BL, then become positive again in the mid-troposphere, and remain positive up to the tropopause or higher. The mid-tropospheric altitudes at which the signs of the accumulated chemical tendencies

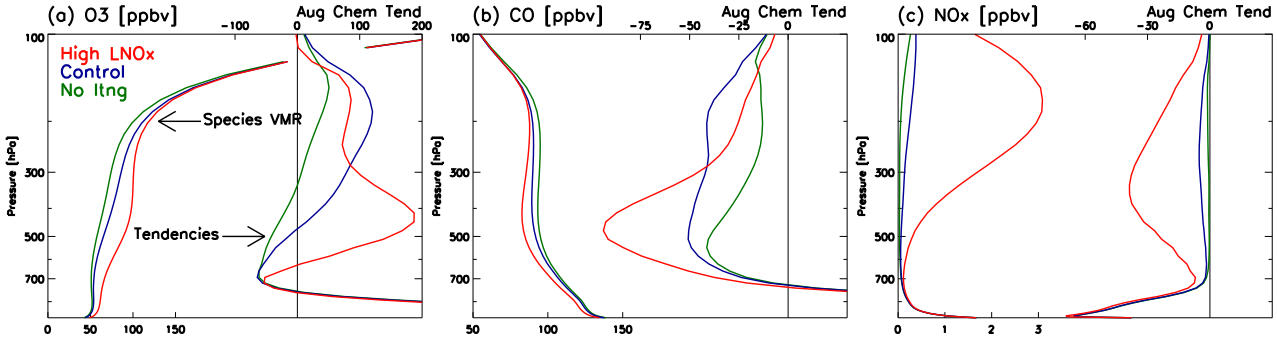

Figure 4.6: August mean mixing ratios and accumulated chemical tendencies for (a) O_3, (b) CO, and (c) NO_x within the anticyclone region for the no-lightning (green), control (blue), and high-LNO_x (red) scenarios. Means are computed on model levels, and then gridded by the mean pressure.

return to positive are due to positive production above a negative background loss rate enhanced by LNO_x. Without lightning, the lowest level with a positive O_3 chemistry tendency in the free troposphere is $\sim$ 340 hPa. In the control scenario, the switch from negative to positive chemistry tendency drops to the $\sim$ 470 hPa level. This is further lowered to $\sim$ 630 hPa with the high-LNO_x scenario. Thus, the vertical distribution of LNO_x, which impacts the vertical profile of ozone's sensitivity to the emission parameter, can directly perturb the structure and vertical extent of the ozone enhancement by influencing the level at which net ozone production is attained.

The mixing ratio of NO_x increases superlinearly in the upper troposphere due to LNO_x emissions between the control and high-LNO_x simulations, as was discussed previously. Consequently, the presence of the exceedingly high NO_x induces a decrease in the chemical production of O_3. While NO_x-titration has been suggested to be possible during intense thunderstorms (e.g *Cummings et al.*, 2013), the persistent occurrence of NO_x-titration has not been observed and the result of this simulation is likely only an artifact as a result of the 10-fold increase in lightning production, and is further amplified by the reduced NO_x loss rate to HNO_3.

4.3.3 Diurnal variabilities

As shown in Figure 4.3, Houston experienced strong negative phases in its ozone chemical tendency, which partially negated the accumulated daytime production. To determine the response of ozone chemistry to lightning, it is thus necessary to take into account daytime versus nighttime chemistry as not to include nocturnal loss into the budget for daytime NO_x-titration. To do so, Figure 4.7 shows the daytime ozone production separated from nighttime losses between 150–300 hPa within the anticyclone. The daytime tendencies are extracted from 15–21 UTC and the nighttime tendencies are extracted from 3–9 UTC. The diurnal variability in the mean values of species mixing ratio are negligible, and thus only daytime values are shown. Due to interconversion between O_3 and NO_2, we also examine odd oxygen $O_x \equiv O_3 + NO_2$ instead of NO_2 in the following analysis.

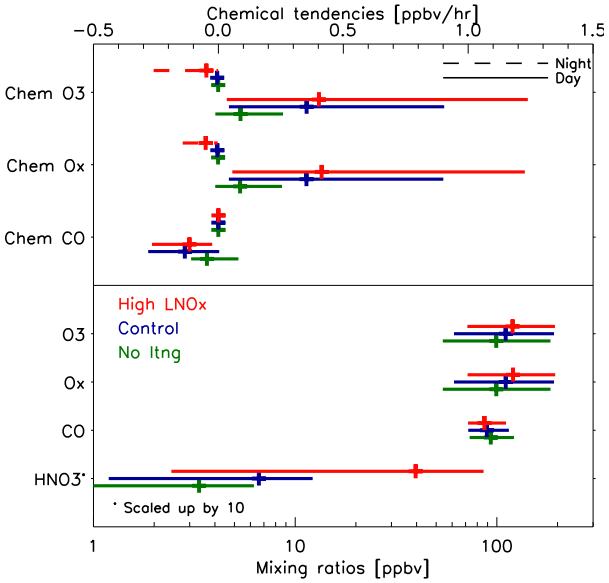

Figure 4.7: **Diurnal variability in tendency and mixing ratio frequency distributions** — Distributions (5pct-mean-95pct) of chemical tendencies and mixing ratios for O_3, O_x, CO, and the mixing ratio for HNO_3 between 150–300 hPa during August within the anticyclone. Nighttime (3–9 UTC) tendencies are represented by dashed lines while daytime (15–21 UTC) tendencies are represented by solid lines.

Without lightning, the mean daytime O_3 chemical tendency is 0.088 ppbv/hr and the 95th-percentile is 0.259 ppbv/hr. For the control case, the daytime mean and 95-pct respectively increase to 0.353 ppbv/hr and 0.904 ppbv/hr. However, further increasing LNO_x to the high-LNO_x scenario only slightly increases the mean ozone chemical tendency to 0.403 ppbv. Considering the combined all-day accumulated tendency, which decreased between the two scenarios with lightning (Figure 4.6a), it is apparent that the nighttime loss phase plays in important role in modulating the total response of ozone chemical tendencies to changes in the lightning emission factor.

Nonetheless, the lowered sensitivity in the daytime chemistry alone still supports the conjecture that NO_x-titration is occurring albeit not as strongly as implied by Figure 4.6a.

Comparing the changes in the distributions of chemical tendencies for O_3 and O_x, it is apparent that the bulk of the ozone losses in the high-LNO_x scenario is due to conversion to NO_2. This is also supported by the increase in HNO_3 from 6.6 ppbv in the control case to 39.6 ppbv in the high-LNO_x case.

Without photolysis, the nighttime maximum O_3 tendencies are all near zero. Thus, without net O_3 production, we can define zero as the baseline and evaluate the sensitivities as relative changes. Without lightning, the ozone loss is 0.90 pptv/hr with the 5th-percentile at 2.93 pptv/hr. The mean loss is increased to 5 pptv/hr (5.6×) and the 5th-pct is increased to 25.8 pptv/hr (8.8×) in the control scenario. Increasing LNO_x by a factor of 10, the mean nighttime O_3 loss is now 48.2 pptv/hr, a 9.5× increase from the control simulation; slightly-sublinear change relative to the increase in emission. Finally, the loss near the left tail of the distribution increases linearly at both the 5th-percentile (25.8 → 259 pptv/hr) and minimum (0.179 → 1.78 ppbv/hr).

4.3.4 NO_x-titration

While it is evident that the high-LNO_x scenario produces unrealistic concentrations of NO_x in the troposphere, > 3 ppbv of NO_x has been observed within convective outflows of large storms (e.g. *Stith et al.*, 1999; *Ridley et al.*, 2004; *Ott et al.*, 2007; *Cummings et al.*, 2013). Thus it is useful to understand the chemistry thresholds that triggered the negative response in ozone chemistry. A steady-state analysis on ozone production and loss terms can be done following the method outlined by *Kleinman et al.* (1997). In a photostationary steady-state, the radical production rate Q is equal to the total loss rate, characterized by radical-radical reactions L_R (e.g. $\mathsf{HO_2 + HO_2}$) and radical-nitrogen reactions L_N (e.g. $\mathsf{NO_2 + OH}$). That is, $Q = L_R + L_N$. The response of ozone production to the available NO can then be quantified as follow (*Kleinman et al.*, 1997):

$$\frac{d \ln P(\mathsf{O_3})}{d \ln[\mathsf{NO}]} = \frac{1 - 3/2\, L_N/Q}{1 - 1/2\, L_N/Q} \tag{4.3}$$

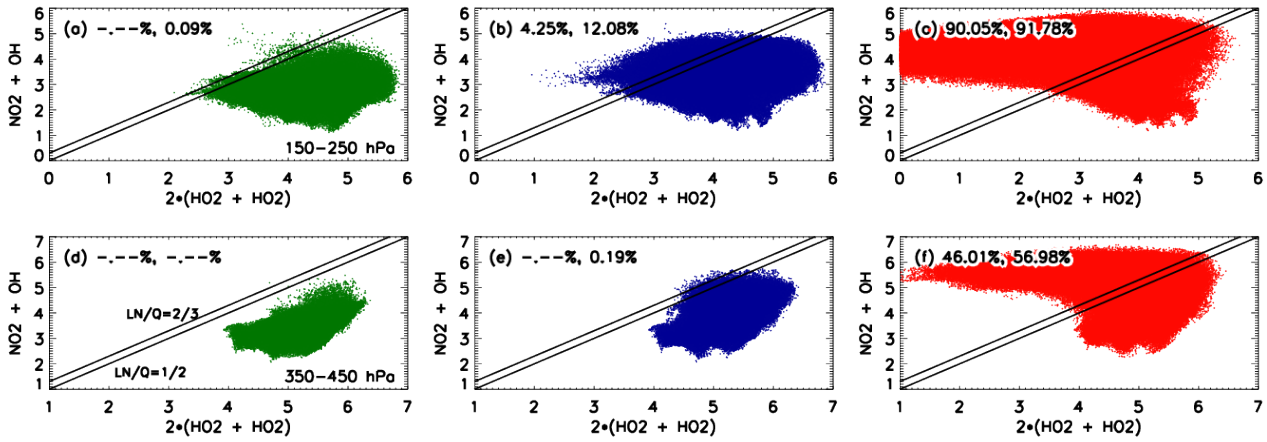

Figure 4.8: Daytime reaction rates ($\log_{10}$ molec. cm^{-3} s^{-1} for NO_2+OH and (2×) HO_2+HO_2 at 150–250 hPa (a–c) and 350–450 hPa (d–f) without lightning (a,d), control simulation (b,e), and high LNO_x scenario (c,f). The left percentage (if present) is the fraction of data points where $L_N/Q > 2/3$. The right, or the only one, percentage (if present) is that of $L_N/Q > 1/2$.

where L_N/Q is the fraction of free radicals removed by NO_x. In the upper troposphere, L_N and L_R can be approximated by the reaction rate of $\mathsf{NO_2 + OH}$ and twice the rate of $\mathsf{HO_2 + HO_2}$, respectively. For consistency with the simulated chemistry, all offline computations are conducted using the rate equations and parameters from RADM2 (*Stockwell et al.*, 1990, and references therein). Using August data points at 15, 18, and 21 UTC within the anticyclone column between 150–250 hPa and 350–450 hPa, the daytime reaction rates $L_N = k[\mathsf{NO_2}][\mathsf{OH}]$ and $L_R = 2k'[\mathsf{HO_2}][\mathsf{HO_2}]$ are plotted in Figure 4.8. *Kleinman et al.* (2001) showed that a VOC-sensitive regime is in place when $L_N/Q > 0.5$, compared to the NO_x-sensitive regime below this threshold. Further, $L_N/Q > 2/3$ is favorable for NO_x-titration, i.e. production of ozone is expected to decrease with further increases in NO_x, as demonstrated by Equation 4.3. Thus, if the majority of air masses lies above the 2/3 threshold, an overall decrease in ozone production or even net loss can be expected to occur.

The percentage of data points where $L_N > L_R$, or $L_N/Q > 1/2$, and $L_N/Q > 2/3$ are computed at both levels for all three sensitivity simulations. When lightning is suppressed, nearly all data points lie within $L_N/Q < 1/2$, which means that the upper troposphere in the anticyclone is NO_x-sensitive. In the control simulation, about 12% in the upper troposphere is VOC-sensitive,

but below 350 hPa almost all HO_x continues to be terminated by radical-radical reactions. In the high-LNO_x simulation, 92% and 57% of the data points are within the VOC-limited regime ($L_N/Q > 1/2$) for the two pressure ranges. The fraction of data points where the expected response of $P(O_3)$ to [NO_x] is negative ($L_N/Q > 2/3$) are 90% for 150–250 hPa and 46% for 350–460 hPa.

Thus, for a reasonable LNO_x emission scenario, i.e. similar to that in our control case, 10% or more of the upper tropospheric air mass is VOC-sensitive and about 4% is in the NO_x-titration regime.

4.3.5 Convective transport

The result of convective transport detrainment and mixing, i.e. convective tendency, depends on the differences in ozone mixing ratios between model vertical levels. If entrainment occurs at high ozone levels, detrainment at low ozone levels would be positive. On the contrary, if low ozone levels are entrained and detrainment occurs at high ozone levels, convective tendencies at the detrainment level would be negative.

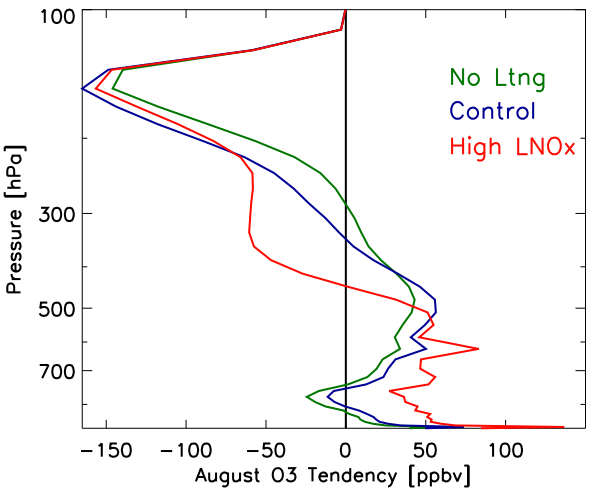

Figure 4.9: Vertical profiles of accumulated ozone convective tendency during August for the three lightning sensitivity simulations within the anticyclone column.

Due to changes in the vertical profiles of mixing ratios, and thus vertical gradients, convective tendencies are also affected by the LNO_x emissions (Figure 4.9). While it still holds true that convection dilutes upper tropospheric ozone by detraining ozone-poor air from the lower levels, changes in ozone due to convection are very different below the maximum detrainment level for different emission scenarios. In particular, due to the deeper enhancement (high ozone at lower altitude), a net negative convective tendency is observed above 440 hPa with high-LNO_x. Lightning NO_x emission also impacts surface air quality via the mid-to-upper tropospheric ozone enhancement,

as observed by the increasingly positive convective tendencies below 600 hPa. The accumulated ozone convective tendency through convective subsidence in the lower troposphere increase from 17–56 ppbv without lightning to 26–74 ppbv in the control case and 59–140 ppbv in the high-LNO_x case.

Therefore, increases in ozone mixing ratio throughout the troposphere (Figure 4.6a) changes the ozone convective tendency. Subsequently, ozone-poor air is transported to a deeper region of the upper troposphere (Figure 4.9) and increases ozone in the lower troposphere.

4.4 Summary

In this study, we have conducted simulations to examine the details of the 2006 North American Monsoon upper tropospheric ozone enhancement. The main results can be summarized as follow:

(1) Maximum chemical productions in the free troposphere at the continental inflow, outflow, and anticyclone regions occur in the upper troposphere near 150 hPa, situated above a layer of chemical loss in the mid-troposphere, forming a mirrored-"S" shaped vertical structure with the positive production near the surface;

(2) While LNO_x monotonically increases ozone and decreases carbon monoxide mixing ratios within the upper tropospheric anticyclone, chemical tendencies for both species show reversals in response to LNO_x at the high-NO_x regime wherein LNO_x is a factor of 10 higher than that in the control case; about 4% of data points in the control case lies within the NO_x-titrating regime, which is drastically increased to $\sim 90\%$ in the high-LNO_x case.

(3) As a result of non-uniform and nonlinear responses throughout the tropospheric column, ozone vertical gradients are modified with different lightning emission rates, which subsequently impact the simulated vertical structure of the ozone convective tendency.

The spatial structures and chemical pathways are highly non-uniform and its responses to perturbations in lightning emission scenarios are not monotonic. The super-linear sensitivity of NO_x

to lightning flash rate also causes NO_x-titration to occur more frequently than if the sensitivity is linear. To constrain lightning flash rate, thus constraining ozone chemistry, one may utilize lightning observations, e.g. *Cooper et al.* (2009) used the observed CG flash rate from NLDN. As more expansive data from total lightning (IC+CG) monitoring instruments and networks are being made available, it is possible to revisit the flash rate assimilation approach again with higher confidence. However, because the vertical distribution of LNO_x has significant impacts on the resulting ozone chemistry as shown by *Pickering et al.* (1998), it is also important to guarantee that convection and emission are spatially and temporally co-located so that convective tendencies are property simulated.

Finally, while lightning is shown to be an important factor for ozone production within the NAM circulation, anthropogenic emission and biogenic emission have also been shown to contribute to ozone production within the NAM upper tropospheric anticyclone (*Li et al.*, 2005). Therefore, additional sensitivity studies investigating these two emission sources would be valuable in revealing further details of this phenomenon and thus constraining the tropospheric chemical and radiative budgets.

Chapter 5

Summary

Ozone in the troposphere acts as a greenhouse gas and causes harm to the ecosystem. The recurring upper tropospheric ozone enhancement during the North American Monsoon has been shown to perturb upper tropospheric ozone by more than 20 ppbv above background values, which leads to a radiative forcing up to $0.50\,\mathrm{W\,m^{-2}}$ (*Li et al.*, 2005; *Cooper et al.*, 2007; *Choi et al.*, 2009). Of all the meteorological and chemical processes that contributes to the ozone enhancement, lightning-generated nitrogen oxides (lightning $\mathrm{NO_x}$, or $\mathrm{LNO_x}$), is shown to be the most prominent factor, which contributes 25–30 ppbv of the ozone maximum at 250 hPa(*Cooper et al.*, 2007). It is important to note that $\mathrm{LNO_x}$ emission is largely unconstrained with a global annual estimate of $5 \pm 3\,\mathrm{Tg\,a^{-1}}$ (*Schumann and Huntrieser*, 2007). Despite the uncertainty, only a few studies have investigated $\mathrm{LNO_x}$ or lightning flash rate parameterization at the regional scale (e.g. *Allen et al.*, 2010, 2012; *Barth et al.*, 2012; *Wong et al.*, 2013). Despite advancements in the physical formulations for the parameterization (*Barthe et al.*, 2010, and references therein), the *Price and Rind* (PR92; 1992) method based on cloud top height continues to show merits despite its own limitations (*Boccippio*, 2002).

To apply PR92 to the 2006 case study, we have implemented PR92 into WRF-Chem (Apdx C). The performance of this implementation has been evaluated (*Wong et al.*, 2013, and Ch. 2) and the results are summarized as follow. It is found that the statistics generated by a 3-month meteorological simulation are comparable ($\sim 2.4\times$ for 2006, $\sim 1\times$ for 2011) to observations from NLDN and ENTLN with a 2- km cloud-top reduction, which is included to reconcile the differences between the

level of neutral buoyancy (LNB) cloud-top proxy and radar reflectivity cloud-top. This reduction is selected to be an appropriate adjustment given a sufficiently large number of convective events. Thus, it does not guarantee applicability for individual storm. However, the IC : CG ratio produced by the *Price and Rind* (1993, PR93) method is shown to generate a erroneous drop-off in the histogram and is thus deemed unreliable. Finally, it is shown that the resolution dependency factor from *Price and Rind* (1994, PR94) is not applicable for a convective parameterized model due to the interpretation of cloud-top heights within a grid. To reconcile differences in model resolution, we suggest scaling by areal ratio to 36 km, at which convective core density (number of core per grid) is expected to be close to unity. However, it should be noted that the base resolution (36 km) may vary spatially or dependent or storm scale.

Due to differences in the simulated meteorology, flash rate is overestimated by a factor 10 in the 2006 case study, compared to the factor of 2 from the simulation evaluated in Chapter 2. The overpredicted $\mathsf{LNO_x}$ emission subsequently leads to a more severe upper tropospheric ozone enhancement. The ozone mixing ratio is simulated to be about 21% higher than that observed by TES. Similarly, CO is shown to be high compared to TES due to lower OH as the result of excessive $\mathsf{O_3}$ and $\mathsf{NO_x}$, but validation against MOPITT shows negligibly low biases in the upper troposphere. Formaldehyde is validated against SCIAMACHY retrievals from KNMI TEMIS. Because of the high uncertainties (σ_N) in the retrieved values, majority of the data points lie within $\pm 1\sigma$ despite low apparent correlations. On the other hand, $\mathsf{NO_2}$ is shown to be over-predicted for events $> 2 \times 10^{15}$ molec. cm^{-2}, which is expected due to excessive $\mathsf{LNO_x}$.

The differences between the chemistry within the anticyclone and that outside are evaluated based on tracer-tracer correlations, passive tracer diagnostics, and tendency diagnostics. It is concluded that contrary to previous studies, the NAM anticyclonic circulation does not sufficiently increase the amount of boundary layer air detrained into the upper troposphere above that in the surrounding area. On the other hand, the lack of influence from the air outside the anticyclone on the air inside, as quantified by the tracer-tracer correlations and lateral boundary tracers, sufficiently distinguishes the composition within the anticyclone from that outside.

To quantify the impact of model biases as well as the sensitivity of ozone to LNO_x emissions, additional simulations are performed without lightning and with reduced lightning tuned according to the flash rate validation. It is shown that as a result of the super-linear response of upper tropospheric NO_x mixing ratios to LNO_x, ozone production crosses the threshold beyond which NO_x-titration occurs, thus reducing and eventually reversing the sensitivity at the detrainment level (150–250 hPa). Furthermore, changes in the ozone vertical profile due to lightning emission also sufficiently modified the vertical gradients, which subsequently affected the resulting convective tendencies, thus forming a nonlinear feedback between convective transport and chemistry.

The contributions to the ozone enhancement from anthropogenic and biogenic emissions are also examined through sensitivity experiments, wherein the respective emission sources are suppressed. In the experiment pertaining anthropogenic emission, VOC, with CO as the proxy, is observed to be the controlling factor in the sensitivity. Due to NO_x-titration, upper tropospheric ozone production responds negatively to the increase in anthropogenic emission. On the other hand, biogenic emission is responsible for NO_x-losses in the upper troposphere (within the NO_x-titration regime), which subsequently allows higher net ozone production (again, within the NO_x-titration regime). It should be noted that this result is partially a consequence of excessive LNO_x within the model, which pushes the upper tropospheric chemistry into the NO_x-titration regime. A similar experiment is conducted by *Li et al.* (2005) and found that enhancements in CO as a result of these emissions are the primary pathway of how these chemical sources contribute to the ozone enhancement.

In conclusion, and directly responding to the questions raised in Chapter 1:

(1) WRF-Chem is able to simulate the occurrence of the ozone enhancement despite an order of magnitude bias in NO_x as the result of parameterizing lightning based on parameterized convection;

(2) In situ chemical production is the dominating tendency for the long term variability of the ozone enhancement after filtering out the advective component. However, contrary to

results from previous studies (e.g. *Li et al.*, 2005; *Cooper et al.*, 2007; *Barth et al.*, 2012), the anticyclone does not create a distinctive region wherein boundary layer air is aged above levels in the surrounding area;

(3) Lightning-generated $\mathsf{NO_x}$ emission is responsible for 16% increase in upper tropospheric ozone in the control and high-$\mathsf{LNO_x}$ scenarios at 300 hPa. On the other hand, anthropogenic emission is responsible for $\sim 6\%$ and biogenic emission is responsible for $\sim 13\%$ with high $\mathsf{LNO_x}$ emission.

5.1 Perspectives and outlook

Despite the ozone enhancement being a relatively self-contained feature, its spatial structures and chemical pathways are highly non-uniform and its response to perturbations in the emission scenarios are often not monotonic. Thus, to obtain more definitive results, studies focusing on specific scenarios and conditions are required to narrow down on specific chemical or meteorological regimes. In order words, it is insufficient to simply define a process such as convective transport and examine its link to the ozone enhancement. Furthermore, the initially super-linear sensitivity to lightning-generated $\mathsf{NO_x}$ also demands a finely tuned lightning parameterization or one that is less sensitive to biases in the convective parameterization, which is further complicated by the feedbacks between chemistry and convective transport. Several potential improvements to this study and remaining questions follow.

Flash rate assimilation, as done by *Cooper et al.* (2009), can potentially increase the fidelity of lightning $\mathsf{NO_x}$ emission in the model and thus the ozone chemistry. As total lightning monitoring instruments are being expanded or deployed(e.g. NLDN, ENTLN, GOES-R), and the data becoming available, it is possible to revisit this approach again. However, because the vertical distribution of $\mathsf{LNO_x}$ emission has significant impacts on the resulting ozone chemistry (*Pickering et al.*, 1998), it is also important to guarantee that convection and lightning colocate. Thus, short simulations

that re-initialize frequently may be the preferred mode of simulation as opposed to season-long simulations for the flash-rate-assimilated approach to avoid model drift in meteorology.

While it has been shown that anthropogenic and biogenic emissions affect the ozone enhancement through different mechanisms, the precise chemical pathways are yet to be determined. Therefore, additional analyses aiming to understand the differences in chemistry are recommended. Examples of the suggested analyses have already been done for the sensitivity of ozone to $\mathsf{LNO_x}$ emission (see Sect. 4.3) as well as for peroxy radical formation by *Barth et al.* (2012). However, the large number of emitted species from anthropogenic and biogenic sources, and subsequently the number of reactions involved, will undoubtedly complicate the analysis. Hence, it is recommended that these studies be performed with minimal scope to maximize focus.

References

Allen, D., K. Pickering, G. Stenchikov, A. Thompson, and Y. Kondo (2000), A three-dimensional total odd nitrogen (NO y) simulation during SONEX using a stretched-grid chemical transport model, *J. Geophys. Res.*, *105*(D3), 3851–3876, doi:10.1029/1999JD901029.

Allen, D., K. Pickering, B. Duncan, and M. Damon (2010), Impact of lightning NO emissions on North American photochemistry as determined using the Global Modeling Initiative (GMI) model, *J. Geophys. Res.*, *115*(D22), doi:10.1029/2010JD014062.

Allen, D. J., and K. E. Pickering (2002), Evaluation of lightning flash rate parameterizations for use in a global chemical transport model, *J. Geophys. Res.*, *107*(D23).

Allen, D. J., K. E. Pickering, R. W. Pinder, B. H. Henderson, K. W. Appel, and A. Prados (2012), Impact of lightning-NO on eastern United States photochemistry during the summer of 2006 as determined using the CMAQ model, *Atmos. Chem. Phys.*, *12*(4), 1737–1758, doi: 10.5194/acp-12-1737-2012.

Baker, M. B., H. J. Christian, and J. Latham (1995), A computational study of the relationships linking lightning frequency and other thundercloud parameters, *Q.J.R. Meteorol. Soc.*, *121*(527), 1525–1548, doi:10.1002/qj.49712152703.

Barth, M. C., J. Lee, A. Hodzic, G. Pfister, W. C. Skamarock, J. Worden, J. Wong, and D. Noone (2012), Thunderstorms and upper troposphere chemistry during the early stages of the 2006 North American Monsoon, *Atmos. Chem. Phys.*, *12*(22), 11,003–11,026, doi: 10.5194/acp-12-11003-2012.

Barthe, C., and J.-P. Pinty (2007), Simulation of a supercellular storm using a three-dimensional mesoscale model with an explicit lightning flash scheme, *J. Geophys. Res.*, *112*(D6).

Barthe, C., G. Molinié, and J.-P. Pinty (2005), Description and first results of an explicit electrical scheme in a 3D cloud resolving model, *Atmos. Res.*, *76*(1–4), 95–113, doi:http://dx.doi.org/10.1016/j.atmosres.2004.11.021.

Barthe, C., W. Deierling, and M. C. Barth (2010), Estimation of total lightning from various storm parameters: A cloud-resolving model study, *J. Geophys. Res.*, *115*(D24), doi:10.1029/2010JD014405.

Beer, R. (2006), TES on the Aura mission: scientific objectives, measurements, and analysis overview, *IEEE Trans. Geosci. Remote Sens.*, *44*(5), 1102–1105.

Boccippio, D. J. (2002), Lightning Scaling Relations Revisited, *J. Atmos. Sci.*, *59*(6), 1086–1104, doi:10.1175/1520-0469(2002)059$⟨$1086:LSRR$⟩$2.0.CO;2.

Boccippio, D. J., W. Koshak, R. Blakeslee, K. Driscoll, D. Mach, D. Buechler, W. Boeck, H. J. Christian, and S. J. Goodman (2000), The Optical Transient Detector (OTD): Instrument Characteristics and Cross-Sensor Validation, *J. Atmos. Oceanic Technol.*, *17*(4), 441–458, doi: 10.1175/1520-0426(2000)017⟨0441:TOTDOI⟩2.0.CO;2.

Boccippio, D. J., K. L. Cummins, H. J. Christian, and S. J. Goodman (2001), Combined Satellite- and Surface-Based Estimation of the Intracloud–Cloud-to-Ground Lightning Ratio over the Continental United States, *Mon. Wea. Rev.*, *129*(1), 108–122.

Boersma, K. F., H. J. Eskes, and E. J. Brinksma (2004), Error analysis for tropospheric NO2 retrieval from space, *J. Geophys. Res.*, *109*(D4), doi:10.1029/2003JD003962.

Borucki, W. J., and W. L. Chameides (1984), Lightning: Estimates of the rates of energy dissipation and nitrogen fixation, *Rev. Geophys.*, *22*(4), 363–372, doi:10.1029/RG022i004p00363.

Bouarar, I., et al. (2011), Emission sources contributing to tropospheric ozone over Equatorial Africa during the summer monsoon, *Atmos. Chem. Phys.*, *11*(24), 13,395–13,419, doi:10.5194/acp-11-13395-2011.

Bovensmann, H., J. P. Burrows, M. Buchwitz, J. Frerick, S. Noël, V. V. Rozanov, K. V. Chance, and A. P. H. Goede (1999), SCIAMACHY: Mission Objectives and Measurement Modes, *J. Atmos. Sci.*, *56*(2), 127–150, doi:10.1175/1520-0469(1999)056$⟨$0127:SMOAMM$⟩$2.0.CO;2.

Brown, D., J. Worden, and D. Noone (2008), Comparison of atmospheric hydrology over convective continental regions using water vapor isotope measurements from space, *J. Geophys. Res.*, *113*(D15), doi:10.1029/2007JD009676.

Burrows, J. P., E. Hlzle, A. P. H. Goede, H. Visser, and W. Fricke (1995), SCIAMACHY–scanning imaging absorption spectrometer for atmospheric chartography, *Acta Astronautica*, *35*(7), 445–451.

Chen, F., and J. Dudhia (2001), Coupling an Advanced Land Surface–Hydrology Model with the Penn State–NCAR MM5 Modeling System. Part II: Preliminary Model Validation, *Mon. Wea. Rev.*, *129*(4), 587–604, doi:10.1175/1520-0493(2001)129$⟨$0587:CAALSH$⟩$2.0.CO;2.

Choi, Y., Y. Wang, T. Zeng, R. V. Martin, T. P. Kurosu, and K. Chance (2005), Evidence of lightning NOx and convective transport of pollutants in satellite observations over North America, *Geophys. Res. Lett.*, *32*(2), L02,805, doi:10.1029/2004GL021436.

Choi, Y., J. Kim, A. Eldering, G. Osterman, Y. L. Yung, Y. Gu, and K. N. Liou (2009), Lightning and anthropogenic NOx sources over the United States and the western North Atlantic Ocean: Impact on OLR and radiative effects, *Geophys. Res. Lett.*, *36*(17).

Chou, M.-D., M. J. Suarez, C.-H. Ho, M. M.-H. Yan, and K.-T. Lee (1998), Parameterizations for Cloud Overlapping and Shortwave Single-Scattering Properties for Use in General Circulation and Cloud Ensemble Models, *J. Climate*, *11*(2), 202–214, doi:10.1175/1520-0442(1998)011$⟨$0202:PFCOAS$⟩$2.0.CO;2.

Christian, H. J., et al. (2003), Global frequency and distribution of lightning as observed from space by the Optical Transient Detector, *J. Geophys. Res. Atmos.*, *108*(D1), 4005, doi:10.1029/2002JD002347.

Cooper, O. R., et al. (2006), Large upper tropospheric ozone enhancements above midlatitude North America during summer: In situ evidence from the IONS and MOZAIC ozone measurement network, *J. Geophys. Res.*, *111*(D24).

Cooper, O. R., et al. (2007), Evidence for a recurring eastern North America upper tropospheric ozone maximum during summer, *J. Geophys. Res.*, *112*(D23).

Cooper, O. R., et al. (2009), Summertime buildup and decay of lightning NOx and aged thunderstorm outflow above North America, *J. Geophys. Res.*, *114*(D1).

Cristofanelli, P., et al. (2013), Influence of biomass burning and anthropogenic emissions on ozone, carbon monoxide and black carbon at the Mt. Cimone GAW-WMO global station (Italy, 2165 m a.s.l.), *Atmos. Chem. Phys.*, *13*(1), 15–30, doi:10.5194/acp-13-15-2013.

Cummings, K. A., T. L. Huntemann, K. E. Pickering, M. C. Barth, W. C. Skamarock, H. Höller, H. D. Betz, A. Volz-Thomas, and H. Schlager (2013), Cloud-resolving chemistry simulation of a Hector thunderstorm, *Atmos. Chem. Phys.*, *13*(5), 2757–2777, doi:10.5194/acp-13-2757-2013.

Cummins, K., and M. Murphy (2009), An Overview of Lightning Locating Systems: History, Techniques, and Data Uses, With an In-Depth Look at the U.S. NLDN, *IEEE Trans. Electromagn. Compat.*, *51*(3), 499 –518, doi:10.1109/TEMC.2009.2023450.

De Smedt, I., J. F. Müller, T. Stavrakou, R. van der A, H. Eskes, and M. Van Roozendael (2008), Twelve years of global observations of formaldehyde in the troposphere using GOME and SCIAMACHY sensors, *Atmos. Chem. Phys.*, *8*(16), 4947–4963, doi:10.5194/acp-8-4947-2008.

De Smedt, I., T. Stavrakou, J. F. Mller, R. J. van der A, and M. Van Roozendael (2010), Trend detection in satellite observations of formaldehyde tropospheric columns, *Geophys. Res. Lett.*, *37*(18), doi:10.1029/2010GL044245.

DeCaria, A. J., K. E. Pickering, G. L. Stenchikov, J. R. Scala, J. L. Stith, J. E. Dye, B. A. Ridley, and P. Laroche (2000), A cloud-scale model study of lightning-generated NO x in an individual thunderstorm during STERAO-A, *J. Geophys. Res.*, *105*(D9), 11,601–11,616.

DeCaria, A. J., K. E. Pickering, G. L. Stenchikov, and L. E. Ott (2005), Lightning-generated NOX and its impact on tropospheric ozone production: A three-dimensional modeling study of a Stratosphere-Troposphere Experiment: Radiation, Aerosols and Ozone (STERAO-A) thunderstorm, *J. Geophys. Res.*, *110*(D14).

Deierling, W., and W. A. Petersen (2008), Total lightning activity as an indicator of updraft characteristics, *J. Geophys. Res.*, *113*(D16), doi:10.1029/2007JD009598.

Dickerson, R. R., et al. (1987), Thunderstorms: An Important Mechanism in the Transport of Air Pollutants, *Science*, *235*(4787), 460–465.

Dufour, G., F. Wittrock, M. Camredon, M. Beekmann, A. Richter, B. Aumont, and J. P. Burrows (2009), SCIAMACHY formaldehyde observations: constraint for isoprene emission estimates over Europe?, *Atmos. Chem. Phys.*, *9*(5), 1647–1664, doi:10.5194/acp-9-1647-2009.

Emmons, L. K., et al. (2010), Description and evaluation of the Model for Ozone and Related chemical Tracers, version 4 (MOZART-4), *Geosci. Model Dev.*, *3*(1), 43–67.

EPA (2012), *40 CFR 51.100(s)*, Code of Federal Regulations.

Futyan, J. M., and A. D. Del Genio (2007), Relationships between lightning and properties of convective cloud clusters, *Geophys. Res. Lett.*, *34*(15).

Gauss, M., et al. (2006), Radiative forcing since preindustrial times due to ozone change in the troposphere and the lower stratosphere, *Atmos. Chem. Phys.*, *6*(3), 575–599, doi:10.5194/acp-6-575-2006.

Grell, G. A. (1993), Prognostic Evaluation of Assumptions Used by Cumulus Parameterizations, *Mon. Wea. Rev.*, *121*(3), 764–787.

Grell, G. A., and D. Devenyi (2002), A generalized approach to parameterizing convection combining ensemble and data assimilation techniques, *Geophys. Res. Lett.*, *29*(14).

Grell, G. A., S. E. Peckham, R. Schmitz, S. A. McKeen, G. Frost, W. C. Skamarock, and B. Eder (2005), Fully coupled "online" chemistry within the WRF model, *Atmos. Environ.*, *39*(37), 6957–6975.

Guenther, A., T. Karl, P. Harley, C. Wiedinmyer, P. I. Palmer, and C. Geron (2006), Estimates of global terrestrial isoprene emissions using MEGAN (Model of Emissions of Gases and Aerosols from Nature), *Atmos. Chem. Phys.*, *6*(11), 3181–3210.

Hansen, A. E., H. E. Fuelberg, and K. E. Pickering (2010), Vertical distributions of lightning sources and flashes over Kennedy Space Center, Florida, *J. Geophys. Res.*, *115*(D14), doi:10.1029/2009JD013143.

Hansen, A. E., H. E. Fuelberg, K. E. Pickering, S. E. Peckham, and R. E. Hart (2012), Lightning NOx Parameterization for WRF-Chem At the Regional Scale, in *92nd Amer. Meteor. Soc. Annual Meeting*, New Orleans, Louisiana.

Hauglustaine, D., et al. (2001), On the Role of Lightning NOx in the Formation of Tropospheric Ozone Plumes: A Global Model Perspective, *J. Atmos. Chem.*, *38*(3), 277–294–294.

Hegarty, J., H. Mao, and R. Talbot (2010), Winter- and summertime continental influences on tropospheric O3 and CO observed by TES over the western North Atlantic Ocean, *Atmos. Chem. Phys.*, *10*(8), 3723–3741, doi:10.5194/acp-10-3723-2010.

Hegglin, M. I., C. D. Boone, G. L. Manney, and K. A. Walker (2009), A global view of the extratropical tropopause transition layer from Atmospheric Chemistry Experiment Fourier Transform Spectrometer O3, H2O, and CO, *J. Geophys. Res. Atmos.*, *114*(D7), D00B11, doi:10.1029/2008JD009984.

Ho, S.-P., D. P. Edwards, J. C. Gille, M. Luo, G. B. Osterman, S. S. Kulawik, and H. Worden (2009), A global comparison of carbon monoxide profiles and column amounts from Tropospheric Emission Spectrometer (TES) and Measurements of Pollution in the Troposphere (MOPITT), *J. Geophys. Res.*, *114*(D21).

Hong, S.-Y., Y. Noh, and J. Dudhia (2006), A New Vertical Diffusion Package with an Explicit Treatment of Entrainment Processes, *Mon. Wea. Rev.*, *134*(9), 2318–2341.

Hudman, R. C., et al. (2007), Surface and lightning sources of nitrogen oxides over the United States: Magnitudes, chemical evolution, and outflow, *J. Geophys. Res.*, *112*(D12).

Janjić, Z. I. (1994), The Step-Mountain Eta Coordinate Model: Further Developments of the Convection, Viscous Sublayer, and Turbulence Closure Schemes, *Mon. Wea. Rev.*, *122*(5), 927–945, doi:10.1175/1520-0493(1994)122⟨0927:TSMECM⟩2.0.CO;2.

Jayaratne, E. R., and C. P. R. Saunders (1985), Thunderstorm electrification: The effect of cloud droplets, *J. Geophys. Res. Atmos.*, *90*(D7), 13,063–13,066, doi:10.1029/JD090iD07p13063.

Jourdain, L., S. S. Kulawik, H. M. Worden, K. E. Pickering, J. Worden, and A. M. Thompson (2010), Lightning NOx emissions over the USA constrained by TES ozone observations and the GEOS-Chem model, *Atmos. Chem. Phys.*, *10*(1), 107–119.

Justice, C. O., et al. (2002), The MODIS fire products, *Remote Sens. Environ.*, *83*(1–2), 244–262, doi:http://dx.doi.org/10.1016/S0034-4257(02)00076-7.

Kar, J., et al. (2004), Evidence of vertical transport of carbon monoxide from Measurements of Pollution in the Troposphere (MOPITT), *Geophys. Res. Lett.*, *31*(23), L23,105, doi:10.1029/2004GL021128.

Kiehl, J. T., T. L. Schneider, R. W. Portmann, and S. Solomon (1999), Climate forcing due to tropospheric and stratospheric ozone, *J. Geophys. Res. Atmos.*, *104*(D24), 31,239–31,254, doi:10.1029/1999JD900991.

Kim, S. W., et al. (2009), NO2 columns in the western United States observed from space and simulated by a regional chemistry model and their implications for NOx emissions, *J. Geophys. Res. Atmos.*, *114*(D11), D11,301, doi:10.1029/2008JD011343.

Kim, S. W., et al. (2011), Evaluations of NOx and highly reactive VOC emission inventories in Texas and their implications for ozone plume simulations during the Texas Air Quality Study 2006, *Atmos. Chem. Phys.*, *11*(22), 11,361–11,386, doi:10.5194/acp-11-11361-2011.

Kleinman, L. I., P. H. Daum, J. H. Lee, Y.-N. Lee, L. J. Nunnermacker, S. R. Springston, L. Newman, J. Weinstein-Lloyd, and S. Sillman (1997), Dependence of ozone production on NO and hydrocarbons in the troposphere, *Geophys. Res. Lett.*, *24*(18), 2299–2302, doi:10.1029/97GL02279.

Kleinman, L. I., P. H. Daum, Y.-N. Lee, L. J. Nunnermacker, S. R. Springston, J. Weinstein-Lloyd, and J. Rudolph (2001), Sensitivity of ozone production rate to ozone precursors, *Geophys. Res. Lett.*, *28*(15), 2903–2906, doi:10.1029/2000GL012597.

Konopka, P., J.-U. Grooß, G. Günther, F. Ploeger, R. Pommrich, R. Müller, and N. Livesey (2010), Annual cycle of ozone at and above the tropical tropopause: observations versus simulations with the Chemical Lagrangian Model of the Stratosphere (CLaMS), *Atmos. Chem. Phys.*, *10*(1), 121–132, doi:10.5194/acp-10-121-2010.

Lacis, A. A., D. J. Wuebbles, and J. A. Logan (1990), Radiative forcing of climate by changes in the vertical distribution of ozone, *J. Geophys. Res. Atmos.*, *95*(D7), 9971–9981, doi:10.1029/JD095iD07p09971.

Lamarque, J. F., G. P. Brasseur, P. G. Hess, and J. F. Müller (1996), Three-dimensional study of the relative contributions of the different nitrogen sources in the troposphere, *J. Geophys. Res. Atmos.*, *101*(D17), 22,955–22,968, doi:10.1029/96JD02160.

Lamarque, J. F., P. Hess, L. Emmons, L. Buja, W. Washington, and C. Granier (2005), Tropospheric ozone evolution between 1890 and 1990, *J. Geophys. Res.*, *110*(D8).

Lamarque, J. F., et al. (2010), Historical (1850–2000) gridded anthropogenic and biomass burning emissions of reactive gases and aerosols: methodology and application, *Atmos. Chem. Phys.*, *10*(15), 7017–7039, doi:10.5194/acp-10-7017-2010.

Lamarque, J. F., et al. (2012), CAM-chem: description and evaluation of interactive atmospheric chemistry in the Community Earth System Model, *Geosci. Model Dev.*, *5*(2), 369–411, doi:10.5194/gmd-5-369-2012.

Lambert, J.-C., et al. (2004), Geophysical Validation of SCIAMACHY NO_2 vertical columns: overview of early 2004 results, in *Proceedings of the Second Workshop on the Atmospheric Chemistry Validation of ENVISAT (ACVE-2)*, ESC01JL2, ESA-ESRIN, Frascati, Italy.

Li, Q., D. J. Jacob, R. Park, Y. Wang, C. L. Heald, R. Hudman, R. M. Yantosca, R. V. Martin, and M. Evans (2005), North American pollution outflow and the trapping of convectively lifted pollution by upper-level anticyclone, *J. Geophys. Res.*, *110*(D10).

Lin, Y.-L., R. D. Farley, and H. D. Orville (1983), Bulk Parameterization of the Snow Field in a Cloud Model, *J. Climate Appl. Meteor.*, *22*(6), 1065–1092, doi:10.1175/1520-0450(1983)022⟨1065:BPOTSF⟩2.0.CO;2.

Liu, C., and S. Heckman (2011), Using total lightning data in severe storm prediction: Global case study analysis from north America, Brazil and Australia, in *Lightning Protection (XI SIPDA), 2011 International Symposium on*, pp. 20–24.

Logan, J. A., I. Megretskaia, R. Nassar, L. T. Murray, L. Zhang, K. W. Bowman, H. M. Worden, and M. Luo (2008), Effects of the 2006 El Niño on tropospheric composition as revealed by data from the Tropospheric Emission Spectrometer (TES), *Geophys. Res. Lett.*, *35*(3), L03,816, doi:10.1029/2007GL031698.

Lopez, J. P., M. Luo, L. E. Christensen, M. Loewenstein, H. Jost, C. R. Webster, and G. Osterman (2008), TES carbon monoxide validation during two AVE campaigns using the Argus and ALIAS instruments on NASA's WB-57F, *J. Geophys. Res. Atmos.*, *113*(D16), D16S47, doi:10.1029/2007JD008811.

Luo, M., et al. (2007a), Comparison of carbon monoxide measurements by TES and MOPITT: Influence of a priori data and instrument characteristics on nadir atmospheric species retrievals, *J. Geophys. Res. Atmos.*, *112*(D9), doi:10.1029/2006JD007663.

Luo, M., et al. (2007b), TES carbon monoxide validation with DACOM aircraft measurements during INTEX-B 2006, *J. Geophys. Res.*, *112*(D24), D24S48, doi:10.1029/2007JD008803.

MacGorman, D. R., and W. D. Rust (1998), *The electrical nature of storms*, Oxford University Press, Incorporated.

Madronich, S. (1987), Photodissociation in the atmosphere: 1. Actinic flux and the effects of ground reflections and clouds, *J. Geophys. Res. Atmos.*, *92*(D8), 9740–9752, doi:10.1029/JD092iD08p09740.

Mansell, E. R., D. R. MacGorman, C. L. Ziegler, and J. M. Straka (2002), Simulated three-dimensional branched lightning in a numerical thunderstorm model, *J. Geophys. Res.*, *107*(D9), doi:10.1029/2000JD000244.

Marais, E. A., et al. (2012), Isoprene emissions in Africa inferred from OMI observations of formaldehyde columns, *Atmos. Chem. Phys.*, *12*(14), 6219–6235, doi:10.5194/acp-12-6219-2012.

Martini, M., D. J. Allen, K. E. Pickering, G. L. Stenchikov, A. Richter, E. J. Hyer, and C. P. Loughner (2011), The impact of North American anthropogenic emissions and lightning on long-range transport of trace gases and their export from the continent during summers 2002 and 2004, *J. Geophys. Res.*, *116*(D7), doi:10.1029/2010JD014305.

McMillan, W. W., et al. (2010), An observational and modeling strategy to investigate the impact of remote sources on local air quality: A Houston, Texas, case study from the Second Texas Air Quality Study (TexAQS II), *J. Geophys. Res.*, *115*(D1), doi:10.1029/2009JD011973.

Michalon, N., A. Nassif, T. Saouri, J. F. Royer, and C. A. Pontikis (1999), Contribution to the climatological study of lightning, *Geophys. Res. Lett.*, *26*(20), 3097–3100.

Millet, D. B., D. J. Jacob, K. F. Boersma, T.-M. Fu, T. P. Kurosu, K. Chance, C. L. Heald, and A. Guenther (2008), Spatial distribution of isoprene emissions from North America derived from formaldehyde column measurements by the OMI satellite sensor, *J. Geophys. Res. Atmos.*, *113*(D2), D02,307, doi:10.1029/2007JD008950.

Mlawer, E. J., S. J. Taubman, P. D. Brown, M. J. Iacono, and S. A. Clough (1997), Radiative transfer for inhomogeneous atmospheres: RRTM, a validated correlated-k model for the longwave, *J. Geophys. Res. Atmos.*, *102*(D14), 16,663–16,682, doi:10.1029/97JD00237.

Müller, J.-F. (1992), Geographical distribution and seasonal variation of surface emissions and deposition velocities of atmospheric trace gases, *J. Geophys. Res. Atmos.*, *97*(D4), 3787–3804, doi:10.1029/91JD02757.

Nassar, R., et al. (2008), Validation of Tropospheric Emission Spectrometer (TES) nadir ozone profiles using ozonesonde measurements, *J. Geophys. Res.*, *113*(D15).

Niemeyer, L., L. Pietronero, and H. J. Wiesmann (1984), Fractal Dimension of Dielectric Breakdown, *Phys. Rev. Lett.*, *52*(12), 1033–1036.

Oltmans, S. J., et al. (2006), Long-term changes in tropospheric ozone, *Atmos. Environ.*, *40*(17), 3156–3173.

Orville, R. E., G. R. Huffines, W. R. Burrows, R. L. Holle, and K. L. Cummins (2002), The North American Lightning Detection Network (NALDN)—First Results: 1998–2000, *Mon. Wea. Rev.*, *130*(8), 2098–2109.

Orville, R. E., G. R. Huffines, W. R. Burrows, and K. L. Cummins (2010), The North American Lightning Detection Network (NALDN)—Analysis of Flash Data: 2001–09, *Mon. Wea. Rev.*, *139*(5), 1305–1322, doi:10.1175/2010MWR3452.1.

Ott, L. E., K. E. Pickering, G. L. Stenchikov, H. Huntrieser, and U. Schumann (2007), Effects of lightning NOx production during the 21 July European Lightning Nitrogen Oxides Project storm studied with a three-dimensional cloud-scale chemical transport model, *J. Geophys. Res.*, *112*(D5).

Ott, L. E., K. E. Pickering, G. L. Stenchikov, D. J. Allen, A. J. DeCaria, B. Ridley, R.-F. Lin, S. Lang, and W.-K. Tao (2010), Production of lightning NOx and its vertical distribution calculated from three-dimensional cloud-scale chemical transport model simulations, *J. Geophys. Res.*, *115*(D4).

Palmer, P. I., et al. (2001), Air mass factor formulation for spectroscopic measurements from satellites: Application to formaldehyde retrievals from the Global Ozone Monitoring Experiment, *J. Geophys. Res. Atmos.*, *106*(D13), 14,539–14,550, doi:10.1029/2000JD900772.

Palmer, P. I., D. J. Jacob, A. M. Fiore, R. V. Martin, K. Chance, and T. P. Kurosu (2003), Mapping isoprene emissions over North America using formaldehyde column observations from space, *J. Geophys. Res. Atmos.*, *108*(D6), 4180, doi:10.1029/2002JD002153.

Palmer, P. I., et al. (2006), Quantifying the seasonal and interannual variability of North American isoprene emissions using satellite observations of the formaldehyde column, *J. Geophys. Res. Atmos.*, *111*(D12), D12,315, doi:10.1029/2005JD006689.

Pan, L. L., J. C. Wei, D. E. Kinnison, R. R. Garcia, D. J. Wuebbles, and G. P. Brasseur (2007), A set of diagnostics for evaluating chemistry-climate models in the extratropical tropopause region, *J. Geophys. Res.*, *112*(D9).

Park, M., W. J. Randel, A. Gettelman, S. T. Massie, and J. H. Jiang (2007), Transport above the Asian summer monsoon anticyclone inferred from Aura Microwave Limb Sounder tracers, *J. Geophys. Res. Atmos.*, *112*(D16), D16,309, doi:10.1029/2006JD008294.

Petersen, W. A., H. J. Christian, and S. A. Rutledge (2005), TRMM observations of the global relationship between ice water content and lightning, *Geophys. Res. Lett.*, *32*(14), doi:10.1029/2005GL023236.

Pickering, K. E., Y. Wang, W.-K. Tao, C. Price, and J.-F. Mller (1998), Vertical distributions of lightning NO x for use in regional and global chemical transport models, *J. Geophys. Res.*, *103*(D23), 31,203–31,216.

Price, C., and D. Rind (1992), A Simple Lightning Parameterization for Calculating Global Lightning Distributions, *J. Geophys. Res.*, *97*(D9), 9919–9933.

Price, C., and D. Rind (1993), What determines the cloud-to-ground lightning fraction in thunderstorms?, *Geophys. Res. Lett.*, *20*(6), 463–466, doi:10.1029/93GL00226.

Price, C., and D. Rind (1994), Modeling Global Lightning Distributions in a General Circulation Model, *Mon. Wea. Rev.*, *122*(8), 1930–1939.

Price, C., J. Penner, and M. Prather (1997), NOx from lightning 1. Global distribution based on lightning physics, *J. Geophys. Res.*, *102*(D5), 5929–5941, doi:10.1029/96JD03504.

Reynolds, S. E., M. Brook, and M. F. Gourley (1957), Thunderstorm chare separation, *J. Meteor.*, *14*(5), 426–436, doi:10.1175/1520-0469(1957)014⟨0426:TCS⟩2.0.CO;2.

Ridley, B., et al. (2004), Florida thunderstorms: A faucet of reactive nitrogen to the upper troposphere, *J. Geophys. Res.*, *109*(D17).

Risi, C., S. Bony, F. Vimeux, C. Frankenberg, D. Noone, and J. Worden (2010), Understanding the Sahelian water budget through the isotopic composition of water vapor and precipitation, *J. Geophys. Res.*, *115*(D24), doi:10.1029/2010JD014690.

Rossow, W., and R. Schiffler (1991), ISCCP cloud data products, *Bull. Amer. Meteorol. Soc.*, *71*, 2–20.

Sandu, A., and R. Sander (2006), Technical note: Simulating chemical systems in Fortran90 and Matlab with the Kinetic PreProcessor KPP-2.1, *Atmos. Chem. Phys.*, *6*(1), 187–195.

Saunders, C. P. R., H. Bax-norman, C. Emersic, E. E. Avila, and N. E. Castellano (2006), Laboratory studies of the effect of cloud conditions on graupel/crystal charge transfer in thunderstorm electrification, *Q.J.R. Meteorol. Soc.*, *132*(621), 2653–2673, doi:10.1256/qj.05.218.

Schumann, U., and H. Huntrieser (2007), The global lightning-induced nitrogen oxides source, *Atmos. Chem. Phys.*, *7*(14), 3823–3907, doi:10.5194/acp-7-3823-2007.

Skamarock, W. C. (2006), Positive-Definite and Monotonic Limiters for Unrestricted-Time-Step Transport Schemes, *Mon. Wea. Rev.*, *134*(8), 2241–2250.

Skamarock, W. C., J. E. Dye, E. Defer, M. C. Barth, J. L. Stith, B. A. Ridley, and K. Baumann (2003), Observational- and modeling-based budget of lightning-produced NOx in a continental thunderstorm, *J. Geophys. Res.*, *108*(D10).

Skamarock, W. C., J. B. Klemp, J. Dudhia, D. O. Gill, D. M. Barker, M. G. Duda, X.-Y. Huang, W. Wang, and J. G. Powers (2008), *A description of the Advanced Research WRF Version 3*, NCAR Tech. Note, NCAR/TN-475+STR.

Skamarock, W. C., J. B. Klemp, M. G. Duda, L. D. Fowler, S.-H. Park, and T. D. Ringler (2012), A Multiscale Nonhydrostatic Atmospheric Model Using Centroidal Voronoi Tesselations and C-Grid Staggering, *Mon. Wea. Rev.*, *140*(9), 3090–3105, doi:10.1175/MWR-D-11-00215.1.

Smit, H. G. J., et al. (2007), Assessment of the performance of ECC-ozonesondes under quasi-flight conditions in the environmental simulation chamber: Insights from the Juelich Ozone Sonde Intercomparison Experiment (JOSIE), *J. Geophys. Res.*, *112*(D19).

Smith, P. L., C. G. Myers, and H. D. Orville (1975), Radar Reflectivity Factor Calculations in Numerical Cloud Models Using Bulk Parameterization of Precipitation, *J. Appl. Meteor.*, *14*(6), 1156–1165, doi:10.1175/1520-0450(1975)014⟨1156:RRFCIN⟩2.0.CO;2.

Stark, M. S., J. T. H. Harrison, and C. Anastasi (1996), Formation of nitrogen oxides by electrical discharges and implications for atmospheric lightning, *J. Geophys. Res. Atmos.*, *101*(D3), 6963–6969, doi:10.1029/95JD03008.

Stevenson, D. S., C. E. Johnson, W. J. Collins, R. G. Derwent, K. P. Shine, and J. M. Edwards (1998), Evolution of tropospheric ozone radiative forcing, *Geophys. Res. Lett.*, *25*(20), 3819–3822, doi:10.1029/1998GL900037.

Stevenson, D. S., et al. (2006), Multimodel ensemble simulations of present-day and near-future tropospheric ozone, *J. Geophys. Res.*, *111*(D8).

Stith, J., J. Dye, B. Ridley, P. Laroche, E. Defer, K. Baumann, G. Hübler, R. Zerr, and M. Venticinque (1999), NO signatures from lightning flashes, *J. Geophys. Res. Atmos.*, *104*(D13), 16,081–16,089, doi:10.1029/1999JD900174.

Stockwell, W. R., P. Middleton, J. S. Chang, and X. Tang (1990), The Second Generation Regional Acid Deposition Model Chemical Mechanism for Regional Air Quality Modeling, *J. Geophys. Res.*, *95*(D10), 16,343–16,367.

Stolzenburg, M., W. D. Rust, and T. C. Marshall (1998), Electrical structure in thunderstorm convective regions: 3. Synthesis, *J. Geophys. Res. Atmos.*, *103*(D12), 14,097–14,108, doi:10.1029/97JD03545.

Tarasick, D. W., et al. (2007), Comparison of Canadian air quality forecast models with tropospheric ozone profile measurements above midlatitude North America during the IONS/ICARTT campaign: Evidence for stratospheric input, *J. Geophys. Res.*, *112*(D12).

Thompson, A. M., et al. (2007a), Intercontinental Chemical Transport Experiment Ozonesonde Network Study (IONS) 2004: 1. Summertime upper troposphere/lower stratosphere ozone over northeastern North America, *J. Geophys. Res.*, *112*(D12).

Thompson, A. M., et al. (2007b), Intercontinental Chemical Transport Experiment Ozonesonde Network Study (IONS) 2004: 2. Tropospheric ozone budgets and variability over northeastern North America, *J. Geophys. Res.*, *112*(D12).

Thompson, A. M., J. E. Yorks, S. K. Miller, J. C. Witte, K. M. Dougherty, G. A. Morris, D. Baumgardner, L. Ladino, and B. Rappenglück (2008a), Tropospheric ozone sources and wave activity over Mexico City and Houston during MILAGRO/Intercontinental Transport Experiment (INTEX-B) Ozonesonde Network Study, 2006 (IONS-06), *Atmos. Chem. Phys.*, *8*(17), 5113–5125.

Thompson, G., P. R. Field, R. M. Rasmussen, and W. D. Hall (2008b), Explicit Forecasts of Winter Precipitation Using an Improved Bulk Microphysics Scheme. Part II: Implementation of a New Snow Parameterization, *Mon. Wea. Rev.*, *136*(12), 5095–5115.

Tie, X., S. Madronich, S. Walters, R. Zhang, P. Rasch, and W. Collins (2003), Effect of clouds on photolysis and oxidants in the troposphere, *J. Geophys. Res.*, *108*(D20).

Tost, H., P. Jöckel, and J. Lelieveld (2007), Lightning and convection parameterisations – uncertainties in global modelling, *Atmos. Chem. Phys.*, *7*(17), 4553–4568.

Uman, M. A., and E. P. Krider (1989), Natural and Artificially Initiated Lightning, *Science*, *246*(4929), 457–464, doi:10.1126/science.246.4929.457.

Ushio, T., S. J. Heckman, D. J. Boccippio, H. J. Christian, and Z.-I. Kawasaki (2001), A survey of thunderstorm flash rates compared to cloud top height using TRMM satellite data, *J. Geophys. Res.*, *106*(D20), 24,089–24,095, doi:10.1029/2001JD900233.

van der A, R. J., H. J. Eskes, M. Van Roozendael, I. De Smedt, N. Blond, F. Boersma, A. Weiss, and J. C. A. van Peet (2010), Tropospheric NO_2, *Algorithm Document TEM/AD1/001*, TEMIS.

Vonnegut, B. (1963), Some facts and speculation concerning the origin and role of thunderstorm eletricity, *Meteor. Monogr.*, (27), 224–241.

Voulgarakis, A., P. J. Telford, A. M. Aghedo, P. Braesicke, G. Faluvegi, N. L. Abraham, K. W. Bowman, J. A. Pyle, and D. T. Shindell (2011), Global multi-year O3-CO correlation patterns from models and TES satellite observations, *Atmos. Chem. Phys.*, *11*(12), 5819–5838, doi:10.5194/acp-11-5819-2011.

Wang, H., W. C. Skamarock, and G. Feingold (2009), Evaluation of Scalar Advection Schemes in the Advanced Research WRF Model Using Large-Eddy Simulations of Aerosol–Cloud Interactions, *Mon. Wea. Rev.*, *137*(8), 2547–2558, doi:10.1175/2009MWR2820.1.

Wang, Y., A. W. DeSilva, G. C. Goldenbaum, and R. R. Dickerson (1998), Nitric oxide production by simulated lightning: Dependence on current, energy, and pressure, *J. Geophys. Res. Atmos.*, *103*(D15), 19,149–19,159, doi:10.1029/98JD01356.

Wang, Y., Y. Zhang, J. Hao, and M. Luo (2011), Seasonal and spatial variability of surface ozone over China: contributions from background and domestic pollution, *Atmos. Chem. Phys.*, *11*(7), 3511–3525, doi:10.5194/acp-11-3511-2011.

Weinstock, E. M., et al. (2007), Quantifying the impact of the North American monsoon and deep midlatitude convection on the subtropical lowermost stratosphere using in situ measurements, *J. Geophys. Res.*, *112*(D18).

Wiesmann, H. J., and H. R. Zeller (1986), A fractal model of dielectric breakdown and prebreakdown in solid dielectrics, *J. Appl. Phys.*, *60*(5), 1770–1773, doi:10.1063/1.337219.

Williams, E. R. (1985), Large-Scale Charge Separation in Thunderclouds, *J. Geophys. Res.*, *90*(D4), 6013–6025.

Williams, E. R. (1989), The Tripole Structure of Thunderstorms, *J. Geophys. Res.*, *94*(D11), 13,151–13,167, doi:10.1029/JD094iD11p13151.

Wilson, C. T. R. (1916), On Some Determinations of the Sign and Magnitude of Electric Discharges in Lightning Flashes, *Proc. Roy. Soc. London*, *92*, 555–574, doi:10.1098/rspa.1916.0040.

Wong, J., M. C. Barth, and D. Noone (2013), Evaluating a lightning parameterization based on cloud-top height for mesoscale numerical model simulations, *Geosci. Model Dev.*, *6*(2), 429–443, doi:10.5194/gmd-6-429-2013.

Worden, J., et al. (2009), Observed vertical distribution of tropospheric ozone during the Asian summertime monsoon, *J. Geophys. Res.*, *114*(D13), D13,304, doi:10.1029/2008JD010560.

Yoshida, S., T. Morimoto, T. Ushio, and Z. Kawasaki (2009), A fifth-power relationship for lightning activity from Tropical Rainfall Measuring Mission satellite observations, *J. Geophys. Res.*, *114*(D9), doi:10.1029/2008JD010370.

Zeldovich, I. A. B. (1966), *Physics of Shock Waves and High-temperature Hydrodynamic Phenomena*, Dover Publications, Incorporated.

Zhang, L., et al. (2006), Ozone-CO correlations determined by the TES satellite instrument in continental outflow regions, *Geophys. Res. Lett.*, *33*(18), L18,804, doi:10.1029/2006GL026399.

Zhang, L., D. J. Jacob, X. Liu, J. A. Logan, K. Chance, A. Eldering, and B. R. Bojkov (2010), Intercomparison methods for satellite measurements of atmospheric composition: application to tropospheric ozone from TES and OMI, *Atmos. Chem. Phys.*, *10*(10), 4725–4739, doi:10.5194/acp-10-4725-2010.

Zhang, X., J. Helsdon, John H., and R. D. Farley (2003), Numerical modeling of lightning-produced NOx using an explicit lightning scheme: 1. Two-dimensional simulation as a "proof of concept", *J. Geophys. Res.*, *108*(D18).

Zhao, C., Y. Wang, Y. Choi, and T. Zeng (2009), Summertime impact of convective transport and lightning NOx production over North America: modeling dependence on meteorological simulations, *Atmos. Chem. Phys.*, *9*(13), 4315–4327, doi:10.5194/acp-9-4315-2009.

Appendix A

Acronyms and Abbreviations

AHPS	Advanced Hydrological Prediction Service
AMF	air mass factor
ANOx	Anthropogenic nitrogen oxides
BVOCs	biogenic volatile organic compounds
CAPE	convective available potential energy
CCN	cloud condensation nuclei
CFCs	Chlorofluorocarbons
CLDN	Canadian Lightning Detection Network
CONUS	Contiguous United States
CTM	chemical-transport model
DE	detection efficiency
DF	direction finding (lightning detection)
DFS	degrees of freedom of signal
DOAS	Differential Optical Absoption Spectroscopy
ECC	electrochemical concentration cell
ECMWF	European Centre for Medium-Range Weather Forecasts model
ENTLN	Earth Networks Total Lightning Network
ENVISAT	Environmental Satellite
EOS	Earth Observing System

EPA	Environmental Protection Agency
ERS-2	European Remote-Sensing satellite
ESRL	Earth System Research Laboratory
FLEXPART	a Lagrangian particle dispersion model
FTUV	fast Tropospheric Ultraviolet-Visible
GFS	Global Forecast System
GOME	Global Ozone Monitoring Experiment
HCFCs	Hydrochlorofluorocarbons
HFCs	Hydrofluorocarbons
IC:CG	Intro-cloud:Cloud-to-ground
IMPACT	Improved Accuracy through Combined Technology (lightning detection)
INTEX-B	Intercontinental Chemical Transport Experiment - phase B
IONS-06	INTEX-B Ozonesonde Network Study of 2006
IPCC	Intergovernmental Panel on Climate Change
ISCCP	International Satellite Cloud Climatology Project
IWP	ice water path
JPL	Jet Propulsion Laboratory
KNMI	Royal Netherlands Meteorological Institute
	(Koninklijk Nederlands Meteorologisch Instituut)
KPP	Kinetic Pre-processor
LAI	leaf area index
LIS	Lightning Imaging Sensor
LNB	level of neutral buoyancy
LNOx	Lightning-generated nitrogen oxides
LPATS	Lightning Position and Tracking System
MAP	maximum a posteriori
MEGAN	Model of Emissions of Gases and Aerosols from Nature

MOPITT	Measurements Of Pollution In The Troposphere
MPE	Multi-sensor Precipitation Estimator
NALDN	North American Lightning Detection Network
NAM	North American Monsoon
NASA	National Aeronautics and Space Administration
NCAR	National Center for Atmospheric Research
NCEP	National Center for Environmental Prediction
NDSC	Network for the Detection of Stratospheric Change
NEI	National Emission Inventory
NLDN	National Lightning Detection Network
NOAA	National Oceanic and Atmospheric Administration
NOx	nitrogen oxides ($\equiv NO+NO_2$)
NWS	National Weather Service
OMI	Ozone Monitoring Instrument satellite
OTD	Optical Transient Detector
PBL	planetary boundary layer
PCA	principal component analysis
PCEEA	parameterized canopy enviornmet emission activity
PM2.5	particulate matter < 2.5 microns in diameter
PPFD	photosynthetic photon flux density
PR92	*Price and Rind* (1992)
PR93	*Price and Rind* (1993)
PR94	*Price and Rind* (1994)
RADM2	second-generation Regional Acid Deposition Model
RFC	River Forecast Center
SCIAMACHY	SCanning Imaging Absorption SpectroMeter for Atmospheric CHartographY
TEMIS	Tropospheric Emission Monitoring Internet Service

TES	Tropospheric Emission Spectrometer
TOA	time-of-arrival
TRMM	Tropical Rainfall Measuring Mission
VCD	vertical column density
VOCs	volatile organic compounds
WLS	Weatherbug Lightning Sensor
WPS	WRF Preprocessing System
WRF	Weather Research and Forecasting model

Appendix B

WRF-Chem v3.4.1 Namelist

Option(s)	Value(s)	Comment
&time_control		
(start|end)_year	2006	
(start|end)_month	(07|08)	
(start|end)_day	(01–31)	end_day = start_day + 1
(start|end)_hour	06	Always start at 6 UTC
interval_seconds	21600	Boundary condition input intervals (6 hours)
history_interval	180	History output interval (3 hours)
frame_per_outfile	1	
restart	.true.	Only .false. for July 1
restart_interval	1440	Daily restart
&domains		
time_step	90 + 0/1	Time-step in seconds
e_we	180	West-east domain dimension
e_sn	120	South-north domain dimension
e_vert	51	Vertical domain dimension
dx,dy	36000	Grid size (m)
p_top_requested	1000	Model top pressure (Pa)
num_metgrid_levels	27	
num_metgrid_soil_levels	4	
grid_id	1	No nesting
eta_levels	1.0, 0.99381, ⋮ 0.00560, 0.0	51 non-uniform fixed vertical resolution
&physics		
mp_physics	8	"New" Thompson microphysics scheme
progn	0	No prognostic cloud droplet number
ra_lw_physics	1	Rapid Radiative Transfer Model (RRTM)
ra_sw_physics	2	Goddard two-stream shortwave scheme

radt	30	Minutes between radiative physics call
sf_sfclay_physics	1	Surface layer physics
sf_surface_physics	2	Noah Land Surface Model
bl_pbl_physics	1	Yonsei University (YSU) scheme
cu_physics	5	Grell-3D (G3) cumulus scheme
cudt	0	Call convective parameterization every time step
prec_acc_dt	180	Bucket for precipitation (min)
isfflx	1	Turn on sensible and latent surface heat flux
ifsnow	0	Turn off snow effect on optical depth
icloud	1	Turn on cloud
surface_input_source	1	WPS/geogrid default surface category
num_soil_layers	4	
sf_urban_physics	0	Turn off urban physics
maxiens	1	(not used?)
maxens, maxens2, maxens3	3, 3, 16	G3 ensemble dimensions
ensdim	144	G3 ensemble dimension
cu_rad_feedback	.true.	Cumulus radiative feedback
ishallow	1	Turn on shallow convection
cu_diag	1	Turn on cumulus diagnostics
&fdda		
grid_fdda	1	Turn on grid 4D data assimilation (GFDDA)
gfdda_inname	"wrffdda_d<domain>"	
gfdda_end_h	10000	End hour ("never")
gfdda_interval_m	360	Interval of GFDDA inputs
fgdt	0	Nudge every time step
if_no_pbl_nuding_(uv,t,q)	0,1,1	Only do nudging for wind in PBL.
(if,k)_zfac_uv	1,10	Limit nudging of wind to above level 10
if_zfac_(t|q)	0	
guv, gt	0.0024	Nudging coefficients (s^{-1})
gq	9.26e-5	Nudging coefficient (s^{-1})
if_ramping	1	Ramp down nudging at the end of period
dtramp_min	60.0	Ramp down time (min)
io_form_gfdda	2	NetCDF format for GFDDA data
&dynamics		
rk_ord	3	Runge-Kutta 3rd order
w_damping	1	Damping for vertical velocity
diff_opt	1	Evaluates 2nd order diffusion term on coordinate surfaces
km_opt	4	Horizontal Smagorinsky first order closure
base_temp	290	Base-state temperature (K)
zdamp	5000	Damping depth (m) from model top
damp_opt	3	Rayleigh damping
dampcoef	0.2	Rayleigh damping coefficient (s^{-1})
non_hydrostatic	.true.	

*_adv_opt	2	Positive definite and monotonic advection for moist, scalar, chem, and tracer
time_step_sound	4	Number of sound steps per time step
h_(mon|sca)_adv_order	5	Horizontal orders for momentum and scalar advections
v_(mon|sca)_adv_order	3	Vertical orders for advections
tracer_opt	4	8 twin tracers + 2 lightning tracers
&bdy_control		
spec_bdy_width	5	Number of rows for specified boundary value nudging
spec_zone	1	Specified zone
relax_zone	4	Relaxation zone
specified	.true.	Specified boundary condition
nested	.false.	
&chem		
kemit	19	Number of levels in emission files
chem_opt	101	RADM2-KPP option, no aerosol
bioemdt	1.5	Update time (min) for biogenic emissions
chemdt	1.5	Update time (min) for chemistry
io_style_emissions	1	Two 12-hr emission files
emiss_inpt_opt	1	Speciate emission for RADM2/SORGAM
emiss_opt	2	RADM2-speciated anthropogenic emission
chem_in_opt	0	Use chemistry from wrfinput_d*
phot_opt	3	FTUV photolysis (see Appendix D.1)
photdt	30	Update time (min) for photolysis
(gas|aer)_drydep_opt	1	Include dry deposition
bio_emiss_opt	3	MEGAN2 biogenic emission
(dust|dmsemis|seas)_opt	0	Turn off dust, DMS, and sea salt options
gas_(bc|ic)_opt	1	Use BC and IC for gas species
aer_(bc|ic)_opt	0	No BC and IC for aerosols
gaschem_onoff	1	Turn on gas-phase chemistry
(aer|cld)chem)_onoff	0	Turn off aerosol and cloud chemistry
wetscav_onoff	0	Turn off wet scavenging
vertmix_onoff	1	Turn on vertical mixing
chem_conv_tr	1	Turn on convective transport for chemical species
biomass_burn_opt	0	No biomass burning
aer_ra_feedback	0	No aerosol radiative feedback
have_bcs_chem	.true.	
lightning_opt	101	Cloud-parameterized PR92.
lightning_start_seconds	900	
lightning_time_step	90	In seconds, i.e. every time step
N_IC	350	Moles of NO per flash (independent of IC or CG)
flash_factor	1.0	Master flash rate tuning factor
passive_ltng	1	Emit passive LNO_x twin tracers
chem_diag	1	Produce tendency diagnostics for 8 species

Appendix C

User documentation for $\mathsf{LNO_x}$ in WRF-Chem 3.5

This is a short guide for using the lightning flash rate and lightning-generated nitrogen oxides ($\mathsf{LNO_x}$) parameterizations in WRF and WRF-Chem after version 3.5.0. Significant changes have been made since 3.4.1, primarily in refactoring the model to allow flash rate predictions without chemistry. Currently, only implementations for the *Price and Rind* (1992, hereafter PR92) schemes are released with modifications based on *Barth et al.* (2012) and *Wong et al.* (2013).

To turn on lightning flash rate parameterization in WRF, set the `physics` namelist option `lightning_option` to one of the following values:

lightning_option	**Description**
1†	PR92 based on maximum w, redistributes flashes within dBZ > 20
2†	PR92 based on 20 dBZ top, redistributes flashes within dBZ > 20
11*	PR92 based on level of neutral buoyancy from convective parameterization

† For convection-resolved resolutions with microphysics turned on for reflectivity calculations.

* For convection-parameterized resolution using either GD or G3 `cu_physics` options. Adjusted by areal ratio relative to `dx`=36 km (*Wong et al.*, 2013), intended for use at 10 < `dx` < 50 km.

Setting `lightning_option` will produce four new 2D arrays: `(ic|cg)_flash(count|rate)` with units number (per seconds), where `ic` and `cg` represent intra-cloud and cloud-to-ground respectively. Set the `physics` namelist option `iccg_method` to control the IC:CG ratio:

iccg_method	Description
0	Default method depending on `lightning_option` , currently all options use `iccg_method`=2 by default.
1	Constant everywhere, set with namelist options `iccg_prescribed_(num|den)`†, default is 0./1. (all CG).
2	Coarsely prescribed 1995–1999 NLDN/OTD climatology based on *Boccippio et al.* (2001).
3	Parameterization by *Price and Rind* (1993) based on cold-cloud depth.
4	Gridded input via arrays `iccg_in_(num|den)` from wrfinput for monthly mapped ratios. Points with 0/0 values use ratio defined by `iccg_prescribed_(num|den)`.

† This is a shorthand for "`iccg_prescribed_num` and `iccg_prescribed_den`." Similar notation is used throughout this guide when namelist options or arrays have long but similar names.

To emit $\mathsf{LNO_x}$, in the form of nitrogen oxide (NO), set the `chem` namelist option `lnox_opt` to one of the following values:

lnox_opt	Description
1	Combined IC+CG single-mode vertical distributions (*Ott et al.*, 2010). Outputs passive tracer array `lnox_total`.
2	Separate IC, CG distributions after *DeCaria et al.* (2000). Outputs two passive tracer arrays `lnox_(ic|cg)`.

Additional namelist settings are available for more detailed controls of the parameterizations:

Namelist option	**Description**
`&physics`	
`lightning_dt`	Time interval (seconds) for calling lightning parameterization. Default uses model time step.
`lightning_start_seconds`	Start time for calling lightning parameterization. Recommends at least 10 minutes for spin-up.
`flashrate_factor`	Factor to adjust the predicted number of flashes. Recommends 1.0 for `lightning_option`=11 between `dx`=10 and 50 km. Manual tuning recommended for all other options independently for each nest.
`cellcount_method`	Method for counting storm cells. Used by CRM options (`lightning_option`s=1,2). **!!** Note that this option used to take values 1, 2, and 3 in version 3.4.1. 0 = model determines method used. 1 = tile-wide, appropriate for large domains 2 = domain-wide, appropriate for single-storm domains
`cldtop_adjustment`	Adjustment from LNB in km. Used by `lightning_option` =11. Default is 0, but recommends −2 km.
`iccg_prescribed_(num|den)`	User prescribed numerator and denominator for IC:CG ratio. Used by `iccg_method`=1,4. Defaults are 0.0/1.0
`&chem`	
`N_(IC|CG)`	Moles of NO emitted per IC and CG flashes. For total LNO_x option (`lnox_opt`=1), a weighted average based on the calculated IC:CG ratio is used. Default is 500 moles. Recommends 300–500 moles.
`lnox_passive`	Set to `.true.` to emit passive tracers only.
`ltng_temp_(upper|lower)`	Temperatures (°C) of `upper` and `lower` peaks of LNO_x vertical distributions (used by `lnox_opt`=2).

Appendix D

WRF-Chem bug fixes

Numerous bugs in WRF-Chem surfaced recently and caused the model to crash or produce undesirable results. This appendix details the bugs discovered and their corresponding fixes.

D.1 Fast TUV

The fast Tropospheric Ultraviolet-Visible (fast TUV, or FTUV) photolysis scheme is a simplified version of the widely used TUV scheme by *Madronich* (1987). Details of FTUV parameterization of TUV can be found in *Tie et al.* (2003). Since the use of MOZART chemistry options triggers an alternative method for computing model top ozone column, this bug only concerns WRF-Chem simulations using non-MOZART chemistry options.

D.1.1 Bug description

To simulate the radiative transfer of the full atmosphere, model column ozone is supplemented with exo-model ozone column density, or "exocolden." This is done during the call to the subroutine `photo_inti` within `ftuv_init`. One of the intended functions of `photo_inti` is to add exocolden data every 2 km on top of the model top up to 50 km using reference data (`o3ref`). However, the model top input for this function has been hard-coded to 20 km regardless of the actual model top level height. The model set-up used in this study has a model top of 10 hPa, or ~ 30 km. Therefore, the effect height profile becomes $0, \ldots, 30, 22, 24, 26, \ldots, 48, 50$ km plus 2.9745×10^{16} molecules cm^{-2} above 50 km. Furthermore, before the calculation of slant column density, the total column ozone

is also scaled to a fixed value (265 DU). However, this value is grossly under-representing the standard ozone column for the United States, which has a recommended value of 349 DU instead (*S. Madronich*, personal communication, 2013). These bugs have two primary consequences[1] :

(1) Since ozone is typically highest between 20–30 km, two ozone maxima are introduced, one located outside the model physical levels. Because of an extra ozone maximum above model top, older simulations with a similar model top (30 km) may see significantly lower photolysis rates above 20 km.

(2) When calculating the slant column density, the logarithm of `o2col` (depends on `dz`) is calculated in the subroutine `schu`. This effectively produces a `NaN` (Not-a-Number) at the model top when the heights drop from 30 km back down to 20 km. The is later used to index a look-up table. Since no index is initialized for the model top due to NaN value, it may either crash the model or produce unpredictable result depending on what the pre-existing value in the corresponding memory location was. Older runs may see missing photolysis rates at their model tops as a result.

D.1.2 Changes made

The model top input for `photo_inti` has now been changed to 30 km, the mean cloud top for the model set-up used in this study. The ozone column scaling has also been changed to 349 DU. Due to an overall low bias in stratospheric ozone in WRF-Chem, the ozone profile between 20–30 km (model levels) internal of FTUV has also been replaced by that from `o3ref`. With these changes, the FTUV-TUV comparison[2] is shown in Table D.1 for

Table D.1: Compaison of photolysis rates from FTUV and TUV.

z (km)	(FTUV-TUV)/TUV	
	$J(O_3)$	$J(NO_2)$
0	+2.74%	-11.8%
2	+4.51%	-9.88%
5	+10.5%	-9.63%
7	+13.7%	-5.47%
10	+14.9%	-3.00%
20	-8.64%	-1.39%
29	-7.68%	-1.90%

[1] The expected low bias caused by the 265 DU is largely offset by the larger distribution of ozone above the model top due to the extra 20–30 km layer.

[2] The TUV code used here is an independent utility developed and implemented by Dr. Sasha Madronich at NCAR-ACD.

clear-sky condition with a solar zenith angle of 8.428° with a surface albedo of 10%. The remaining biases may be attributed to differences in actual ozone profiles used between WRF-Chem FTUV and the TUV code. It should also be noted that $J(\mathsf{NO_2})$ has slightly different cross-section in the two implementations, so differences are expected.

D.1.3 Other problems

(1) Diagnostic outputs recently added (v3.4.0+) for photolysis spectral and rate information (`radfld`, `adjcoe`, `prate`) are copied through `nz`, which is the number of FTUV model levels including exocolden levels (59 in this study). However, these variables were only defined for `nref`(:= 51) levels. Thus for simulations where `nz`> 51, this statement is a guaranteed crash or out-of-bound access. This problem is patched for this study by removing the respective copy statements since the diagnostics are not used.

(2) The surface albedo over sea water uses different data sets for MOZART and non-MOZART options. The concerning factor here is that the prescribed albedos is about an order of magnitude apart (e.g. 0.0747 for MOZART and 0.8228 for non-MOZART for the first spectral bin). Moreover, all grids are identified as land (`lu`=1) when non-MOZART options are used. No fix has been performed for this particular inconsistency due to lack of knowledge for the intention of the original programmer.

(3) Photolysis cross sections and top-of-atmosphere solar flux have not been updated to more recent recommendations since FTUV's initial implementation in 2003. No direct changes have been made to these values, but constant scaling factors (α) have been applied to several photolysis reactions that have been shown to have significant biases during CALNEX 2010 flight measurements (*C. Knote*, personal communication, 2013). These reactions include $J(\mathsf{HNO_4})$ and $J(\mathsf{MGLY}$[3]$)$ with $\alpha = 0.35$ and 0.20 respectively.

[3] Methylglyoxal, $\mathsf{C_3H_4O_2}$

D.2 Passive tracer-convective transport

Passive tracer diagnostics have been added to WRF-Chem to facilitate air sourcing analyses from predefined sources. These tracers are held constant at 1.0 at their respective sourcing regions (e.g. stratosphere) or emitted by replicating a specified source (e.g. biomass burning, lightning). They are then allowed to be transported through advection and convection. However, because the original implementation of convective transport, performed by the subroutine `grelldrvct`, is designed to operate on the `chem` array, some changes have to be made.

D.2.1 Bug description

The subroutine handling downdraft (`cup_dd_tracer`) in version 3.4.1 iterates over the tracer array, but it uses the global value of `num_chem`, which is the number of chemical species. It works as designed for the `chem` array but since the `tracer` array is typically smaller, out-of-bound memory access occurs. This becomes problematic when the array `tr_pwd(:,:,:,num_chem)` is initialized at the beginning of `cup_dd_tracer`, which overwrites neighboring memory addresses with zeroes, including `ierr`, which identifies if convection has the necessary conditions to happen.

D.2.2 Changes made

An extra parameter is added to the definition of the subroutine `cup_dd_tracer` so that the proper array dimension is used for allocating the "`tracer`" array instead of the global value of `num_chem`, which is always associated with the `chem` array. Alternative naming convention has been suggested, but it will not be implemented until the next WRF-Chem update.

D.2.3 Other problems

(1) The array `tr_dd` in the subroutine `CUP_ct`, which is accumulated in `cup_dd_tracer` through the column top-down, is not initialized properly. This bug is introduced in 3.4 when wet scavenging is added. Older runs may see tracers disappearing when convective transport

is used. It is now properly initialized to 0.0 in `CUP_ct`. For consistency, the same is done for `tr_up`.

(2) Wet deposition for NO_3 and SO_4 are accumulated at the end of the main subroutine `grelldrvct`. However, since the same subroutine is used for convective transport for both `chem` and `tracer` arrays, wet deposition is effectively performed twice. Older runs may see higher ($2\times$) than expected wet deposition. This is fixed by testing for `chemopt` ($== 0$ if transporting tracer), this is not to be confused with `chem_opt`, which is the global chemistry option. Alternative naming convention has been suggested.